

NON-DESTRUCTIVE IMAGING AND FEEDBACK
WITH ULTRACOLD GASES

Department of Physics and Astronomy
Aarhus University
Denmark
2015

PhD thesis by

Miroslav Gajdacz

This thesis is submitted to the Faculty of Science and Technology at the University of Aarhus, Denmark, in order to fulfil the requirements for obtaining the PhD degree in Physics.

The work have been carried out at the Department of Physics and Astronomy with main supervisor prof. Jan Arlt, and co-supervisor prof. Jacob Sherson from August 2011 to July 2015.

Abstract

The field of ultracold atomic gases provides a new opportunity for the investigation of the quantum properties of matter. The rapid progress of both experimental and theoretical research in the past three decades has facilitated an astonishing insight at the level of few atoms as well as large ensembles.

This thesis examines the usage of dispersive, magnetically sensitive, optical probing for high resolution detection of the cold atomic clouds. This minimally destructive online measurement technique is utilized in a feedback scheme, which can actively stabilize the sample production to the level of atom shot noise. In addition, experiments with spinor condensates in a one dimensional vertical optical lattice are presented, where spin changing collisions generating wave packet like excitations with anti-correlated momenta are observed.

The theoretical part of the thesis considers a proposal for a two-qubit quantum gate (controlled-NOT) operating on motional degrees of freedom of atoms trapped in a super-lattice potential. In analogy to the transistor, the gate controls the flux of one atomic species through interaction with a second species of atoms that intermediately occupies the same region in space. Applying the gate principle to a pair of atomic condensates can yield an atomtronic device.

Finally, the limits of time evolution of quantum systems are studied in the theoretical framework of Hilbert space geometry. It is shown that in order to reach a given target state in the fastest way, the direct Hilbert velocity has to be optimized, which can be effectively achieved with common Optimal Control algorithms. Notably, a necessary criterion for convergence of these algorithms is derived from the time dependence of the direct Hilbert velocity.

Resumé

Forskning i ultrakolde kvantegasser har åbnet for nye muligheder for at undersøge kvanteegenskaberne af stof. De hurtige fremskridt indenfor både eksperimentel såvel som teoretisk forskning i de sidste tre årtier har medført en fantastisk indsigt i både systemer med få atomer og såvel som store samlinger af atomer.

Denne afhandling behandler anvendelsen af dispersiv, magnetisk følsom, optisk probing til højt-opløst detektion af kolde atomare skyer. Denne minimalt destruktive målingsteknik bliver udnyttet til løbende målinger i en feedback-protokol, der aktivt kan stabilisere produktionen af atomare skyer til niveauet for den atomare shot støj. I tillæg til dette præsenteres eksperimenter med spinor-kondensater i en-dimensionelle optiske gitre, hvor spin-ændrende kollisioner, der skaber bølgepakker i form af excitationer med antikorreleret impuls, observeres.

I den teoretiske del af afhandlingen præsenteres et forslag til en 2-qubit kvantegate (kontrolleret inverter, CNOT), der opererer på bevægelses-frihedsgraderne af atomer fanget i et supergitter-potentiale. I analogi med transistoren kontrollerer gaten gennemstrømningen af en type atomer ved hjælp af vekselvirkninger med en anden type af atomer, der intermediært optager det samme område i rummet. Anvendelse af gaten på et par af atomare kondensater kan give et atomtronisk apparat.

Endeligt undersøges grænserne for tidsudviklingen af et kvantesystem indenfor de teoretiske rammer af Hilbertrum-geometri. Det bliver vist, at for at opnå en ønsket sluttetilstand hurtigst muligt er det nødvendigt at optimere den direkte Hilbert-hastighed, hvilket kan opnås med almindelige optimal styrings algoritmer. Værd at bemærke er, at et nødvendigt kriterium for konvergens af disse algoritmer bliver udledt ud fra tidsafhængigheden af den direkte Hilbert-hastighed.

Preface

The work presented in this thesis was carried out during my PhD studies at the Institute for Physics and Astronomy at Aarhus University. I have been enrolled in an experimental project aimed at non-destructive Faraday imaging [1,2] and spinor dynamics in optical lattices [3]. My focus was on the Faraday project, whereas my fellow PhD student Poul Lindholm Pedersen focused on the spinor project. Nevertheless we were working together on both, sometimes in parallel, sometimes focusing on a single project for a period of time to complete the data acquisition, evaluation and publications. First part of my thesis presents our most important experimental results from these two fields.

During my studies I was also involved in theoretical projects which originated from an extended collaboration with my bachelor thesis supervisor Prof. Tomáš Opatrný from Palacký University Olomouc in the Czech Republic and Prof. Kunal K. Das from Kutztown University of Pennsylvania in United States of America. This work first examined the possibility of utilizing motional eigenstates of trapped cold atoms as a resource for quantum computation [4], and later analysed the problem of the quantum speed limit in the framework of Hilbert space geometry [5]. The latter was carried out in collaboration with my supervisors at Aarhus University Prof. Jan Arlt and Prof. Jacob Sherson. These results are presented in the second part of my thesis.

My work in the Ultracold Quantum Gases Group at Aarhus University started in January 2011, when I was enrolled as a masters student on a Lindhard Scholarship. At that point the experiment had recently been moved to its present location, so we had to rebuild it in the new facilities. The first experiments were devoted to the study of wave packet dynamics in optical lattices, work initiated by Sung Jong Park and Sune Mai. Together with Poul and another PhD student, Nils Winter, we extended this work, which led to two publications [6,7]. Since Poul and Nils described these experiments extensively in their PhD theses, I have not included them here.

During the time of my scholarship, I had a few months of overlap with Nityanand Sharma, an Indian masters student, who built a Faraday laser system for measurements on a room temperature rubidium gas cell. I helped with the measurements and analysis of the Faraday effect and when Nitya left, I took over the Faraday project. Since the laser system was built on a ‘bread board’, it was possible to place

it on our laser table and quickly integrate it into the existing apparatus. From that point, the Faraday project started to run in parallel with the wave packet investigations, sharing the same experimental system. The wave packet project was later replaced by an investigation of spin changing collisions in optical lattices, which has thus far yielded one publication [3].

The Faraday experiments were also very fruitful. We have published an introductory paper on the dark field Faraday imaging applied to the ultracold atomic clouds [1], where we also present practical applications of the non-destructive measurements. Since then, we have made a considerable progress on the high precision non-destructive atom number measurement and stabilisation with feedback, which will soon be submitted for publication [2].

Acknowledgements

The results presented in this thesis were not obtained by a solitary effort. Indeed, constructing and operating an elaborate experiment is not feasible without the support of mechanical workshop, custom build electronics and neighborly administrative staff. Most importantly, however, the work load has to be shared between all group members and the intermediate results have to be put into perspective based on collective knowledge and experience, in order to target true physical challenges.

These criteria were met especially thanks to engaged supervision of Jan Arlt and Jacob Sherson, who could always turn over the fortune with insightful suggestions, when the progress was not meeting our expectations. My gratitude to Tomas Opatrný can hardly be expressed with words, since he introduced to me the world of research and set me up on a ‘scientific career’. To Kunal Das, I am dearly thankful for our never ending discussions about the ‘ultimate truth’.

My thanks go to Andrew Hilliard, for not hesitating to raise an objection, when my contributions to a discussion are grounded on elusive arguments, and for mending the abundant pitfalls of my english not only in this thesis. A good time in the lab was certainly facilitated by my fellow PhD students: Nils Winter, who had milden my shock of experimental physics when I fist came to Aarhus, Poul Lindholm Peredsen, who was my ‘field mate’ in an uncountable number of cheerful and challenging days and Mick Kristensen, who continues to fill the numerous cavities in my knowledge, sane judgement and sense of humour.

Special thanks go to Lars Wacker, for keeping up the spirit in our synchronous struggle for a perfect PhD thesis, in which he surely succeeded, while helping me out with countless practical issues. Certainly, the time in the office flew faster also thanks to the friendly company of Romain Müller and Nils Byg Jørgensen. The list of people with whom I had the pleasure to collaborate does not end here, however, I have to cut it short, since surpassing the 200 page limit is a sign of bad quality in a PhD thesis.

Not least, I am permanently grateful to my family, for supporting my ambitions since the earliest childhood, and especially to my parents, for seeing a purpose in the plentiful material damage induced by the not quite scientific experiments accompanying my grow up.

List of publications

1. M. Gajdacz, P. L. Pedersen, T. Mørch, A. Hilliard, J. Sherson and J. Arlt, *Non-destructive Faraday imaging of dynamically controlled ultracold atoms*, Rev. Sci. Instr. **84** (2013), 8, p. 083105.
doi:1.1063/1.4818913
2. M. Gajdacz, M. Kristensen, P. L. Pedersen, J. Arlt, A. Hilliard and J. Sherson, *Active stabilization of ultracold atomic clouds*, draft
3. P. L. Pedersen, M. Gajdacz, F. Deuretzbacher, L. Santos, C. Klempt, J. F. Sherson, A. J. Hilliard and J. J. Arlt, *Spin dynamics in a two-dimensional quantum gas*, Phys. Rev. A **89** (2014), p. 051603.
doi:10.1103/PhysRevA.89.051603
4. M. Gajdacz, T. Opatrny and K. K. Das, *An atomtronics transistor for quantum gates*, Physics Letters A **378**, 1919-1924 (2014).
doi:10.1016/j.physleta.2014.04.043
5. M. Gajdacz, K. K. Das, J. Arlt, J. Sherson and T. Opatrny, *Time limited optimal dynamics beyond the Quantum Speed Limit*, arXiv:1405.6079, considered for publication in Physics Review A
6. J. F. Sherson, S. J. Park, P. L. Pedersen, N. Winter, M. Gajdacz, S. Mai and J. Arlt, *The pump-probe coupling of matter wave packets to remote lattice states*, New Journal of Physics **14** (2012), 8, p. 083013.
doi:10.1088/1367-2630/14/8/083013
7. P. L. Pedersen, M. Gajdacz, N. Winter, A. J. Hilliard, J. F. Sherson and J. Arlt, *Production and manipulation of wave packets from ultracold atoms in an optical lattice*, Phys. Rev. A **88** (2013), p. 023620.
doi:10.1103/PhysRevA.88.023620

CONTENTS

Abstract	i
Resumé	ii
Preface	iii
List of publications	vi
I Cold atom experiments	1
1 Introduction	3
2 Trapping and cooling neutral atoms	9
2.1 Cooling and trapping by laser light	9
2.2 Conservative traps for atoms	11
2.3 Evaporative cooling and Bose-Einstein condensation	15
2.4 Experiment overview	17
3 Correlated wave packet generation by spin changing collisions	19
3.1 Experimental system	19
3.2 Theory of 2D wave packet excitations	22
3.3 Observation of spinor wave packets	29
4 Non-destructive Faraday imaging	37
4.1 Faraday rotation	37
4.2 Dark field Faraday imaging	39
4.3 Signal-to-noise analysis of dispersive imaging techniques	40
4.4 Faraday laser system	45
4.5 Atom number and temperature calibration	46
4.6 Monitoring system dynamics	48

5	Actively stabilized preparation of atomic clouds	53
5.1	Online image analysis	54
5.2	Active experiment control	59
5.3	Measurement precision and destructivity	62
5.4	Shot noise limited sample preparation	70
5.5	Stable sample production	78
6	Conclusion and Outlook	85
II	Quantum gates and Optimal Control	87
7	Introduction	89
8	An atomtronics transistor for quantum gates	95
8.1	Static operation scheme	95
8.2	Physical models: Single atoms and Dual species condensates	98
8.3	Dynamic gate and Transistor	99
8.4	Feasibility analysis	102
8.5	Fidelity and noise	105
9	Hilbert space geometry and the quantum speed limit	107
9.1	Hilbert space geometry	107
9.2	Relative motion	109
9.3	Optimal navigation	111
9.4	Time fidelity trade-off	113
9.5	Entanglement generation in a multilevel system	115
10	Conclusion and Outlook	119
A	^{87}Rb D2 line and the Faraday laser	121
	Bibliography	134

Part I

Cold atom experiments

Introduction

The atom, an indivisible building block of matter postulated by the ancient Greeks, turned out to be consisting of yet smaller parts. In 1897, the electron was discovered by John. J. Thomson [1], and a decade later, Ernst Rutherford concluded from his scattering experiments, that most of the atomic volume is actually empty and all the remaining matter is concentrated in a nucleus [2]. For most practical purposes, however, atoms are indeed indivisible, since the electrons are bound to the core with a strong electric attraction. Still, the electrons can occupy different motional states, which gives a rise to a rich structure inside the atom, and effectively determines properties of all common matter, including that of our living bodies. Surprisingly though, all the atomic interactions are mediated by a single force: electro-magnetism.

Naturally, as all matter is made of atoms, many different aspects of their behaviour have been studied in great detail. The field of ultracold atoms is focusing on the investigation of atomic properties in the gas phase, the most dilute form of matter, where atoms ‘fly’ freely in space undisturbed by each other’s fields, interacting only briefly during collisions. In the past three decades, research in this field has provided insight into many fundamental properties of matter. Phenomena such as quantum indistinguishability and the interference of particles have been demonstrated experimentally with both bosonic [3] and fermionic atoms [4]. Great control over all atomic degrees of freedom has facilitated astonishing precision in the measurements of external fields [5], as well as time and space [6]. However, our knowledge of the quantum mechanical properties of the atoms and the techniques for handling and utilizing them still have a large potential for improvement.

A gas in a container evolves through inter-atomic collisions into a state with maximal entropy, called thermal equilibrium. When cooling a gas of bosonic particles¹ below a certain critical temperature (typically $< 1 \mu\text{K}$), it is favourable to

¹Bosons are particles with integer angular momentum.

distribute the thermal energy of the system among a finite fraction of the particles, while placing the rest in a zero entropy state: the ground state of the confining potential. Quite counterintuitively, such a configuration can carry more entropy. The macroscopic ensemble of indistinguishable particles ($\approx 10^4 - 10^7$ atoms), all in the same quantum state, is called a Bose-Einstein condensate (BEC) [7]. At absolute zero temperature, the entire cloud forms a pure condensate, described by a single wavefunction, which can be viewed as a single macro-particle.

As outlined above, atomic clouds can only be manipulated via electromagnetic fields. The palette of the available techniques is, however, very rich. Most atoms respond both to static magnetic fields and to radio frequency radiation, which couple to their internal degrees of freedom of the atom. Also, scattering of light at frequencies close to the internal atomic transitions can act on the atoms with a strong force, and is utilized in the laser cooling and trapping techniques. An intense off-resonant light can, in turn, develop a strong conservative force through the so called dipole interaction, with only a small amount of spontaneously scattered photons.

The spatial density distribution of the cloud is the main source of information about the cloud dynamics, e.g., a colder cloud occupies a smaller volume in the confining potential. The density distribution can be extracted most conveniently by optical imaging techniques. A commonly used technique for precise ultracold cloud imaging, so-called absorption imaging, is based on incoherent light scattering and obtains the cloud shape from a shadow cast by the atoms on a resonant imaging beam. However, the method can only reliably resolve optical densities of the order of one. Since the typical in-trap density of an ultracold cloud is two orders of magnitude larger, the cloud has to be released from the trap, whereupon it expands in free fall. The in-trap distribution can be reconstructed from the time-of-flight image, provided the expansion mechanism is known. The large number of spontaneously scattered photons required for high sensitivity imaging immediately destroys the cloud, allowing only for a single image of a given sample.

Non-destructive imaging and feedback

Many experiments involve monitoring some dynamical process. In this case, the sequence has to be repeated many times, where a destructive image is acquired at different points in time. Such a measurement is not only time consuming, but also susceptible to run-to-run fluctuations and drifts in the experimental apparatus, which cause scatter in the data. Being able to measure the atomic distribution repeatedly in a single run virtually eliminates these problems. In addition, feedback to the experimental apparatus can be applied, since the state of the atomic system can be monitored in real-time, and the evolution of the cloud can be driven towards a desired state.

Non-destructive measurements of atomic ensembles have been realized using

several dispersive techniques, such as phase contrast imaging (PCI) and dark fields scalar imaging (DFSI) [7] utilizing the polarization independent phase shift, as well as polarization resolved techniques based on Faraday rotation (FR) [8, 9]. Further, the non-destructive detection was facilitated by diffractive techniques [10], and most recently, partial-transfer absorption imaging [11]. The achievable signal-to-noise ratio in all of these approaches is similar [12], hence the experimental requirements typically prescribe the method of choice.

The quantum non-demolition (QND) measurements based on FR in room temperature atomic ensembles have been used to demonstrate entanglement [13], quantum memory [14], and quantum teleportation [15]. In the regime of ultracold atoms [16, 17], this approach has yielded spectacular results including spin squeezing [18], magnetometry [5], and the observation of many-body dynamics [19].

In this work, we have adapted the Faraday imaging method for fast and reliable measurement of ultracold atomic clouds. Faraday imaging is based on the polarization rotation that occurs when light passes through a spin-polarized atomic sample. In our approach, the spatially dependent angle of rotation is detected by measuring the intensity of rotated light transmitted through a polariser onto a camera. The method can thus be regarded as a form of dark field imaging [7] and we refer to it as dark field Faraday imaging (DFFI). Provided one can generate imaging light that is detuned from an atomic resonance by 10 to 100 natural linewidths, the method can be realized by inserting a single polariser in a standard absorption imaging set-up and is thus considerably simpler to implement than PCI or dual-port homodyne detection schemes [17].

We have calibrated the DFFI technique relative to the absorption imaging and brought its precision to the photon shot noise limit. We use the method in several experiments, such as monitoring of in-trap cloud oscillations or magnetic field detection, but most importantly, we have achieved a high precision online atom number stabilization by providing feedback to the experimental sequence.

Correlated wave packet generation

Spinor condensates, large ensembles of coherent particles with a variable spin degree of freedom, were first investigated in early BEC experiments with rubidium [20, 21] and sodium [22]. Since then, this research has brought considerable insight into quantum magnetism and numerous interesting effects, such as spontaneous symmetry breaking [23] or parametric amplification of vacuum fluctuations [24].

A BEC in a trapped dilute gas typically occupies the lowest vibrational state, yielding a high density sample with a small velocity spread. In a collision process, particles can exchange energy and momentum, which can lead to a change of their state, however the total energy and momentum has to be conserved. If two ‘colliding’ particles are initially at rest, they will emerge in anti-correlated

quantum states: one with momentum \mathbf{p} , the other with $-\mathbf{p}$. This is an example of a so called Einstein-Podolsky-Rosen (EPR) pair [25] which exhibits the non-locality of quantum mechanics [26]. The two particles are said to be entangled: a measurement of particle A immediately influences the quantum state of particle B. Although no classical information can travel in this way, the subsequent evolution of the state B will depend on the outcome of measurement A, irrespective of the particles' separation. This 'action at a distance' is one of the most puzzling features of quantum mechanics [27, 28].

Apart from momentum, colliding atoms can also exchange quanta of their internal angular momentum, that is change their spin. Since the total spin must be preserved, equal numbers of particles with increased and decreased spin, N_+ and N_- , are generated. This is analogous to two-mode squeezing in spontaneous parametric down-conversion, where a high energy photon is converted into two lower energy photons in a non-linear optical medium [29]. The squeezing of the number difference $N_+ - N_-$ below the atom shot noise limit $\sqrt{\langle N \rangle}$ in spontaneous spin changing collisions has been observed [30, 31], and can potentially be used to enhance the sensitivity of atom based interferometers.

The energy of the spin components depends on the external magnetic field, and therefore a change of the spin states in a collision can yield an excess energy, which has to be accommodated in the motional degrees of freedom. When the excess energy is small, only the ground motional state is populated, permitting the use of a single-spatial-mode approximation. Coherent oscillations between the spin components has been observed both in bosonic [32, 33] and fermionic [34] systems.

Once the excess energy is high enough to populate excited motional states, the evolution scenario depends on the separation of the eigenenergies, determined by the confinement of the gas. A tight trap with a large energy spacing between the eigenstates allows to populate individual excited modes [35]. The spatial structure of these modes can be imaged using the time-of-flight technique [36]. First experiments employed a rotationally symmetric trap, and the observed Bessel modes demonstrated spontaneous spatial symmetry breaking [37].

In our experiments, we observe spin changing collisions in a one-dimensional vertical optical lattice generated by a retro-reflected red-detuned Gaussian beam. The high lattice depth does not allow for tunnelling between neighbouring lattice sites, and thus each site is populated with an individual BEC in the ground state of that well. The atoms are weakly confined in the radial direction by the cylindrically symmetric potential of the lattice beam, and the transverse modes are excited in the spin changing collisions. The high mode density nearly forms a continuum, thus individual stationary states cannot be addressed.

We observe that the spinor excitations have a wave packet like character. The velocity of these wave packets is set by the bias magnetic field (the excess scattering energy), while the direction of propagation in the 2D plane is chosen randomly—

though in anti-correlated directions—in the two spin components.

Structure of part I

The first part of the thesis is organized as follows:

- Chapter 2 provides an overview of the atom-light interaction and Bose-Einstein condensation. Moreover it outlines essential experimental techniques for cooling and trapping of atomic gases.
- Chapter 3 discusses our results on the spin changing collisions in a 1D optical lattice.
- Chapter 4 characterizes the method of dark field Faraday imaging and presents some of its applications.
- Chapter 5 examines the high precision regime of non-destructive measurements and the application of feedback to the experimental sequence.
- Chapter 6 summarizes the most important results and discusses further experimental perspectives.

Trapping and cooling neutral atoms

Our goal is to investigate properties of cold and dense atomic gas samples. On the way from the room temperature 300 K to the ultracold ~ 100 nK regime a multitude of techniques must be utilized, in order to span such tremendous difference of physical conditions. An ultra high vacuum is a must. Next comes a cooling and confinement by a laser light, followed by a compression and an evaporative cooling in a conservative trap, which finally yields a Bose-Einstein condensate in the ground state of the well. In this chapter we will review the physical principles of the essential experimental techniques required to reach the quantum degeneracy.

2.1 Cooling and trapping by laser light

The 1997 Nobel Prize in Physics was awarded to Steven Chu, Claude Cohen-Tannoudji and William D. Phillips for ‘*development of methods to cool and trap atoms with laser light*’ [38]. These methods were first implemented in 1985, and within a decade, temperatures below $1 \mu\text{K}$ were reached, surpassing both the Doppler limit and the recoil limit [39, 40].

Optical molasses

To cool down a physical system, its entropy has to be transferred to an external reservoir. In the Doppler cooling scheme, the reservoir is a coherent laser light. Photons with a very well defined propagation direction get scattered into random directions, their entropy increases, but the entropy of the atoms can be reduced.

An atom can undergo transition into different electronic state by absorption or emission of photons, provided the photon energy is close to the energy of an atomic transition. Each photon carries energy $E = h\nu$ and momentum $p = E/c$, where ν is frequency of the light¹. The photon momentum is transferred into the translational motion of the atom. The rate of momentum exchange is then the origin of an external force $F = dp/dt$.

When the atoms are illuminated with a red detuned light² in all directions³, the Doppler shift brings the photons propagating *against* the motion of each atom closer on resonance, resulting in a higher absorption rate. Subsequently the photons are emitted in a random direction, hence, in total, this causes a net force against the motion of the atoms, which reduces their kinetic energy.

Weak magnetic field interaction

Since neutral atoms do not possess a net electric charge, they do not interact with weak electrostatic fields⁴, however they do interact with low magnetic fields by means of the magnetic dipole moment.

In analogy with a current loop, the angular motion of the electric charge induces a magnetic dipole moment

$$\hat{\mu} = -\frac{\mu_B}{\hbar} g_F \hat{\mathbf{F}}, \quad (2.1)$$

where μ_B is the Bohr magneton, and g_F is the hyperfine Landé g -factor representing the distribution of the charge [41]. Interaction with the magnetic field $-\hat{\mu} \cdot \mathbf{B}$ removes the energetic degeneracy of the hyperfine states $|F, m_F\rangle$ due to the linear Zeeman effect

$$\Delta E(m_F) = \mu_B g_F m_F B_z, \quad (2.2)$$

where the quantization axis z is aligned with the magnetic field.

Magneto-optical trap

The laser cooling mechanism by itself does not confine the gas, however, a confining effect can arise when the atomic transition energy is spatially dependent. Such shifts of the resonance can be obtained by combining the laser field of an optical molasses with a weak magnetic QP-field (see Eq. (2.4) and Fig. 2.2), which create a so called magneto-optical trap (MOT) [39, 40].

¹ h is the Planck constant and c is the speed of light.

² The light frequency is lower than the atomic transition.

³ Two counter-propagating beams per each axis.

⁴ Strong electrostatic field can induce an electric dipole moment: the *dc Stark effect*.

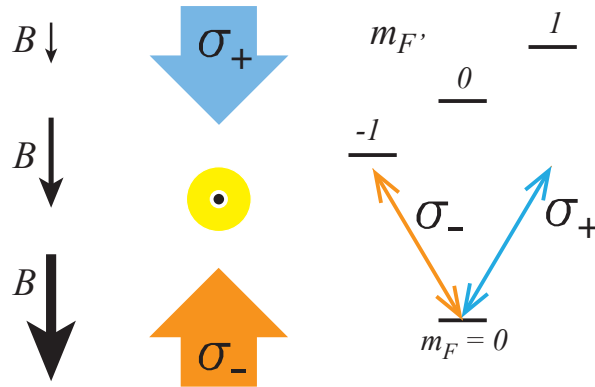


Figure 2.1: Schematics of the confining action of the MOT.

Figure 2.1 shows schematically an action of a restoring force for an atom that has been displaced downwards from the centre of the trap. The black arrows on the left represent the growth of the magnetic field with the displacement, which brings the atom (yellow particle) closer on resonance with the σ_- polarized beam (orange) propagating upwards. This increases the scattering rate on the σ_- transition, which pushes the atom back into the centre. For an upward displacement, the orientation of the local magnetic field would be opposite, bringing on resonance the downwards propagating beam (blue), and restoring the position again. Interestingly, it is always the σ_- transition that scatters the most photons. Similar restoring effects can occur in the two horizontal directions, provided the polarisation of the laser beams is chosen appropriately.

Often the ground state manifold of the atom has more than one state, which causes scattering on multiple distinct transitions, however, the operating principle of the MOT remains the same. The first MOT was constructed by Steven Chu and co-workers in 1987, and was operating with sodium atoms [42].

2.2 Conservative traps for atoms

To study atoms without the presence of spontaneous photon scattering, the cloud can be trapped in a conservative potential. The potential can be engineered either by a static magnetic fields or ‘dressing’ of an electronic transition with far a detuned time varying field. The later can be achieved by using micro-wave (MW) [43, 44] or optical transitions. In the following we will discuss the magnetic and optical trapping techniques.

Magnetic field trapping

In an inhomogeneous field, the magnitude and orientation of the magnetic field vector \mathbf{B} is spatially varying. An atom in motion experiences a time varying field, however, it remains in an immediate eigenstate $|F, m_F\rangle$ with respect to the local field, provided the change in the field is adiabatic, that is slow compared to the Zeeman level separation. The spatially varying energy is in fact a potential energy

$$U(\mathbf{r}) = \mu_B g_F m_F |\mathbf{B}(\mathbf{r})|, \quad (2.3)$$

which can generate a confinement for selected $|F, m_F\rangle$ states in certain magnetic field configurations.

The simplest implementation of a magnetic trap is a quadrupole (QP) field

$$\mathbf{B}_{\text{QP}}(x, y, z) = B'_{\text{QP}} \begin{pmatrix} x \\ -2y \\ z \end{pmatrix} \quad (2.4)$$

generated by pair of parallel coils with electric currents flowing in opposite directions, the so called anti-Helmholtz configuration. The gradient B'_{QP} is proportional to the current and determines magnitude of the restoring force. The trapping occurs for states with $g_F m_F > 0$. The corresponding potential is cone like, rotationally symmetric in the xz -plane with a twice as strong gradient along the symmetry axis y , see Fig. 2.2.

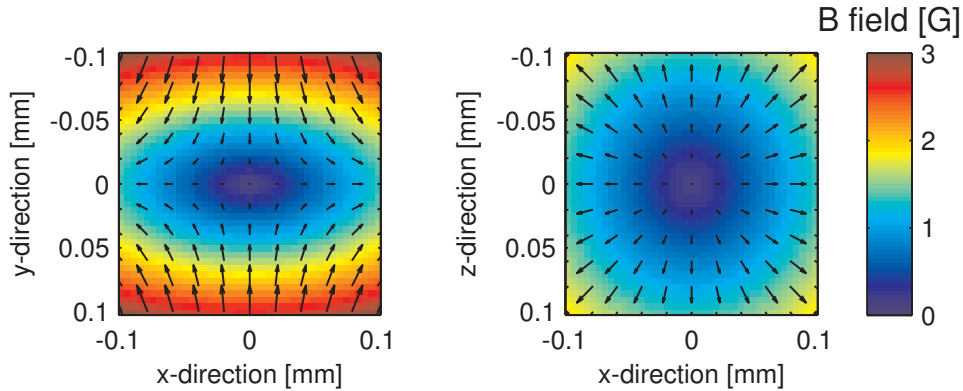


Figure 2.2: Illustration of a quadrupole magnetic field. The arrows show direction of the field, the colour encodes the field magnitude. The gradient constant was chosen $B'_{\text{QP}} = 133 \text{ G/cm}$, to represent a typical QP-trap.

For a typical gradient $B'_{\text{QP}} \sim 150 \text{ G/cm}$, the QP-field can be used for trapping thermal clouds with temperatures above $\sim 10 \mu\text{K}$. As the cloud gets colder, atomic density in the region with zero magnetic field increases, and the atoms are more likely to undergo transition into un-trapped magnetic states, an effect known as

Majorana losses. Therefore, to hold a Bose-Einstein condensate in a magnetic trap, a different field configuration is required.

The so called Ioffe-Pritchard trap provides a non-zero bias field in the trap centre preventing the Majorana spin flips. In our experiment this is achieved by placing an additional coil (Ioffe coil) at $z = -d$ (oriented along the z -axis), which creates a field

$$\mathbf{B}_I(x, y, z) \approx B_I(z) \begin{pmatrix} x \\ y \\ -2z \end{pmatrix} \quad (2.5)$$

with a decaying magnitude $B_I(z) \propto 1/(z^2 + d^2)$. The minimum of the combined potential occurs at a position where the field gradient from the Ioffe coil cancels the gradient of the QP-field in the z -direction. Consequently the gradient in the y -direction is now reduced to 75%, while the gradient along the x -direction is increased by 50%, making the two directions equally strong. The combined field can be expressed as

$$\mathbf{B}_{IP}(x, y, z) = \begin{pmatrix} 0 \\ 0 \\ B_0 \end{pmatrix} + B' \begin{pmatrix} x \\ -y \\ 0 \end{pmatrix} + \frac{B''}{2} \begin{pmatrix} -xz \\ -yz \\ z^2 - (x^2 + y^2)/2 \end{pmatrix}, \quad (2.6)$$

which gives rise to a harmonic trapping in all three directions. The trap is cylindrically symmetric and elongated in the z -direction, see Fig. 2.3.

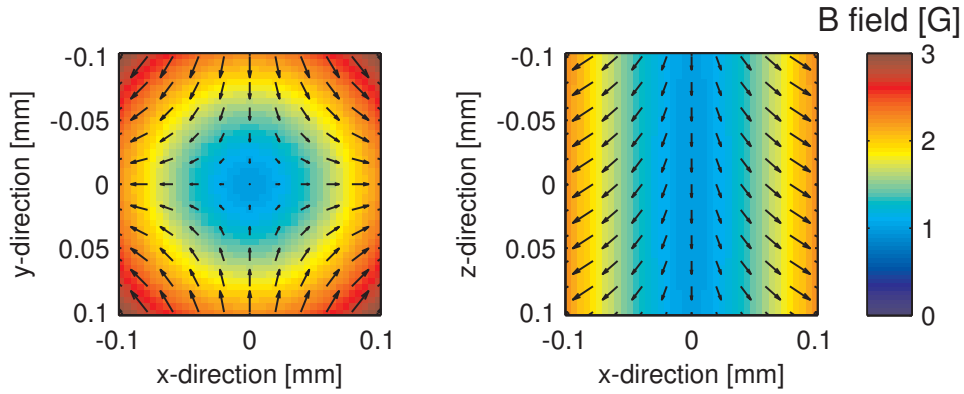


Figure 2.3: Illustration of the Ioffe-Pritchard trap. The arrows show direction of the field, the colour encodes the field magnitude. The parameters are $B_0 = 1\text{G}$, $B' = 200\text{G/cm}$ and $B'' = 200\text{G/cm}^2$. The trapping along the z -axis is a factor of 10 weaker than in the x and y directions.

Optical dipole trap

Magnetic traps allow to trap only certain magnetic sub-states, and the potential strength depends on the magnetic number m_F . An equally strong confinement of all the m_F components can be accomplished by a purely optical trap using off-resonant forward scattering. This regime requires a light with large detuning and consequently high power. Due to presence of the electric field interaction $-e\mathbf{E}(t)\hat{\mathbf{r}}$, the stationary states of the atom are modified, now being a superposition of the bare ground $|g\rangle$ and excited $|e\rangle$ state. The energy of the new ground state is shifted by

$$\Delta E_g = \frac{I}{(\nu - \nu_0)} \frac{e^2}{2\hbar c \epsilon_0} |\langle g|\hat{x}|e\rangle|^2, \quad (2.7)$$

where ν and ν_0 are the laser and atomic transition frequencies, I is the light intensity and $\langle g|\hat{x}|e\rangle$ is the dipole matrix element⁵ [39].

As the atoms move across regions of spatially varying light intensity, they remain adiabatically in the immediate ground state and thus experience a potential energy $U(\mathbf{r}) \propto I(\mathbf{r})$. In general, red detuned light ($\nu < \nu_0$) produces an attractive potential, while blue detuned light ($\nu > \nu_0$) is repulsive.

Optical lattice

Overlapped coherent laser beams can create standing wave patterns, which form a periodic potential for the atoms. This is similar to the crystal lattice potential experienced by electrons in a solid state of matter, hence the term optical lattice [45]. Similarly to the solid state, motional eigenstates of the trapped atoms organize into a band structure.

The potential in the lattice direction (denoted by y for later convenience) can be written as

$$V(y) = sE_R \sin^2(ky), \quad (2.8)$$

where s is the dimensionless lattice depth in units of photon recoil energy $E_R = \hbar^2 k^2 / (2m)$, $k = 2\pi/\lambda$ is the wave-number and m is the atomic mass. Around the minimum of an individual well, the potential can be expressed as

$$V(y) \approx sE_R k^2 y^2 = \frac{s\hbar^2 k^4}{2m} y^2, \quad (2.9)$$

which after comparison with a harmonic potential $\frac{1}{2}m\omega_y^2 y^2$ yields the trapping frequency of the well as

$$\omega_y = \frac{\hbar k^2}{m} \sqrt{s}. \quad (2.10)$$

⁵The polarization of the light was assumed to be linear: along the x -axis. The constants e and ϵ_0 are the elementary charge and the vacuum permittivity.

Typically, the trapping frequency is of the order of ~ 10 kHz.

2.3 Evaporative cooling and Bose-Einstein condensation

The laser cooling techniques alone can not produce a BEC [40]. In rough terms, this is caused by the discreteness of the spontaneous photon scattering. Since every absorbed photon has to be emitted, the associated recoil is unlikely to leave the atom completely at rest. To reach the motional degeneracy, evaporative cooling has to be employed.

Atoms in a gas phase exchange momentum and kinetic energy by collisions. Since this process is stochastic, the particles do not emerge from the collision with an equal share of energy. Some collisions can generate atoms with kinetic energy high above the average. If those are eliminated from the cloud, the remaining particles will be colder.

A direct way to remove the hot atoms is to engineer a finite trap depth. Only the atoms reaching a certain potential energy can leave the trap. When the trap depth is decreased slowly compared to the rethermalisation rate, a continuous atom loss and cooling occurs. An optical dipole trap has by construction always a finite depth. Evaporation can hence be introduced by ramping down the trapping beam intensity or application of external magnetic field gradient pulling the atoms out of the trap.

A magnetic field can not be shaped so easily, however, the strength and sign of the potential depends on the magnetic sub-state. By applying a radio-frequency (RF) radiation⁶ resonant with the Zeeman level splitting, the atoms can be transferred into untrapped states. This technique is called RF evaporation. Since the Zeeman energy is spatially varying, only a certain spatial shell is addressed with a chosen RF frequency, see Figs. 2.2 and 2.3. A continuous evaporation can be accomplished by a slow sweep down of the RF frequency.

Bose-Einstein condensation

A Bose-Einstein condensate (BEC) is achieved when a single quantum state is populated with a large number of particles. When a cloud of bosonic particles is cooled below a certain critical temperature, Bose statistics implies much higher population probability for the energy ground state than for the remaining states. The reduced effective kinetic energy $E_K = \pi k_B T$ leads to an increase of the de Broglie wavelength $\lambda_{dB} = h/\sqrt{2mE_K}$, which can span the size of the sample. Thus

⁶Evaporation can also be carried out by a transfer to a different hyperfine ground manifold, which might require a micro-wave radiation.

when the number of particles per volume λ_{dB}^3 —the so called phase space density—exceeds one, Bose-Einstein condensation can occur. This process was extensively described in many textbooks [46] and review articles [40].

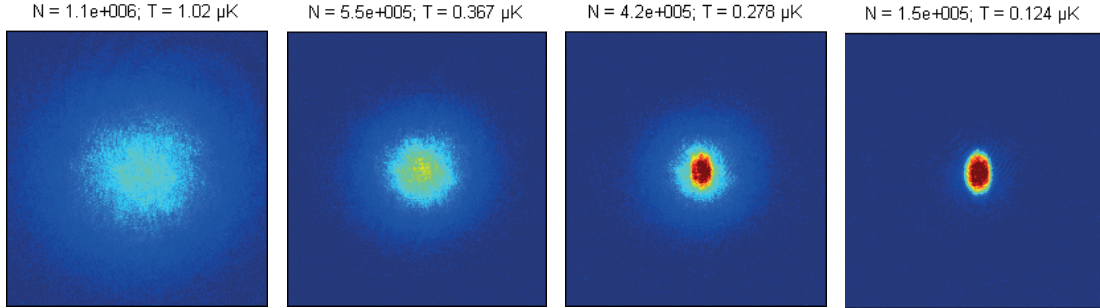


Figure 2.4: Example of ^{87}Rb BEC formation for decreasing end evaporation frequency in a magnetic trap. The absorption imaging pictures were taken in time-of-flight (15 ms). The upper captions show the atom number and temperature of the cloud. The two later pictures show a BEC condensate in the centre.

An important property of a trapped interacting BEC is the vanishing kinetic energy compared to the energy shift due to the density of the gas—the mean field energy. The density distribution of the lowest energy state then acquires the shape of the potential in a fluid like fashion: e.g. a harmonic trap produces a cloud in the shape of an inverted parabola.

When the BEC is abruptly released from the trap, the mean field energy initiates expansion of the cloud. The expansion velocity depends on the gradient of the density, thus a more tightly confined dimensions expand faster. In an asymmetric trap, this leads to the inversion of the aspect ratio in a long time-of-flight.

Unlike a BEC, a thermal cloud always acquires a round shape when expanding freely, since the size of the cloud after expansion is a measure of the in-trap velocity distribution, which is given by the cloud temperature. The spatial distribution is well described by a Gaussian function.

The atomic density distribution can be probed conveniently by absorption imaging. A resonant laser beam is shone through the vacuum chamber and imaged on a CCD camera. The spontaneous photon scattering removes light from the beam proportionally to the local atomic density. The atomic density can thus be reconstructed from the shadow, provided the atomic scattering cross-section is known. Figure 2.4 shows examples of evaluated absorption images. The images are typically taken after 15 ms expansion time to resolve the variations in the atomic density.

2.4 Experiment overview

The first ultracold atom apparatus at Aarhus University produced the first BECs in 2006, and since then has carried out a wide range of experiments involving both magnetic and optical traps. The experiment uses ^{87}Rb atoms, one of the most common species for ultracold gas experiments [47]. The technical implementations were extensively described in the PhD theses of P. Pedersen [48] and H. K. Andersen [49]. Here only an overview of its characteristic features is provided.

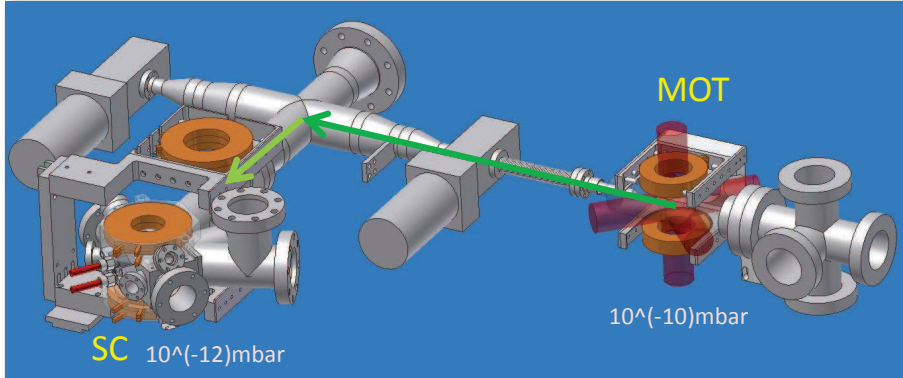


Figure 2.5: 3D model of the vacuum chamber and the transport coil system. The transport consists of two sequential moves (denoted with the green arrows).

The experimental apparatus is divided into two vacuum chambers: the MOT chamber with 10^{-10} mbar pressure and the science chamber (SC) with 10^{-12} mbar pressure, separated by a differential pumping stage. First, the atoms are loaded from the background gas and cooled in a 3D MOT, then the cloud is transferred by a mechanical motion of the trapping coils to the science chamber, where it can be evaporatively cooled until a BEC is formed. The cloud can also be loaded into an optical trap for further experiments.

In our MOT, we obtain a cloud of $\sim 10^9$ atoms at a temperature $\sim 50 \mu\text{K}$. The MOT phase concludes by state preparation via optical pumping, which transfers the atoms into $|F = 2, m_F = 2\rangle$ state (see the level structure in appendix A). This state experiences a positive Zeeman shift and can be trapped by the magnetic potential of the MOT-coils when the current is ramped up. Once the cloud is trapped and compressed, a mechanical motion of the trapping coils translates the atoms over a differential pumping stage into the science chamber (SC). At the end of the transport, the cloud temperature is about $150 \mu\text{K}$.

Due to a very low pressure in SC, the lifetime of the cloud is extended to about 60 s. Here, the atoms can be cooled by forced RF evaporation, first in a QP-field and later in a Ioffe-Pritchard trap. The transverse trapping frequency can be adjusted by the choice of the z -axis bias field in range from 80 Hz to 360 Hz, while

the weak longitudinal trapping frequency remains ~ 17.5 Hz.

The cloud sags slightly in the magnetic trap, such that the vertical field gradient compensates the gravitational force. This gives a rise to a non-zero vertical component of the magnetic field. In our trap, however, the magnetic field tilt due to the sag is less than a percent.

Correlated wave packet generation by spin changing collisions

This chapter presents our results on spin changing collisions in a one-dimensional optical lattice, where we observe wave packet like excitations in the weakly trapping, transverse degrees of freedom. The material was to a large extent presented in our publication [50], where the mechanism of excitations was analysed in the Bessel mode basis—the spectrum of cylindrical box eigenstates. In the paper, we arrived at a conclusion that multiple modes are excited simultaneously due their small energy spacing compared to the magnitude of the instability rate.

Here, we analyse the problem in the position and momentum space, which highlights the wave packet character of these excitations, predicts their spatial width and offers a complementary model for the time-of-flight size of the clouds. In addition, we provide arguments supporting generation of a single anti-correlated wave packet pair per lattice site. Only the essential characteristics of the experimental system are provided. More details about the technical implementation and magnetic field calibration can be found in the PhD thesis of Poul L. Pedersen [48].

3.1 Experimental system

Single site atomic density

The BEC is trapped in a red-detuned vertical optical lattice along the y -axis with wavelength $\lambda = 914\text{nm}$, created by a retro-reflected beam. For our default lattice depth, $s = 18$, Eq. (2.10) yields a trapping frequency $\omega_y \approx 2\pi \times 23.4\text{kHz}$ in the lattice direction. The transverse trapping frequency was measured to be

$\omega_\rho \approx 2\pi \times 50\text{Hz}$, which justifies the assumption that the longitudinal degrees of freedom (along the lattice) are ‘frozen’ and the system is effectively two dimensional.

Each lattice site contains an individual BEC. For a large number of particles, the condensate can be described by a single wavefunction governed by the Gross-Pitaevskii equation [46]

$$\left[-\frac{\hbar^2}{2m} \nabla^2 + V(\mathbf{r}) + U_0 |\psi(\mathbf{r})|^2 \right] \psi(\mathbf{r}) = \mu \psi(\mathbf{r}), \quad (3.1)$$

where μ is the chemical potential and $U_0 = 4\pi\hbar^2 a/m$ is the strength of the interaction given by the s -wave scattering length a . The chemical potential is chosen such that the wavefunction is normalized to the particle number $N = \int d\mathbf{r} |\psi(\mathbf{r})|^2$. The energy associated with the lattice trapping frequency is much higher than the interaction energy $\sim h \times 1\text{kHz}$, thus the y -dimension can be described by the ground state of a harmonic potential

$$\phi(y) = \frac{1}{\sqrt{l_y} \sqrt{\pi}} \exp\left(-\frac{y^2}{2l_y^2}\right), \quad (3.2)$$

with a harmonic oscillator length $l_y = \sqrt{\hbar/m\omega_y}$. Substituting the factorized wavefunction $\psi(\mathbf{r}) = \phi(y)\psi(\boldsymbol{\rho})$ into Eq. (3.1), multiplying from the left by $\phi^*(y)$ and integrating over y yields a two dimensional Gross-Pitaevskii equation

$$\left[-\frac{\hbar^2}{2m} \nabla^2 + V(\boldsymbol{\rho}) + \tilde{U}_0 |\psi(\boldsymbol{\rho})|^2 \right] \psi(\boldsymbol{\rho}) = \tilde{\mu} \psi(\boldsymbol{\rho}), \quad (3.3)$$

where the 2D interaction strength is

$$\tilde{U}_0 = U_0 \int dy |\phi(y)|^4 = \frac{U_0}{l_y \sqrt{2\pi}}, \quad (3.4)$$

and the effective chemical potential is $\tilde{\mu} = \mu - \hbar\omega_y/2$.

To obtain the transverse distribution, we can apply the Thomas-Fermi approximation and neglect the kinetic energy term in Eq. (3.3). The resulting 2D density is

$$|\psi(\boldsymbol{\rho})|^2 = \max\left(0, \frac{\tilde{\mu} - V(\boldsymbol{\rho})}{\tilde{U}_0}\right). \quad (3.5)$$

The density goes to zero at the Thomas-Fermi radius ρ_0 , when $\tilde{\mu} = V(\boldsymbol{\rho})$, which for a harmonic potential implies $\tilde{\mu} = \frac{1}{2}m\omega_\rho^2 \rho_0^2$. For $|\boldsymbol{\rho}| = \rho < \rho_0$ we can thus write $V(\boldsymbol{\rho}) = \tilde{\mu} \left(\frac{\rho}{\rho_0}\right)^2$ and

$$|\psi(\boldsymbol{\rho})|^2 = \frac{\tilde{\mu}}{\tilde{U}_0} \left[1 - \left(\frac{\rho}{\rho_0}\right)^2 \right]. \quad (3.6)$$

To obtain the 2D chemical potential, we can verify the normalization

$$N = \int_0^{2\pi} \int_0^{\rho_0} \rho d\rho |\psi(\boldsymbol{\rho})|^2 = \frac{2\pi\tilde{\mu}\rho_0^2}{\tilde{U}_0} \int_0^1 dw w(1-w^2) = \frac{\pi\tilde{\mu}^2}{\tilde{U}_0 m \omega_\rho^2}, \quad (3.7)$$

which gives

$$\tilde{\mu} = \omega_\rho \sqrt{\frac{N\tilde{U}_0 m}{\pi}}. \quad (3.8)$$

Lattice loading

To find the number of particles in each lattice site, we need to know the atomic density at the moment of loading into the lattice. The loading procedure involves decompressing the magnetic trap while the lattice is being ramped up. We estimate that the density along the lattice dimension becomes fixed at a lattice depth $s = 10$, at which point the magnetic trapping frequencies are $\bar{\omega}_x = \bar{\omega}_y \approx 2\pi \times 200\text{Hz}$ and $\bar{\omega}_z = 2\pi \times 17.5\text{Hz}$. The total number of atoms in the BEC is on average $N_{\text{BEC}} = 4.2(7) \cdot 10^4$.

The density in the magnetic trap can also be approximated with a Thomas-Fermi profile

$$n'(\mathbf{r}) = \max\left(0, \frac{\mu'}{U_0} \left[1 - \frac{x^2}{x_0^2} - \frac{y^2}{y_0^2} - \frac{z^2}{z_0^2}\right]\right), \quad (3.9)$$

where the chemical potential is [46]

$$\mu' = \frac{15^{2/5}}{2} \left(\frac{aN_{\text{BEC}}}{l'}\right)^{2/5} \hbar\omega' \approx h \times 1.08\text{kHz}. \quad (3.10)$$

The geometric mean trapping frequency is $\omega' = (\bar{\omega}_x \bar{\omega}_y \bar{\omega}_z)^{1/3} \approx 2\pi \times 88.8\text{Hz}$ and the effective oscillator length is $l' = \sqrt{\hbar/m\omega'} \approx 1.16\mu\text{m}$. The background scattering length is $a = 100a_{\text{B}}$ [51], where a_{B} is the Bohr radius. The resulting Thomas-Fermi radii are $x_0 = y_0 = 2.51\mu\text{m}$ and $z_0 = 28.7\mu\text{m}$. Denoting the lattice constant as $b = \lambda/2 \approx 0.46\mu\text{m}$, we see that the BEC in the magnetic trap extends over $2y_0/b \approx 11$ lattice sites.

We can now find the density distribution along the lattice direction by integrating Eq. (3.9) along $x = ux_0$ and $z = vz_0$

$$\begin{aligned} n'(y) &= \frac{\mu'x_0z_0}{U_0} \int \int dudv \left[1 - u^2 - v^2 - \frac{y^2}{y_0^2}\right] \\ &= \frac{2\pi\mu'x_0z_0}{U_0} \int_0^{\sqrt{1-\frac{y^2}{y_0^2}}} dw w \left[1 - w^2 - \frac{y^2}{y_0^2}\right] \\ &= \frac{\pi\mu'x_0z_0}{2U_0} \left[1 - \frac{y^2}{y_0^2}\right]^2. \end{aligned} \quad (3.11)$$

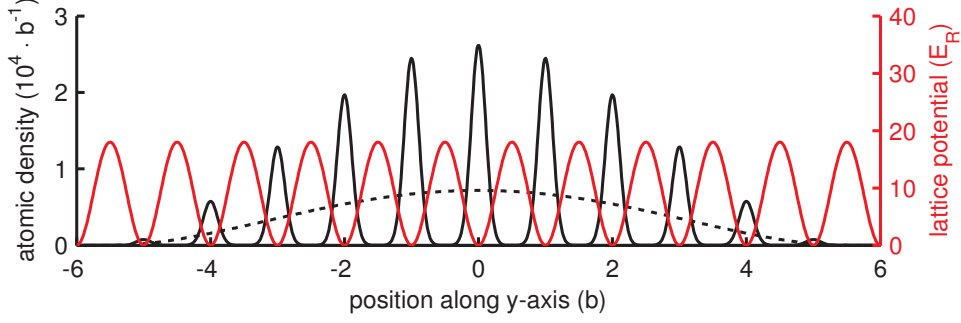


Figure 3.1: Illustration of the lattice loading. The atomic density in the magnetic trap Eq. (3.11) is shown with black dotted line and the density in the lattice Eq. (3.13) is shown with black solid line. The red solid line shows the lattice potential referring to the right hand vertical axis.

The number of particles N_j in the j -th lattice site, centred at $y = jb$, can be found by integration over the extent of a single site

$$N_j = \int_{-b/2}^{+b/2} n'(y - jb) dy \approx n'(jb)b = \frac{\pi\mu'x_0z_0b}{2U_0} \left[1 - \left(\frac{jb}{y_0} \right)^2 \right]^2, \quad (3.12)$$

where we have assumed that $n'(y)$ is a slowly varying function and can be approximated with its value at the centre of each site. The resulting atomic density in the lattice

$$n(y) = \sum_{j=-5}^5 N_j |\phi(y - jb)|^2 \quad (3.13)$$

employing Eq. (3.2) is shown in Fig. 3.1.

In the central lattice site, the number of atoms is $N_0 \approx 7180$, the chemical potential based on Eq. (3.8) is $\tilde{\mu} \approx h \times 1.44\text{kHz}$ and the Thomas-Fermi radius is $\rho_0 \approx 11.6\mu\text{m}$.

3.2 Theory of 2D wave packet excitations

Control of excitations

The individual spin components of the condensate can have different potential energy due to interaction with external fields. Change of the spin state in a scattering process may therefore require to deliver or dissipate energy, depending on the sign of the interaction. Since the total spin has to be conserved, the spin change in a two particle collision process is always opposite.

The linear Zeeman shift does not influence the energy balance, since the energy change for the spin increased component $E_+ - E_0$ exactly cancels the one for spin decrease $E_- - E_0$. The next order, quadratic, correction is due to breaking of the hyperfine manifold into the fine structure [41]. Taking energy of the $m_F = 0$ state as a reference, the quadratic Zeeman shift for $J = 1/2$ can be expressed as [52]

$$E_q(m_F) = (-1)^{F+1} \frac{(g_J - g_I)^2 (\mu_B m_F B_z)^2}{\Delta E_{\text{HFS}} (2I + 1)^2} \equiv q m_F^2, \quad (3.14)$$

where g_J and g_I are g -factors for the electron and nuclear angular momentum and ΔE_{HFS} is the separation of the hyperfine ground states. For ^{87}Rb in the $F = 2$ manifold this gives

$$q = -h \times 71.83 \text{Hz/G}^2 \times B_z^2. \quad (3.15)$$

Since this quantity is negative, a condensate prepared in $m_F = 0$ state will generate pairs of $m_F = 1$ and $m_F = -1$ atoms while releasing energy ($-q$) per particle. The choice of magnetic field determines the magnitude of this excess scattering energy and selects the motional states that are populated in the scattering process.

In a similar fashion, microwave dressing applied on the hyperfine transition can alter the potential energy of a single m_F component [53]. In this way, a collisional excess energy can be created even in a hyperfine manifold with a positive quadratic Zeeman shift, such as $F = 1$ in ^{87}Rb [54].

Field Hamiltonian

In our experiments, the cloud is initially prepared in the state $|F = 2, m_F = 0\rangle \equiv |m_F = 0\rangle$. For short evolution times, only a single scattering channel

$$2 \times |m_F = 0\rangle \leftrightarrow |m_F = 1\rangle + |m_F = -1\rangle \quad (3.16)$$

needs to be considered. The scattering process

$$2 \times |m_F = 0\rangle \leftrightarrow |m_F = 2\rangle + |m_F = -2\rangle \quad (3.17)$$

has a negligible rate due to vanishing Clebsh-Gordan coefficients [37], and the process

$$2 \times |m_F = \pm 1\rangle \leftrightarrow |m_F = \pm 2\rangle + |m_F = 0\rangle \quad (3.18)$$

is neglected due to low population in $|m_F = \pm 1\rangle$. We further assume that the depletion of the main condensate can be neglected, and the main cloud can be described by a wavefunction $\psi_0(\boldsymbol{\rho}, t) = \sqrt{n_0(\boldsymbol{\rho})} e^{-i\mu t}$, where $n_0(\boldsymbol{\rho})$ is the 2D ground state density from Eq. (3.5). The $|m_F = \pm 1\rangle$ components have to be described by quantum fields $\hat{\psi}_{\pm 1}$.

The field Hamiltonian describing the three dimensional excitations [37] can be reduced to two dimensions in a fashion similar to Eq. (3.3), which gives

$$\hat{H} = \hat{H}_I + \sum_{m_F=\pm 1} \hat{H}_{m_F}, \quad (3.19)$$

$$\hat{H}_I = \int d\boldsymbol{\rho} \tilde{U}_1 n_0(\boldsymbol{\rho}) [\hat{\psi}_1^\dagger \hat{\psi}_{-1}^\dagger + \hat{\psi}_1 \hat{\psi}_{-1}] \quad (3.20)$$

$$\hat{H}_{m_F} = \int d\boldsymbol{\rho} \hat{\psi}_{m_F}^\dagger [\hat{H}_{\text{eff}} + q] \hat{\psi}_{m_F} \quad (3.21)$$

where the effective Hamiltonian of the motional energy is

$$\hat{H}_{\text{eff}} = -\frac{\hbar^2}{2m} \nabla^2 + V(\boldsymbol{\rho}) + (\tilde{U}_0 + \tilde{U}_1) n_0(\boldsymbol{\rho}) - \tilde{\mu} \quad (3.22)$$

and $(-q)$ is the excess scattering energy due to the quadratic Zeeman shift. Similar to Eq. (3.4), the 2D interaction strengths ($j = 0, 1$) are

$$\tilde{U}_j = \frac{U_j}{l_z \sqrt{2\pi}} = \frac{4\pi \hbar^2 a_j}{m} \frac{1}{l_z \sqrt{2\pi}} \quad (3.23)$$

with the s -wave scattering lengths¹ $a_0 = 96.9a_B$ and $a_1 = 3.97a_B$.

Position space picture

The interaction term (3.20) represents the scattering process (3.16). Particles in the $m_F = \pm 1$ fields are either simultaneously created or annihilated. If this term alone was determining the evolution, fields at different points in space would be independent of each other and an analytic solution could be found. This type of system is usually solved by a Bogoliubov transformation [46, 37]. However, when only the Hamiltonian \hat{H}_I is present, the solution can also be guessed.

Assuming that the field operators at equal times fulfil the commutation relations

$$[\hat{\psi}_j(\boldsymbol{\rho}), \hat{\psi}_k^\dagger(\boldsymbol{\rho}')] = \delta_{jk} \delta(\boldsymbol{\rho} - \boldsymbol{\rho}') \quad (3.24)$$

for $j, k = \pm 1$, the time evolution in the Heisenberg picture is given by

$$\begin{aligned} i\hbar \frac{\partial \hat{\psi}_j(\boldsymbol{\rho})}{\partial t} &= [\hat{\psi}_j(\boldsymbol{\rho}), \hat{H}_I] \\ &= \int d\boldsymbol{\rho}' \tilde{U}_1 n_0(\boldsymbol{\rho}') [\hat{\psi}_j(\boldsymbol{\rho}), \hat{\psi}_1^\dagger(\boldsymbol{\rho}') \hat{\psi}_{-1}^\dagger(\boldsymbol{\rho}')] \\ &= \int d\boldsymbol{\rho}' \tilde{U}_1 n_0(\boldsymbol{\rho}') \hat{\psi}_{-j}^\dagger(\boldsymbol{\rho}') \delta(\boldsymbol{\rho} - \boldsymbol{\rho}') \\ &= \tilde{U}_1 n_0(\boldsymbol{\rho}) \hat{\psi}_{-j}^\dagger(\boldsymbol{\rho}). \end{aligned} \quad (3.25)$$

¹The constants $a_0 = (7a'_0 + 10a'_2 + 18a'_4)/35$ and $a_1 = (-7a'_0 - 5a'_2 + 12a'_4)/35$ were derived in ref. [37]. The s -wave scattering lengths a'_F of the channel with total spin F can be found in ref. [55]; $a'_0 = 88.2a_B$, $a'_2 = 93.7a_B$ and $a'_4 = 102.1a_B$.

Therefore, the operator $\hat{\psi}_1(\boldsymbol{\rho})$ couples only to $\hat{\psi}_{-1}^\dagger(\boldsymbol{\rho})$, while $\hat{\psi}_{-1}(\boldsymbol{\rho})$ couples to $\hat{\psi}_1^\dagger(\boldsymbol{\rho})$. It can be easily verified that the solution to the above is

$$\hat{\psi}_j(\boldsymbol{\rho}, t) = \hat{\psi}_j(\boldsymbol{\rho}, 0) \cos(i\tilde{\omega}(\boldsymbol{\rho})t) - \hat{\psi}_{-j}^\dagger(\boldsymbol{\rho}, 0) \sin(i\tilde{\omega}(\boldsymbol{\rho})t), \quad (3.26)$$

where $\tilde{\omega}(\boldsymbol{\rho}) = \tilde{U}_1 n_0(\boldsymbol{\rho})/\hbar$. With both fields prepared in the vacuum state $|0\rangle$, the time dependent particle density in the field is

$$\begin{aligned} n_{\pm 1}(\boldsymbol{\rho}, t) &= \langle 0 | \hat{\psi}_j^\dagger(\boldsymbol{\rho}, t) \hat{\psi}_j(\boldsymbol{\rho}, t) | 0 \rangle \\ &= -\sin^2(i\tilde{\omega}(\boldsymbol{\rho})t) \langle 0 | \hat{\psi}_{-j}(\boldsymbol{\rho}, 0) \hat{\psi}_{-j}^\dagger(\boldsymbol{\rho}, 0) | 0 \rangle \\ &= \sinh^2(\tilde{\omega}(\boldsymbol{\rho})t) \end{aligned} \quad (3.27)$$

For long times, the growth of density would be exponential with a time constant $\tau(\boldsymbol{\rho}) = \frac{1}{2\tilde{\omega}(\boldsymbol{\rho})}$. For short evolution times we can approximate $\sinh \phi \approx \phi$ and write

$$n_{\pm 1}(\boldsymbol{\rho}, t) \approx \left(\frac{\tilde{U}_1 t}{\hbar} \right)^2 n_0^2(\boldsymbol{\rho}). \quad (3.28)$$

We could now proceed and substitute for $n_0(\boldsymbol{\rho})$ from our previous result (3.6), however, we only wish to point out here that due to the second power on $n_0(\boldsymbol{\rho})$, the characteristic width of the excitations can be approximated as ²

$$\sigma_{\pm 1} \approx \sigma_0 / \sqrt{2}, \quad (3.29)$$

where $\sigma_0 \equiv \sqrt{\langle x^2 \rangle}$ is the characteristic width of the main cloud distribution $n_0(\boldsymbol{\rho})$, which can be estimated³ by $\sigma_0 \approx 0.41\rho_0$.

Momentum space picture

The evolution due to the interaction Hamiltonian (3.20) can also be analysed in the momentum space. Decomposing the field on its Fourier components

$$\hat{\psi}_j(\boldsymbol{\rho}) = \int d\mathbf{k} e^{i\mathbf{k}\boldsymbol{\rho}} \hat{a}_{j\mathbf{k}}, \quad (3.30)$$

where $\hat{a}_{j\mathbf{k}}$ annihilates particles with momentum $\hbar\mathbf{k}$ in the spinor component $m_F = j$, and substituting into Eq. (3.20), we can write

$$\begin{aligned} \hat{H}_I &= \tilde{U}_1 \iiint d\mathbf{k} d\mathbf{k}' d\boldsymbol{\rho} n_0(\boldsymbol{\rho}) [e^{-i(\mathbf{k}+\mathbf{k}')\boldsymbol{\rho}} \hat{a}_{1\mathbf{k}}^\dagger \hat{a}_{-1\mathbf{k}'}^\dagger + \text{h.c.}] \\ &= \tilde{U}_1 \iiint d\mathbf{k} d\mathbf{k}' [\tilde{n}_0(\mathbf{k} + \mathbf{k}') \hat{a}_{1\mathbf{k}}^\dagger \hat{a}_{-1\mathbf{k}'}^\dagger + \text{h.c.}], \end{aligned} \quad (3.31)$$

²This relation is true exactly when $n_0(\boldsymbol{\rho})$ is a Gaussian.

³This was done by evaluating standard deviation for the marginal distribution $n_0(x) = \int n_0(x, z) dz$ for density from Eq. (3.6).

where h.c. denotes hermitian conjugate of the preceding term, and the density Fourier transform image is

$$\tilde{n}_0(\mathbf{k}) = \frac{1}{(2\pi)^2} \int d\boldsymbol{\rho} e^{-i\mathbf{k}\boldsymbol{\rho}} n_0(\boldsymbol{\rho}). \quad (3.32)$$

If $n_0(\boldsymbol{\rho})$ was a Gaussian with variance σ_0^2 , its Fourier transform would also be a Gaussian, located at $\mathbf{k} = 0$ and having a variance $\sigma_k^2 = 1/\sigma_0^2$. In consequence, the interaction term (3.31) implies that the momenta of the scattered particles are anti-correlated $\mathbf{k} \approx -\mathbf{k}'$ with uncertainty $\sim \sigma_k/\sqrt{2} \approx 1/\sqrt{2}\sigma_0$, where we have assumed that, similar to Eq. (3.28), the scattering is proportional to $|\tilde{n}_0(\mathbf{k})|^2$. Once an $m_F = 1$ particle with momentum \mathbf{k} is detected, there exists a wave packet of $m_F = -1$ particle with mean momentum $-\mathbf{k}$ and spread $\sim 1/\sqrt{2}\sigma_0$.

The individual wave packets also have to obey an uncertainty relation $\Delta x \Delta k \geq 1/2$ which from Eq. (3.28) implies

$$\sigma_{\pm 1k} \geq \frac{1}{2\sigma_{\pm 1}} \approx \frac{1}{\sqrt{2}\sigma_0} \approx \frac{1}{0.41\sqrt{2}\rho_0} \quad (3.33)$$

for their spread in the \mathbf{k} -space.

Kinetic evolution

The Hamiltonian (3.22) describes the kinetic and potential energy of the field. The potential energy terms can be cast into

$$V_{\text{eff}}(\boldsymbol{\rho}) = V(\boldsymbol{\rho}) + (\tilde{U}_0 + \tilde{U}_1)n_0(\boldsymbol{\rho}) - \tilde{\mu}. \quad (3.34)$$

Inserting for $n_0(\boldsymbol{\rho})$ from (3.6), we obtain

$$V_{\text{eff}}(\boldsymbol{\rho}) = \tilde{\mu} \left[1 - \left(\frac{\rho}{\rho_0} \right)^2 \right] \times \begin{cases} \frac{\tilde{U}_1}{\tilde{U}_0}, & \rho \leq \rho_0 \\ -1, & \rho > \rho_0 \end{cases} \quad (3.35)$$

Since $\frac{\tilde{U}_1}{\tilde{U}_0} \approx 4.1\%$ is small, the potential is nearly flat in the range $\rho \leq \rho_0$ and can be approximated with a box or a hard wall cylinder, where the motional eigenstates are Bessel functions [37]. The quality of this approximation can be verified by numerical diagonalisation of the Hamiltonian (3.22). Figure 3.2 shows the energy of the eigenstates obtained by diagonalisation of the Hamiltonian on a finite point grid in space⁴ for the central lattice site ($\tilde{\mu} = h \times 1.44\text{kHz}$). We see that until mode number $n \sim 300$, the total energy grows roughly linearly with $\sim 1.3\text{Hz}$ per mode spacing. The kinetic energy clearly dominates over the potential energy, which justifies the cylindrical box approximation.

⁴The kinetic term $\nabla^2\psi$ was approximated as $[-4\psi_{jk} + \psi_{j+1k} + \psi_{j-1k} + \psi_{jk+1} + \psi_{jk-1}]/d^2$, where d is the grid constant and j, k are the 2D grid indexes.

The right side of Fig 3.2 shows position and momentum space probability distributions for few selected eigenstates. Interestingly, the first 11 modes populate only the outer rim in the space due to repulsion of the main condensate. These states correspond to a standing waves on a ring distinguished by a different number of nodes along the circumference. The low density overlap with the main cloud will cause relatively weak scattering into those states.

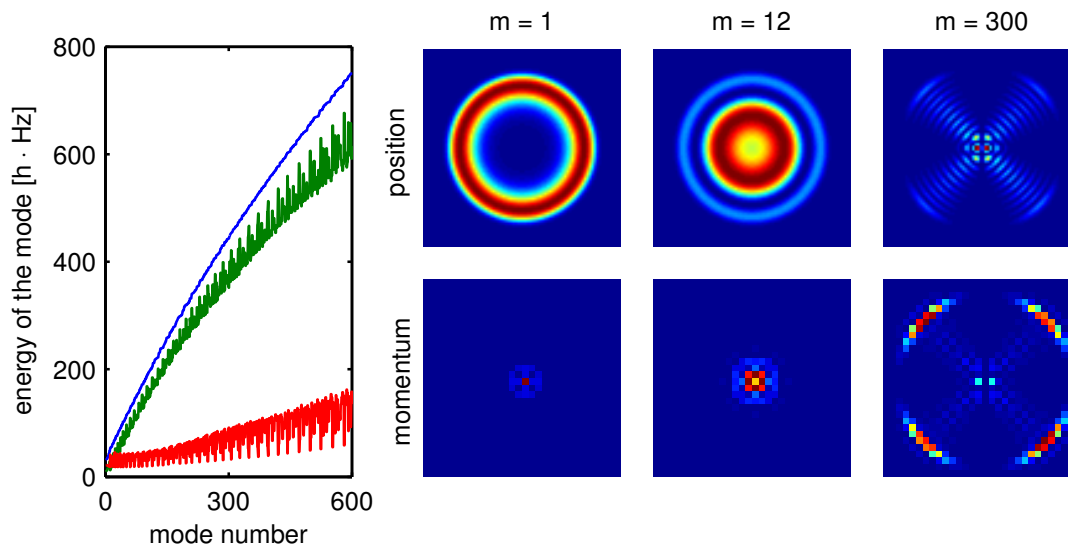


Figure 3.2: Eigenstates of the motional Hamiltonian (3.22) for the central lattice site. The left graph shows the total, kinetic and potential energy of the eigenstates with blue, green and red curve respectively. The images on the right show the probability distribution in position and momentum space for three selected eigenstates.

The Hamiltonian (3.21) influences which modes are excited. Since \hat{H}_{eff} does not contain time varying terms, the mean energy of the system has to remain zero, and the scattering can occur only to motional modes whose energy is close to $(-q)$. To see this, we can approximate $n_0(\boldsymbol{\rho})$ in Eq. (3.20) with its average

$$\tilde{U}_1 n_0(\boldsymbol{\rho}) \rightarrow \tilde{U}_1 \bar{n}_0 = \frac{\tilde{U}_1}{\pi \rho_0^2} \int d\boldsymbol{\rho} n_0(\boldsymbol{\rho}) = \frac{\tilde{U}_1 N_0}{\pi \rho_0^2} \equiv \tilde{\Omega}, \quad (3.36)$$

which introduces an effective scattering rate $\tilde{\Omega}$. The field can be expanded on the motional eigenstate basis

$$\hat{H}_{\text{eff}} \phi_m(\boldsymbol{\rho}) = \epsilon_m \phi_m(\boldsymbol{\rho}), \quad (3.37)$$

$$\hat{\psi}_j(\boldsymbol{\rho}) = \sum_m \hat{a}_{jm} \phi_m(\boldsymbol{\rho}), \quad (3.38)$$

where \hat{a}_{jm} annihilates particle with spin $m_F = j$ in the eigenmode m . Provided that the states $\phi_m(\boldsymbol{\rho})$ are chosen to be real, their orthonormality allows us to write Eq. (3.19) in the form

$$\hat{H} = \sum_m \left(\tilde{\Omega} [\hat{a}_{1m}^\dagger \hat{a}_{-1m}^\dagger + \hat{a}_{1m} \hat{a}_{-1m}] + (\epsilon_m + q) [\hat{a}_{1m}^\dagger \hat{a}_{1m} + \hat{a}_{-1m}^\dagger \hat{a}_{-1m}] \right). \quad (3.39)$$

In this approximation, each mode is independent and the Heisenberg equation of motion for the creation and annihilation operators is

$$i\hbar \frac{d}{dt} \begin{pmatrix} \hat{a}_{1m} \\ \hat{a}_{-1m}^\dagger \end{pmatrix} = \begin{pmatrix} (\epsilon_m + q) & \tilde{\Omega} \\ -\tilde{\Omega} & -(\epsilon_m + q) \end{pmatrix} \begin{pmatrix} \hat{a}_{1m} \\ \hat{a}_{-1m}^\dagger \end{pmatrix}. \quad (3.40)$$

For $\epsilon_m + q < \tilde{\Omega}$, the eigenvalues of this system,

$$\mathcal{E}_m = \pm \sqrt{(\epsilon_m + q)^2 - \tilde{\Omega}^2}, \quad (3.41)$$

are imaginary, and an exponential growth of population in the mode m ensues⁵, see Eq. (3.27). Since the growth is maximal for $\epsilon_m = -q$, the choice of the external field q selects the total energy of the modes (potential plus kinetic).

Provided the spatial density of the wave packets can be approximated by Eq. (3.28) (irrespective of their momenta), the expectation value of the potential energy per particle is

$$\langle \hat{V}_{\text{eff}} \rangle = \frac{1}{N_{\pm 1}} \int d\boldsymbol{\rho} V_{\text{eff}}(\boldsymbol{\rho}) n_{\pm 1}(\boldsymbol{\rho}) \approx h \times 44.3\text{Hz}, \quad (3.42)$$

here evaluated for the central lattice site. Therefore, the mean kinetic energy of the wave packets should be

$$E_K = p^2/2m = \max[0, (-q) - \langle \hat{V}_{\text{eff}} \rangle]. \quad (3.43)$$

This implies that there is a cut-off in $(-q)$ below which the wave packets do not move.

The wave packet population is amplified only if all its composite modes are simultaneously resonant, implying that the wavepacket's energy uncertainty should be smaller than $\tilde{\Omega}$. Through error propagation, we can determine the energy uncertainty

$$\Delta E_K = \Delta p \frac{p}{m} = \hbar \Delta k \sqrt{\frac{-2(q + \langle \hat{V}_{\text{eff}} \rangle)}{m}}. \quad (3.44)$$

Inserting Δk from Eq. (3.33), and using a typical experimental value $(-q)/h = 300\text{Hz}$, we obtain $\Delta E_K = h \times 36.5\text{Hz}$ in the central lattice site, which is of the same order as $\tilde{\Omega} = h \times 29.6\text{Hz}$.

⁵Assuming that the fields are initialised in the vacuum state.

3.3 Observation of spinor wave packets

Experimental sequence

We prepare a BEC in a magnetic trap by a forced RF evaporative cooling and load the atoms into the optical lattice by a simultaneous ramp-down of the magnetic trap and a ramp up of the lattice over 110 ms. This is performed in the $|F = 2, m_F = 2\rangle$ state. Once the BEC is optically trapped, a bias magnetic field $B_z = 285\text{mG}$ is applied, and the atoms are transferred into $|F = 2, m_F = 0\rangle$ using two microwave pulses⁶. Immediately afterwards, a bias magnetic field along the y -axis is applied using a linear ramp lasting 1 ms, which produces the target quadratic Zeeman shift and initiates the spin changing collisions.

The evolution time was chosen to be 8 ms, which is just before the growth of population ceases to be exponential and depletion of the main condensate starts to play a role [50]. The lattice is turned off abruptly initiating a 20 ms time-of-flight. In the first 5 ms, a Stern-Gerlach (SG) pulse of inhomogeneous magnetic field is applied in the z -direction using the Ioffe coil. This provides the magnetic components with a different momentum impulse and leads to their separation in free fall.

The spin components are imaged along the y -direction, that is along the lattice, using standard absorption imaging. This allows us to probe the momentum distribution in the transverse degrees of freedom. Along the lattice direction, the clouds from the individual sites expand very fast, which on a microsecond time scale⁷ overlaps their densities and washes out all information about the site origin of the atoms. We can therefore measure only the combined density of all lattice sites.

Spinor populations

Figure 3.3 shows the average population fraction in the $m_F = \pm 1$ components as a function of the excess scattering energy $(-q)$. We see that the two populations are very well correlated, in accordance with our expectation of equal number scattering into the opposite m_F states. The residual discrepancy can be attributed to the measurement precision and to systematic effects due to spatial inhomogeneity of the imaging beam arising from light interference on the optical elements of the imaging system.

The populations first saturate around $(-q)/h \approx 50\text{Hz}$, which corresponds well with the mean potential energy from Eq. (3.42). Below this value a reduced fraction

⁶First going to $|F = 1, m_F = 1\rangle$ with $12\mu\text{s}$ pulse and then to $|F = 2, m_F = 0\rangle$ with $20\mu\text{s}$ pulse. The residual population in $|F = 2, m_F = 0\rangle$ is pushed out of the view a resonant light along the z -axis between the two microwave pulses.

⁷For a harmonic ground state, the average velocity is $\bar{v} = \frac{\hbar\sqrt{s}}{2m\lambda} \approx 10.6\frac{\mu\text{m}}{\text{ms}}$ based on $\frac{1}{2}m\bar{v}^2 = \frac{1}{4}\hbar\omega_y$.

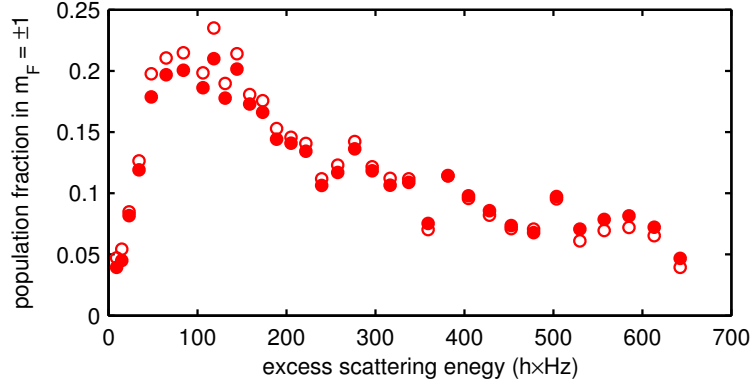


Figure 3.3: Average population fraction in the $m_F = -1$ (full circles) and $m_F = 1$ (empty circles) components over ~ 6 experimental repetitions as a function of the excess scattering energy ($-q$).

of atoms is addressed: the scattering is resonant only in the outer regions of the main cloud. As the scattering energy is further increased, the excited wave packets gain kinetic energy and begin to translate during the spinor evolution time. This can deplete the region with the maximal excitation rate, and therefore reduce the bosonic enhancement of the spin changing collisions. Likely, this caused the decrease of the spinor population with a growing value of ($-q$).

Time-of-flight images

Figure 3.4 shows examples of time-of-flight images for few chosen values of the excess scattering energy. The upper image demonstrates that at a low value of ($-q$), the scattered spinor components do not have any excess kinetic energy and their spatial distribution copies the shape of the main cloud in agreement with Eq. (3.28). We observe that from run to run, the shape of the main cloud varies slightly, possibly depending on the performance of the loading procedure⁸. A picture with a particularly asymmetric main cloud was chosen to demonstrate the correlation.

The lower section of Fig. 3.4 shows examples of $m_F = \pm 1$ clouds with intermediate excess scattering energies $\sim h \times 330\text{Hz}$. Here the anti-correlation of the wave packet momenta is very obvious. In time-of-flight, the initial velocity of the wave packets transforms into position, therefore presence of a ‘blob’ on one side of a spinor cloud implies the existence of a ‘blob’ on the opposite side (centrally symmetric) in the other spinor component. Since all the wave packets have similar kinetic energy, the density forms a ring structure whose radius grows with ($-q$).

⁸For example, a variable heating of the magnetic trap coils can misalign the trap slightly producing an out of equilibrium distribution in the transverse trapping directions of the lattice.

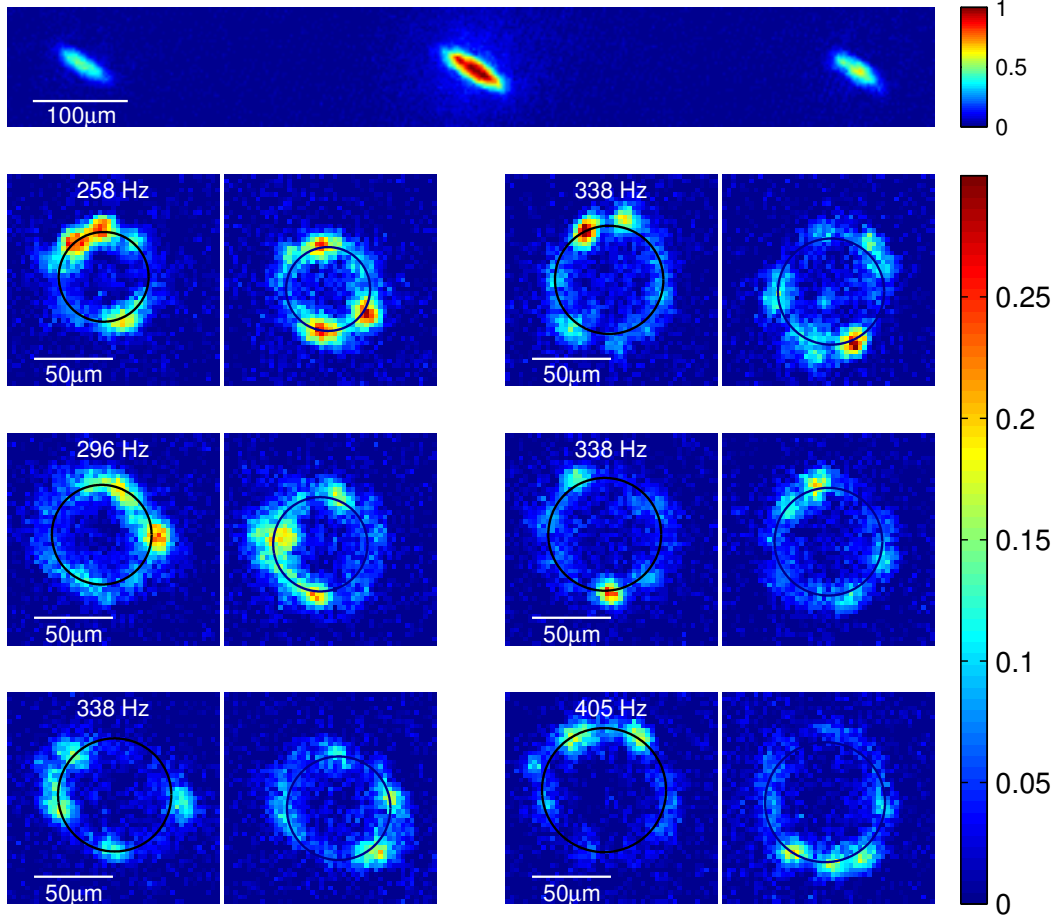


Figure 3.4: Images of spinor wave packets after time-of-flight. Colour encodes the optical density. The upper image demonstrates the Stern-Gerlach separation of the $m_F = -1, 0, 1$ components (left to right) taken at low value of $(-q)/h = 23\text{Hz}$. The pairs of images show the anti-correlated wave packets in the $m_F = -1, 1$ components (left, right) for several $(-q)/h$ values (stated above).

Cloud size

The clouds were fitted with a torus-like density distribution

$$n_{\text{tor}}(x, z) = A \exp \left(-\frac{\left[\sqrt{(x - x_0)^2 + (z - z_0)^2} - r_0 \right]^2}{2\sigma_{\text{tor}}^2} \right), \quad (3.45)$$

where r_0 is the radius, σ_{tor} is the Gaussian width of the torus and x_0, z_0 are the coordinates of its centre. The fit results for r_0 and σ_{tor} are shown in Fig. 3.5 as a function of $(-q)$. Also shown is a simple expectation of the ring size based on

Eq. (3.43) according to which the wave packet position should be

$$r_0 = t_{\text{TOF}}v = t_{\text{TOF}}\sqrt{\frac{2E_K}{m}} = t_{\text{TOF}}\sqrt{\frac{2 \times \max[0, (-q) - \langle \hat{V}_{\text{eff}} \rangle]}{m}}, \quad (3.46)$$

where $t_{\text{TOF}} = 20$ ms is the time-of-flight, and $\langle \hat{V}_{\text{eff}} \rangle = h \times 44.3$ Hz was set to the central lattice site value.

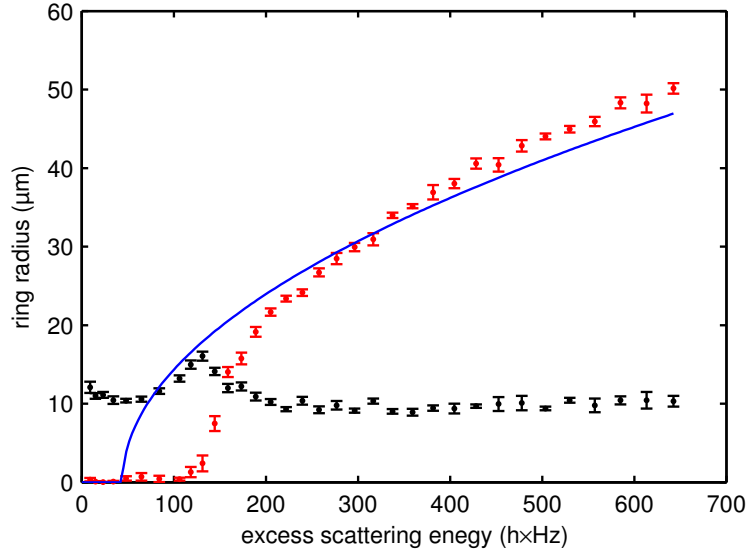


Figure 3.5: Size of the spinor clouds in time-of-flight. Figure shows the fitted values of r_0 (red) and σ_{tor} (black) from Eq. (3.45) as a function of the excess scattering energy $(-q)$. The error bars denote the standard deviation of the mean taken over ~ 6 experimental realizations and both $m_F = \pm 1$ clouds. Shown with a blue solid curve is the expectation of r_0 based on Eq. (3.46).

Taking into account the following consideration, the theory curve is in good agreement with the experiment. When the radius of the torus is smaller than its width, it cannot be resolved by the fit, however we can see an increase in σ_{tor} when r_0 becomes comparable. Once r_0 grows above σ_{tor} , the two parameters can again be clearly distinguished, and the width of the torus drops to back to $\sim 10 \mu\text{m}$. For chosen value of t_{TOF} , the ring structure emerges around $(-q)/h = 200$ Hz.

At high values of $(-q)$, we can see a slight discrepancy: the rings are bigger than the theory curve. Perhaps this could be caused by an additional impulse due to mean field expansion immediately after the release from the lattice, or the fact that the wave packets are already displaced from the centre before the release: ~ 1 ms increase in the effective t_{TOF} would explain the discrepancy (5% error relative to t_{TOF}). To illustrate the fit results, the torus radii were drawn as black circles in Fig. 3.4.

Number of wave packets

From the toroidal fit we also obtain coordinates of the cloud centre (x_0, z_0) , which allows us to define a polar coordinates system (r, θ) centred at this point and extract the angular distribution

$$n(\theta)_{\pm 1} = \int_0^{r_0 + \sigma_{\text{tor}}} n_{\pm 1}(r, \theta) r dr. \quad (3.47)$$

Figure 3.6 shows an example of the angular distributions, here taken for the low left corner image pair in Fig. 3.3, $(-q)/h = 338$ Hz. The distribution for $m_F = 1$ (red dotted line) was rotated by π to highlight the correlation with the $m_F = -1$ distribution (black solid line).

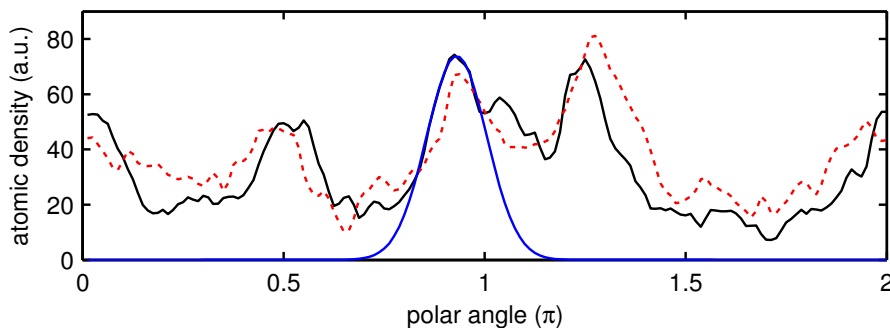


Figure 3.6: Example of angular distribution from Eq. (3.47) evaluated for the low left corner image pair in Fig. 3.3, $(-q)/h = 338$ Hz. The black solid line shows the distribution for $m_F = -1$, the red dotted line shows distribution for $m_F = 1$ rotated by π . The blue solid line shows an example of a Gaussian fit to a wave packet in $m_F = -1$.

For each run we make Gaussian fits to the peaks in both $m_F = \pm 1$. Starting from the highest peak, we iteratively subtract the current fit and make a fit to the next highest peak. We then count how many peaks have an amplitude higher than a threshold set by the average height of the highest peaks from $m_F = \pm 1$, separately for individual run.

The results of the wave packet counting are shown in Fig. 3.7 for $(-q)/h > 200$ Hz, where the ring structure is clear. In the range $300 \text{ Hz} < (-q)/h < 500 \text{ Hz}$, both the number of wave packets and their width seem to be constant, with an average occurrence of 5.1 wave packet having $15.1 \mu\text{m}$ width (2σ). Below 300 Hz the wave packets appear to have a slightly bigger size and also seem to have a lower occurrence, which might be caused by a higher probability of wave packet overlap.

The overlap probability can be estimated by

$$P_{\text{over}}(k) = 1 - \prod_{j=1}^{k-1} \left(1 - j \frac{2\sigma}{2\pi r_0} \right), \quad (3.48)$$

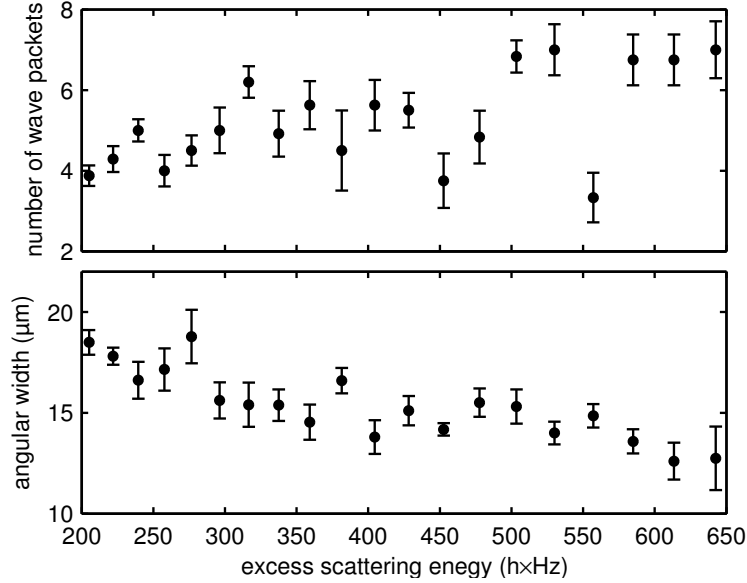


Figure 3.7: Wave packet counting. The upper plot shows the mean number of wave packets with height at least that of the average highest peak from $m_F = \pm 1$ in each individual run. The lower plot shows the mean angular width (2σ) of those wave packets converted into size by the effective radius of the cloud. Both parameters are plotted as a function of the excess scattering energy ($-q$). The error bars show the standard error of the mean.

where the term in the brackets is the probability that $(j + 1)$ -th wave packet hits an ‘empty’ space. For $(-q)/h = 200\text{Hz}$ and wave packet width $2\sigma = 15.1\mu\text{m}$, the overlap probability is $P_{\text{over}}(5) \approx 70\%$, while at $(-q)/h = 400\text{Hz}$ it is $\sim 52\%$. Above 500Hz the wave packet number indicates growth to about 7, but it is difficult to assign a physical relevance to it, because the density of the scattered spin components is very low, and the fits might be misinterpreting residual fringe patterns from the imaging beam.

The observed position uncertainty of the wave packets, $\sigma = 7.5\mu\text{m}$, can now be compared with the theoretical estimates. From Eq. (3.29), we would expect $\sigma_{\pm 1} = 0.41\rho_0/\sqrt{2} \approx 3.35\mu\text{m}$ for the in-trap size, while the to momentum uncertainty implies expansion of the cloud by $\sigma_{\text{TOF}} \equiv \hbar\sigma_{\pm k}t_{\text{TOF}}/m \approx 2.19\mu\text{m}$, where $\sigma_{\pm k}$ is taken from Eq. (3.33). Additionally, the imaging system has a finite resolution evaluated experimentally by measuring the width of $0.5\mu\text{m}$ aperture inserted into the imaging plane, which yielded a point spread function with Gaussian width $\sigma_{\text{img}} = 2.02\mu\text{m}$. Adding these quantities in quadrature we arrive at a minimum size of the wave packet

$$\sigma_{\text{min}} = \sqrt{\sigma_{\pm 1}^2 + \sigma_{\text{TOF}}^2 + \sigma_{\text{img}}^2} \approx 4.48\mu\text{m}. \quad (3.49)$$

Although the order of magnitude is correct, this estimate is still considerably lower

than the observed size. One possible cause could be a mean field expansion of the wave packets due to overlap with the highly repulsive main cloud immediately after the release. Another reason could be that the peak fit function does not include an additive offset parameter, and therefore any background density lifting the wave packets will artificially broaden their size.

Spontaneous symmetry breaking

Since the lattice sites are well isolated, each wave packet must originate from a single lattice site. Referring to Eq. (3.13) and Fig. 3.1, we see that only about 5 lattice sites are populated with an atom number higher than half of the maximum. This implies that each lattice site generates on average one wave packet. Since all directions of scattering are equally likely, a symmetry breaking has to occur in order to amplify population in a wave packet with a particular momentum.

Reference [37] provides arguments for spontaneous symmetry breaking of the cylindrical eigenstate phase and observed randomly chosen orientations of the spinor clouds in the excited motional states. The scattered spinor population is in a two mode squeezed state and measuring the orientation of one m_F component collapses the other into the opposite direction.

An analogous mechanism should be present for wave packet excitations. Before the measurement, the spinor components are in a superposition of many wave packets in all possible directions of the 2D space and only the final measurement collapses the state into a particular direction. This would be true exactly if only one atom was excited into a wave packet. In a condensate, we scatter many atoms, and bosonic stimulation [56] ‘encourages’ the particles to scatter into already populated modes. In the formalism of two mode vacuum squeezed states, the number of particles is highly uncertain in each possible direction of the wave packet propagation. Once the momentum is measured, it is very probable that a single direction will have much higher population than others, which would appear as a single wave packet.

Angular correlations

To quantify the correlation of the wave packet momenta, we have repeated the experiment 54 times at $(-q)/h = 300\text{Hz}$ and evaluated the correlation function

$$\mathcal{C}(\theta) \equiv \frac{\int d\phi n_+(\phi) n_-(\phi - \theta)}{N_+ N_-} \quad (3.50)$$

for each run, where $N_{\pm 1} = \int d\phi n_{\pm 1}(\phi)$ is the number of particles in the $m_F = \pm 1$ components.

Figure 3.8 shows the value of the correlation function obtained by a weighted

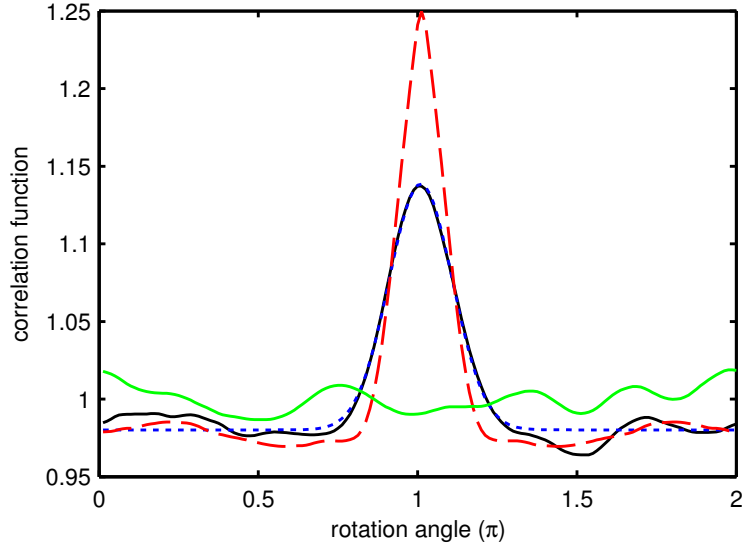


Figure 3.8: Correlation of angular distributions, Eq. (3.50). The black solid line shows the mean correlation of the opposite spin components, and the blue dotted line is its Gaussian fit. The dashed red line is a mean self-correlation function. The green solid line is a mean correlation of the spin components between successive runs.

average over all runs⁹ (black solid line). In accordance with our expectations, the function peaks at $\theta = \pi$. From a Gaussian fit we obtain an angular uncertainty $\Delta\theta = 0.010\pi$, which translates into spatial uncertainty $\sigma_{\text{cor}} = 10.5\mu\text{m}$.

To find out how strong the correlation could be, we also evaluate a mean self-correlation¹⁰ for the $m_F = \pm 1$ components (red dashed line). Position uncertainty of this function, $\sigma_{\text{self}} = 7.41\mu\text{m}$, indicates the mean width of the peak like features in the angular distribution. The self-correlation is effectively a convolution of the function with itself. In case of Gaussian peaks, the width would be broadened by a factor of $\sqrt{2}$. This implies that the position uncertainty for the wave packets is $\sigma_{\text{wp}} = \sigma_{\text{self}}/\sqrt{2} = 5.24\mu\text{m}$, which is close to the theoretical limit set by Eq (3.49).

Finally, an important property to note is that there is only a single peak in both the correlation and self-correlation function implying that the distribution of the wave packets along the circumference is not periodic. To find out if there is some preferred direction for the wave packet emission, we also evaluated the correlation function individually for $m_F = \pm 1$ on pairs of successive runs. The result, plotted in Fig. 3.8 with green solid curve, does not show any signs of correlation, and we can therefore conclude that the wave packets are emitted in random directions.

⁹The total atom number of scattered atoms $N_1 + N_{-1}$ was used as weight coefficient.

¹⁰In this limit the angular distributions for $m_F = \pm 1$ are identical and rotated by π .

Non-destructive Faraday imaging

In this chapter, we will review the effect of Faraday rotation and show a simple implementation of a non-destructive, spatially resolved measurement: the imaging of cold atomic clouds. We analyse analytically the signal-to-noise ratio for common dispersive imaging techniques and show that, including our method of Dark field Faraday imaging (DFFI), all techniques provide a comparable measurement precision.

We examine the properties of DFFI for a wide range of atom numbers and temperatures of the cloud, and present applications of the technique for vector field magnetometry and monitoring of the in-trap cloud motion.

4.1 Faraday rotation

Faraday rotation can be described using a model of the dispersive light-matter interaction [9, 57]. The effective scattering Hamiltonian $\hat{H}_{\text{eff}} = \hat{H}^{(\text{scal})} + \hat{H}^{(\text{vec})}$ consists of a scalar and vector part

$$\hat{H}^{(\text{scal})} = \frac{1}{3}g \sum_{f'} \frac{\alpha_{f,f'}^{(0)}}{\Delta_{f,f'}} \hat{N}_{\text{at}} \hat{N}_{\text{ph}}, \quad (4.1)$$

$$\hat{H}^{(\text{vec})} = \frac{1}{2}g \sum_{f'} \frac{\alpha_{f,f'}^{(1)}}{\Delta_{f,f'}} \hat{F}_z (\hat{N}_+ - \hat{N}_-), \quad (4.2)$$

where \hat{N}_{at} and \hat{N}_{ph} are atom and photon number operators respectively and \hat{F}_z is the component of the collective atomic angular momentum in the direction of light propagation (defines the z -axis). \hat{N}_{\pm} are photon number operators for the two circular polarizations. The field factor is given by $g = \omega/(2\epsilon_0 V)$, where V is the light-atom interaction volume.

The scalar and vector polarizabilities $\alpha_{f,f'}^{(0)}$ and $\alpha_{f,f'}^{(1)}$ characterize the response of an atom to light of frequency ω detuned from an atomic resonance by $\Delta_{f,f'} = \omega - \omega_{f,f'}$, where f and f' denote the initial and final hyperfine states respectively¹. The polarizabilities can be expressed as [57]

$$\alpha_{f,f'}^{(k)} = \alpha_f^{f'} c_k \sqrt{3(2f+1)(2f'+1)} \begin{Bmatrix} f & k & f \\ 1 & f' & 1 \end{Bmatrix}, \quad (4.3)$$

$$c_0 = 1, \quad (4.4)$$

$$c_1 = \sqrt{\frac{2}{f(f+1)}}, \quad (4.5)$$

$$\alpha_f^{f'} = (-1)^{1+f+f'+j+j'+2i} \alpha_0 (2j'+1) \begin{Bmatrix} j' & f' & i \\ f & j & 1 \end{Bmatrix}^2, \quad (4.6)$$

$$\alpha_0 = \frac{3\epsilon_0 \hbar \Gamma \lambda^3}{8\pi^2}. \quad (4.7)$$

Provided the atom number N_{at} is large and all atoms are in the same internal state with average z -axis projection of the angular momentum $\langle \hat{f}_z \rangle$, we can treat the collective angular momentum classically and use $\hat{F}_z = N_{\text{at}} \langle \hat{f}_z \rangle$. To account for the spatial variation of the density, we substitute $N_{\text{at}}/V \rightarrow \rho(\mathbf{r})$. Under these assumptions the circularly polarized photons become the eigenstates of the effective Hamiltonian \hat{H}_{eff} with energies E_{\pm} . The Hamiltonian (4.1) induces the scalar phase shift $\theta_s = \int \frac{1}{2}(E_+ + E_-)dt/\hbar$ used in, e.g., phase contrast imaging (PCI). The rotation of the polarization plane of a linearly polarized beam of light—known as Faraday rotation—arises from a differential phase shift of the two circular components induced by the vector term (4.2) according to $\theta_F = \int \frac{1}{2}(E_+ - E_-)dt/\hbar$.

In our experiments, atoms are prepared in the $|f=2, m_f=2\rangle$ state of ^{87}Rb , and for imaging wavelengths close to the D2 line, the spatially resolved Faraday angle is given by

$$\theta_F(x, y) = \frac{\langle \hat{f}_z \rangle \Gamma \lambda^2}{16\pi \Delta_{\text{eff}}} \int \rho(\mathbf{r}) dz = c_F(\Delta_{\text{eff}}) \tilde{\rho}(x, y), \quad (4.8)$$

where Γ is the natural linewidth, λ is the wavelength of the imaging light and the effective detuning is given by

$$\frac{1}{\Delta_{\text{eff}}} = \frac{1}{20} \left(\frac{28}{\Delta_{2,3}} - \frac{5}{\Delta_{2,2}} - \frac{3}{\Delta_{2,1}} \right). \quad (4.9)$$

For later convenience, we write the spatially dependent angle of polarization as a product of a Faraday coefficient $c_F(\Delta_{\text{eff}})$ and the column density of the sample $\tilde{\rho}(x, y)$.

¹In this chapter, we use lower case letters to denote the electronics states of individual atoms. The upper case letters are used to denote collective quantity.

4.2 Dark field Faraday imaging

Fig. 4.1 schematically shows the experimental system to measure the angle of polarization. When a beam of linearly polarized light impinges on a cloud of magnetically oriented atoms, a spatial rotation pattern is imprinted on the beam. The polarization pattern is collimated and the two linear components are subsequently separated on a polarizing beam splitter (PBS). The polarization of the imaging beam is chosen such that its transmission through the PBS is minimized in the absence of atoms. A second lens then forms an image in the detection system, which contains a mask to allow for partial readout and thereby high frame rates in an Electron Multiplying Charge Coupled Device (EMCCD) camera. This camera enables low light intensity imaging and hence reduced measurement destructiveness by decreasing sensitivity to the readout noise of the camera. This feature is crucial for repeated probing and feedback experiments, but comes at the expense of an amplification of the shot noise of the detected light by a factor of $\sqrt{2}$, which can be a severe limitation in applications with low signal-to-noise.

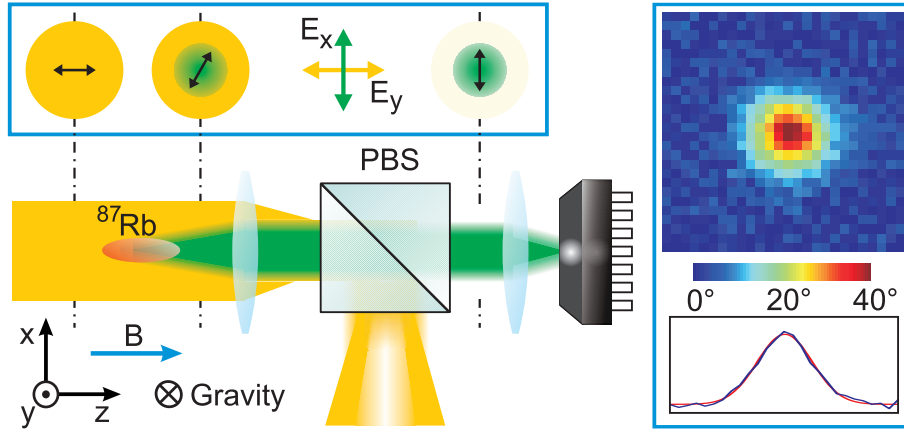


Figure 4.1: Sketch of the Faraday imaging system and a resulting image (right) at $T = 1.5 \mu\text{K}$ and $N = 10^6$ atoms. The polarization of the light is indicated (top left) by displaying cross sections of the imaging beam obtained from a rotation around the dash-dot lines.

The reconstruction of the rotation angle requires knowledge of the intensities of the incoming and rotated light. In principle this can be achieved by measuring the intensity of the light reflected by the PBS as well as the transmitted portion. In our realization, however, we avoid the necessary cross-calibration this would entail, by making use of the technical imperfection of the PBS, which leads to a finite transmission of the non-rotated light. Thus, images without atoms can be used to determine the incoming light intensity and compensate for beam profile

inhomogeneity. The transmitted light intensity is given by

$$I(\theta_F) = I_0 \frac{\sin^2 \theta_F + \text{CS} \cos^2 \theta_F}{1 + \text{CS}}, \quad (4.10)$$

where I_0 is the incident intensity on atoms. We measure the cube suppression

$$\text{CS} = I(0)/I(\pi/2) \approx 1.5 \cdot 10^{-3} \quad (4.11)$$

as the ratio of minimum to maximum light intensity transmitted through the PBS for a manually scanned polarization angle. The Faraday rotation angle can be obtained from

$$\sin^2 \theta_F = \left(\frac{I(\theta_F)}{I(0)} - 1 \right) \left(\frac{\text{CS}}{1 - \text{CS}} \right). \quad (4.12)$$

An absolute light intensity calibration is therefore not required to evaluate the rotation angle, as long as the EMCCD camera has a linear response.

4.3 Signal-to-noise analysis of dispersive imaging techniques

In this section we examine the signal-to-noise ratio (SNR) of the four common dispersive imaging techniques. Two methods use the scalar phase shift θ_s induced by the Hamiltonian (4.1), namely dark field scalar imaging (DFSI) and phase contrast imaging (PCI), and two methods are based on a phase shift θ_F arising from the vector Hamiltonian (4.2), namely DFFI and dual port Faraday imaging (DPFI) [17]. To allow for a generalized treatment, we define a normalized signal $S(\theta) \equiv I(\theta)/I_0$, where θ is a phase shift, and $I(\theta)$ and I_0 are the detected and the incident light intensities, respectively.

General SNR analysis

The individual pixel values of the acquired image are subject to several sources of noise. There is technical noise, such as the readout noise of the camera, thermally induced dark counts, clock induced charges (CIC), and classical noise coming from unstable light intensity or vibrations of the optical elements. All these sources of noise depend on the particular implementation and can be minimized by a careful design of the imaging system. On the other hand, noise coming from the quantum character of the light (shot noise) cannot be eliminated and often becomes the main source of noise.

Non-destructive imaging generally requires low light intensities and thus measurement of signals comparable to the readout noise of the camera. The readout

noise magnitude increases with the readout frequency, a decisive parameter for the frame rate of continuous acquisition. Preceding the readout amplifier with an electron multiplying (EM) register amplifies the signal and improves the sensitivity of an EMCCD camera to the single photon level, even using fast readout. Unfortunately, due to the random sequential character of the EM gain, any noise already present in the picture (such as the shot noise) will be amplified by about a factor of $\sqrt{2}$ [58, 59]. The use of EM gain becomes profitable when the number of electrons N_{el} accumulated on a given pixel of the CCD is smaller than the readout noise variance.

For dispersive imaging techniques, the SNR due to shot noise can be calculated using

$$N_{\text{el}} = \eta N_{\text{ph},0} S(\theta), \quad (4.13)$$

where $N_{\text{ph},0}$ is the number of atom incident photons per physical pixel area, i.e., the area of a pixel in the imaging plane. The detection efficiency η takes into account light losses in the imaging system as well as the quantum efficiency of the CCD. Assuming poissonian statistics for the signal, $(\Delta N_{\text{el}})^2 = N_{\text{el}}$. The signal error becomes

$$\Delta S = \left| \frac{dS}{dN_{\text{el}}} \right| \Delta N_{\text{el}} = \frac{\sqrt{\eta N_{\text{ph},0} S(\theta)}}{\eta N_{\text{ph},0}} = \sqrt{\frac{S(\theta)}{\eta N_{\text{ph},0}}}. \quad (4.14)$$

As such, the EM gain $\sqrt{2}$ noise amplification effectively reduces the detection efficiency η by a factor of 2.

To quantify the destructiveness of the imaging, we relate the number of incident photons to the photon absorption probability per atom

$$P_{\text{abs}} \approx \frac{N_{\text{ph},0} \sigma_0}{A \delta^2}, \quad (4.15)$$

where A is the physical pixel area and σ_0 is the effective scattering cross-section (for a two level atom, $\sigma_0 = \frac{3\lambda^2}{2\pi}$). The above equation is valid in the large detuning limit $\delta \equiv \frac{\Delta}{\Gamma/2} \gg 1$, which is often required to reduce diffraction effects. In the following we assume this regime.

Employing equation (4.15), the error in the measured phase shift becomes

$$\Delta \theta = \left| \frac{d\theta}{dS} \right| \Delta S = \left| \frac{d\theta}{dS} \right| \frac{\sqrt{S(\theta)}}{|\delta| \sqrt{\eta P_{\text{abs}} A / \sigma_0}}. \quad (4.16)$$

Using the off-resonant scalar phase shift formula [7]

$$\theta_s = \frac{\sigma_0}{2\delta} \tilde{\rho}, \quad (4.17)$$

where $\tilde{\rho}$ is the atomic column density (see Eq. (4.8)), we can eliminate the explicit detuning dependence in Eq. (4.16), casting it into

$$\Delta\theta = \left| \frac{d\theta}{dS} \right| \frac{2|\theta_s| \sqrt{S(\theta)}}{\tilde{\rho} \sqrt{\eta P_{\text{abs}} A \sigma_0}}. \quad (4.18)$$

Since $\theta \propto \tilde{\rho}$, the atom number measurement precision is determined by the signal-to-noise ratio in the phase shift

$$\text{SNR}_\theta = \frac{|\theta|}{\Delta\theta} = \frac{1}{2} \left| \frac{dS}{d\theta} \right| \frac{\Pi}{\sqrt{S(\theta)}}, \quad (4.19)$$

where we have defined

$$\Pi \equiv \left| \frac{\theta}{\theta_s} \right| \tilde{\rho} \sqrt{\eta P_{\text{abs}} A \sigma_0}. \quad (4.20)$$

The factor Π is determined by the properties of the atomic cloud and the light-atom interaction. It is independent of a chosen phase shift analyzing method and, as we will show later, it corresponds to the maximum achievable SNR_θ in each of the four analyzed dispersive imaging techniques.

At first glance, increasing the interaction cross-section σ_0 or the imaging system efficiency η is always beneficial. However, an increase in the physical pixel area A (e.g. via CCD binning before readout) improves SNR_θ at the cost of reduced image resolution. In a natural fashion, the SNR_θ is proportional to the atomic density $\tilde{\rho}$.

The SNR_θ square root dependence on P_{abs} quantifies the trade-off between the signal and destructiveness [11]. Contrary to commonly accepted intuition that arbitrary degrees of non-destructiveness can be achieved by sufficient detuning in dispersive measurements, the above equations illustrate that in the off-resonant regime, the signal-to-noise ratio does not depend directly on the detuning, but rather on the destructiveness P_{abs} , which is a function of both the detuning and imaging light intensity.

The phase shift ratio $|\theta/\theta_s|$ as a function of detuning is non-trivial only for vector imaging, and can be found from Hamiltonians (4.1) and (4.2) to be

$$\frac{\theta_F}{\theta_s} = \frac{3\langle f_z \rangle}{2} \left[\sum_{f'} \frac{\alpha_{f,f'}^{(1)}}{\Delta_{f,f'}} \right] \left[\sum_{f'} \frac{\alpha_{f,f'}^{(0)}}{\Delta_{f,f'}} \right]^{-1}. \quad (4.21)$$

In table 4.1, we present the far-detuned limit of this ratio for the D transitions in hydrogen-like atoms with nuclear spin $i = 3/2$ such as ^{87}Rb , ^{39}K , ^{23}Na , ^7Li , and those with $i = 7/2$ such as ^{133}Cs . We note that, in these cases, the ratio is always smaller than or equal to one resulting in a reduced SNR_θ for vector compared to

scalar imaging methods. In our system, at a detuning $\Delta = 2\pi \times 1\text{GHz}$, we expect $|\theta_F/\theta_s| = 0.59$. Here, the additional information one obtains in imaging with the vector part of the atomic polarizability comes at the expense of a reduced SNR_θ compared to the scalar phase shift imaging.

Table 4.1: Far detuned vector to scalar phase shift ratio $|\theta_F/\theta_s|$ for hydrogen like atoms with nuclear spin i .

$i = 3/2$			$i = 7/2$		
f	D ₁ line	D ₂ line	f	D ₁ line	D ₂ line
1	1/2	1/4	3	3/4	3/8
2	1	1/2	4	1	1/2

Comparison of dispersive imaging methods

To make a fair comparison of different imaging techniques, we first neglect experimental imperfections such as a non-ideal beam block or phase plate placement in DFSI and PCI respectively, and also omit non-zero cube suppression in DFFI.

Provided the measurement destructiveness P_{abs} is low, the probe light transmission coefficient through the cloud can be set to one, and the detected light intensity for the two scalar imaging techniques [7] reduces to

$$I^{(\text{DFSI})} = I_0 [2 - 2 \cos(\theta_s)], \quad (4.22)$$

$$I^{(\text{PCI})} = I_0 [3 - \sqrt{8} \cos(\theta_s - \pi/4)]. \quad (4.23)$$

In the DPFI method the probe light is polarized at 45° with respect to the PBS axis. The horizontally and vertically polarized ports are imaged separately on the camera according to

$$I_H^{(\text{DPFI})} = I_0 [1 + \sin(2\theta_F)] / 2, \quad (4.24)$$

$$I_V^{(\text{DPFI})} = I_0 [1 - \sin(2\theta_F)] / 2. \quad (4.25)$$

The signal is obtained from the difference of the two images, however the variance in such a picture is proportional to the sum of the two variances, making the signal error independent of the rotation angle $\Delta S^{(\text{DPFI})} = 1/\sqrt{\eta N_{\text{ph},0}}$.

Table 4.2 summarizes the signal function properties and the resulting SNR_θ for the discussed techniques, normalized with respect to the factor Π . Fig. 4.2(a) displays the SNR_θ/Π variation with the respective phase shift θ . In the small phase shift limit $\theta \ll 1$ all four techniques offer a signal to noise ratio $\text{SNR}_\theta \approx \Pi$. At high angles, the sensitivity of first the two Faraday imaging techniques and then the two scalar ones decreases to zero. This is caused by extremal points in the

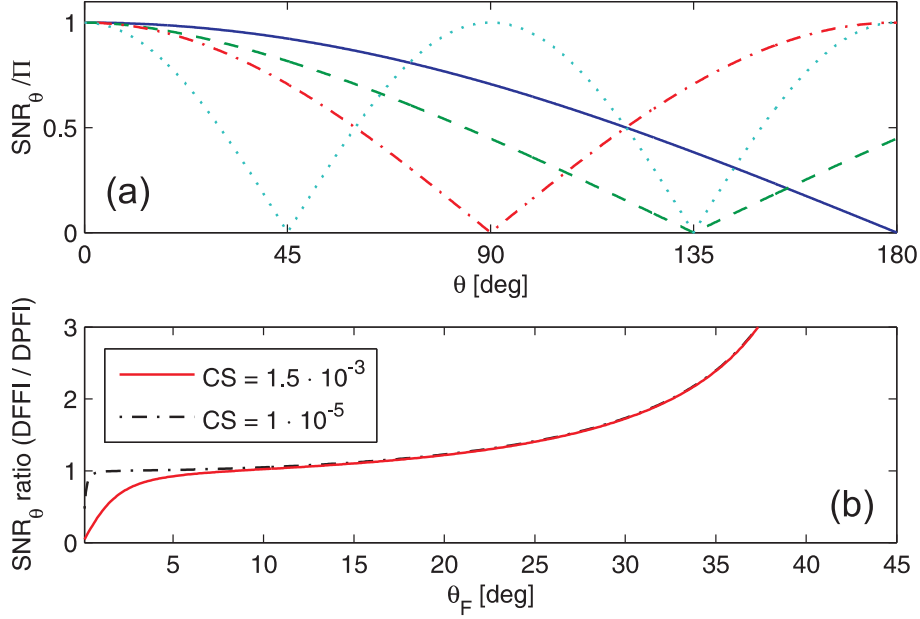


Figure 4.2: Signal to noise ratio in the measured phase shift. (a) SNR_θ / Π for common dispersive imaging techniques (DFSI blue solid; PCI green dashed; DFFI red dot-dashed; DPFI cyan dotted) as a function of the respective phase shift. (b) Relative SNR_θ ratio for DFFI and DPFI vs. Faraday rotation angle. Non-zero cube suppression CS was taken into account.

signal function $S(\theta)$, when the light noise is amplified by the diverging derivative $|d\theta/dS|$.

Although in dark field imaging, the signal increases only quadratically with the phase shift θ , noise in the picture originates only from the signal light. On the other hand, in PCI or DPFI there is a finite light intensity, and hence shot noise detected, even when no phase shift occurs. This feature, together with the relative suppression of noise in the error propagation formula, equalizes the sensitivity of the above methods for small phase shifts θ .

Fig. 4.2(b) shows a comparison of the two Faraday imaging techniques in a more realistic model, where the cube suppression is not neglected. We present the result for our experimental value $\text{CS} = 0.0015$ as well as for a high quality Glan-Thompson polarizer with $\text{CS} = 10^{-5}$. Although for small angles $\theta_F \lesssim \sqrt{\text{CS}}$ the DFFI technique offers lower SNR_θ , for higher angles it is superior to the dual port imaging, for which the noise diverges at $\theta_F = 45^\circ$; a typical peak angle in our experiments. As seen from Fig. 4.2 (a), DFFI only reaches zero sensitivity at twice this angle. To obtain the same sensitivity in the high angle regime, the detuning in the DPFI method has to be chosen about twice that of DFFI. The absolute sensitivity SNR_θ / Π of our DFFI system peaks at $\theta_F \approx 11^\circ$, when it reaches 96% of the theoretical maximum.

Table 4.2: Signal properties of dispersive imaging techniques.

technique	$S(\theta)$	$dS/d\theta$	SNR_θ/Π
DFSI	$2 - 2 \cos \theta_s$	$2 \sin \theta_s$	$ \cos(\theta_s/2) $
PCI	$3 - \sqrt{8} \cos(\theta_s \pm \pi/4)$	$\sqrt{8} \sin(\theta_s \pm \pi/4)$	$\frac{ \sqrt{2} \sin(\theta_s \pm \pi/4) }{\sqrt{3 - \sqrt{8} \cos(\theta_s \pm \pi/4)}}$
DFFI	$\sin^2 \theta_F$	$\sin(2\theta_F)$	$ \cos(\theta_F) $
DPMI	$\sin(2\theta_F)$	$2 \cos(2\theta_F)$	$ \cos(2\theta_F) $

4.4 Faraday laser system

The off-resonant Faraday light is derived from a home built, external cavity diode laser in Littrow configuration, which is locked to a master laser via a tunable offset lock [60]. The master laser is locked to a saturation spectroscopy signal on the $f = 2$ to $f' = 1$ and $f = 2$ to $f' = 3$ crossover, which makes it 212MHz red detuned from the $f = 2$ to $f' = 3$ transition. The electronic level structure can be found in appendix A.

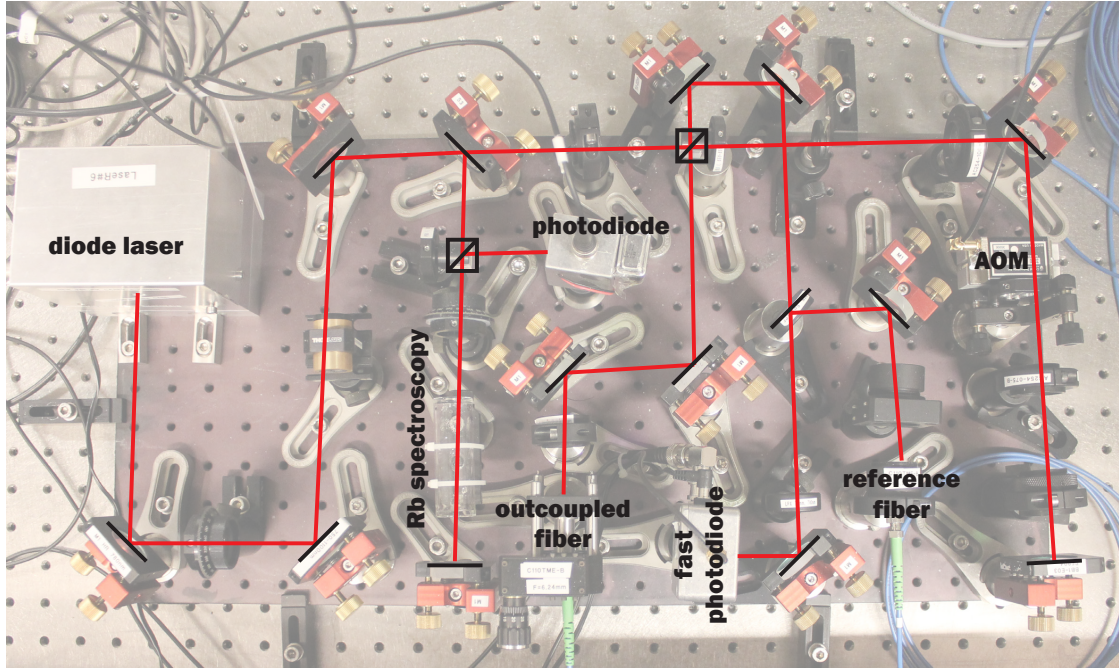


Figure 4.3: Photo and schematics of the beam path for the Faraday laser system.

A weak master beam from the main laser system is fiber-coupled and delivered to the Faraday laser ‘bread board’, where it is mode-matched with a fraction of the Faraday light on a 50/50 beam splitter. The beat-note of the two lasers is recorded by a fast photo-detector and mixed with a signal from a voltage controlled oscillator (VCO), to obtain a side band at a difference of the two frequencies. The mixer is

followed by a low pass filter and an amplifier. Next, the signal is split, one part of it is delayed by an external cable and mixed again with the non-delayed signal. The DC component of the result is a measure of a relative phase shift on the delay line. The spacing and position of nodes during a laser frequency sweep depends on the delay cable length and the VCO frequency. Using a feedback circuit with proportional, differential and integral gain (PID), the laser can be locked to a chosen node and tuned in lock by a VCO frequency adjustment.

Since the $f = 2 \rightarrow f' = 3$ transition has the highest oscillator strength (see Eq. (4.9)), we use $\Delta_{2,3} \equiv \Delta$ as a measure of the laser detuning. This system allows us to lock the laser in the range $\Delta = (-1.5, 1.8)$ GHz and to adjust the detuning dynamically in a single run within a range of 0.7 GHz. To monitor the detuning, the system is also equipped with an auxiliary saturation spectroscopy.

The Faraday power is controlled by a double pass acousto-optical modulator (AOM), which shifts the laser frequency up by two times 200 MHz. The imaging light pulses are typically of $1 \mu\text{s}$ duration. A pair of concave lenses is used to focus the beam through the AOM. An intermediate fiber is used to guide the light into the imaging section of the main laser system, where it is overlapped with the beam path for the z -axis absorption imaging and coupled into an existing imaging fiber. The imaging fiber delivers the light to the experimental table.

On the experimental table, the light polarization is cleaned by two PBS cubes followed by a half-wave plate (HWP) for the incident polarization adjustment. The light is injected into the science chamber through a hole in the Ioffe coil and propagates along the symmetry axis (z -axis in Fig. 4.1) of the cigar-shaped trap, corresponding to the magnetic field direction. The imaging beam waist at the cloud was $2\sigma = 2.29$ mm. After the chamber, the light impinges on a $2''$ PBS, where the Faraday rotated light is transmitted to the imaging camera and the non-rotated part is reflected and focused onto a photo-detector to monitor the optical power.

4.5 Atom number and temperature calibration

We first investigate the Faraday coefficient c_F as a function of the laser detuning. Fig. 4.4 (a) shows this dependence, where $c_F = \theta^{\text{sum}}/N_{\text{abs}}$ is obtained experimentally by summing θ_F (obtained from Eq. (4.12)) over all CCD pixels and N_{abs} is the atom number obtained from the absorption image. We focus on the characterization of the blue detuned side, to avoid complications arising from molecular resonances [17]. In each experimental sequence, we prepared a thermal cloud at $3 \mu\text{K}$ and took 35 Faraday images while sweeping the laser detuning over 700 MHz. Each pulse had a rectangular amplitude envelope with duration $1 \mu\text{s}$, peak power $160 \mu\text{W}$, and the pulse period was 4.7 ms.

The data agrees well with the theoretical value up to an overall scaling factor of 0.64. We ascribe this discrepancy to the spatial inhomogeneity in the magnetic potential and systematic calibration effects [61]. Nonetheless, the agreement is

good in light of previous work [16, 17] and justifies neglecting phase shift from the tensor atomic polarizability, which would induce detuning dependent corrections.

The destructiveness of DFFI was measured at four different detunings by exposing the cloud to Faraday light for various durations and subsequently measuring the resulting temperature in absorption images. To obtain the scattering rate from the cloud temperature, we assume that each scattering event transfers twice the photon recoil energy and the heat capacity of an atom is $\frac{3}{2}k_B$. The measured scattering rate shown in Fig. 4.4 (a) is consistent with theory up to 50%. Fig. 4.4 (a) also illustrates that the scattering rate decays as $1/\Delta^2$ whereas the Faraday coefficient falls off as $1/\Delta$.

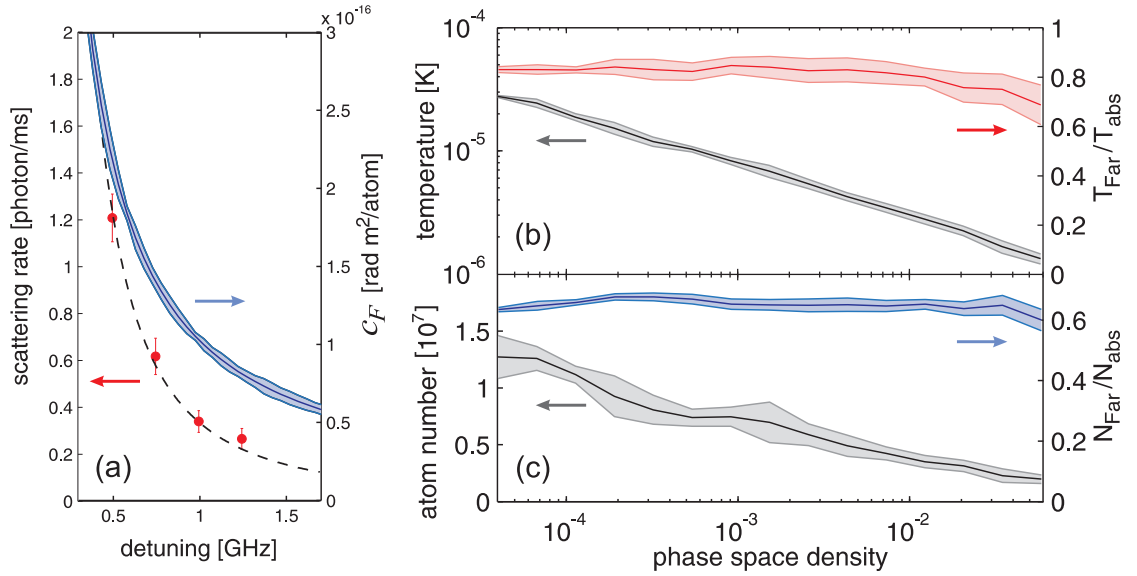


Figure 4.4: Characterization of DFFI. (a) Faraday coefficient c_F and photon scattering rate as a function of the detuning. (b), (c) Temperature and atom number obtained from DFFI compared to results from absorption imaging. Arrows in the figures indicate the appropriate axes.

To investigate the measurement accuracy, we employ DFFI at different times in the evaporation sequence, sampling an atom number range from $1.5 \cdot 10^7$ to $1.6 \cdot 10^6$ and a temperature range from $30 \mu\text{K}$ to $1 \mu\text{K}$. The upper and lower limits of this range are set by the EMCCD size and the magnification of the detection system. In each experimental sequence, 20 Faraday images are taken, from which the first six contain atoms and an average of the rest provides the intensity reference $I(\theta = 0)$. The pulse parameters correspond to those in Fig. 4.4 (a) at detuning $+750 \text{ MHz}$, leading to an absorption probability per DFFI pulse of $6 \cdot 10^{-4}$.

To verify the accuracy of these measurements, we have taken a calibrated absorption image [62] at the end of each experimental sequence. This provides an independent measurement of the number of atoms and the temperature of the

cloud. The measured temperatures and atom numbers are shown in Fig. 4.4 (b) and (c) as a function of phase space density. In both cases, DFFI allows for precise measurements over the entire parameter range, despite the fact that atom number and temperature are changed dramatically. Fig. 4.4 (b) and (c) show that the proportionality factor between the two methods is essentially constant: it is 0.82(9) for the temperature, and, consistent with the results in Fig. 4.4 (a), the atom number proportionality factor is 0.65(3). This result confirms that DFFI provides precise non-destructive measurements and good accuracy can be obtained by appropriate scaling of the results.

4.6 Monitoring system dynamics

Vector field magnetometry

Due to the magnetic field dependence of the Faraday effect, DFFI also allows for new avenues in magnetometry. Vapor cell optical magnetometers [63] based on the Faraday effect have been extremely successful. They reach sensitivities competitive with state-of-the-art SQUID magnetometers (superconducting quantum interference device) and allow for both spatial resolution [64] and vector field magnetometry [65]. However, in this method, due to atomic motion, the spatial resolution is typically limited to millimetre length scales. For this reason, magnetometry based on ultracold atoms holds promise for orders of magnitude higher precision due to the reduced thermal motion. Spatially resolved magnetometry has been realized in, e.g., dark optical tweezers [66] and Bose-Einstein condensates [67, 5]. Furthermore, vector magnetometers were recently realized [68] by combining Faraday rotation in one iteration with a measurement using the tensor part on another sample and in ref. [69] using spatially resolved absorption imaging of a precessing collective spin after variable evolution times. To date, however, all realizations have been limited in interrogation time and to resolutions of the order of tens of microns due to residual motion along a weakly confining trap axis.

In this work, we take an important conceptual step towards higher spatial resolution by realizing a single shot vector magnetometer based on ultracold atoms in an optical lattice. The method is an adaptation of a standard strategy of vapour cell magnetometers [65] relying on time-dependent control of additional magnetic bias fields to determine the magnetic field components. In principle, our approach allows for spatially resolved magnetometry down to the scale of a single lattice site ($\approx 0.5 \mu\text{m}$).

To realize this lattice magnetometer, the atomic cloud is transferred into a 1D vertical lattice at a wavelength of 914 nm, whereupon we sweep the magnitude of an additional magnetic field applied along the z -axis. During this sweep, 50 DFFI images are taken to obtain the integrated Faraday signal at each applied magnetic field B_z as shown in Fig. 4.5 for two values of the transverse magnetic field. The

data was normalized and fitted with $e^{-\kappa t}|B_z - B_{z_0}|/|\mathbf{B}|$, where the modulus is taken because our method is not sensitive to the sign of the Faraday rotation. The fit yields the offset field in the z -direction B_{z_0} and the magnitude of the transverse field $|\mathbf{B}_r|$. The exponential factor in the fit function accounts for atom loss during the sweep.

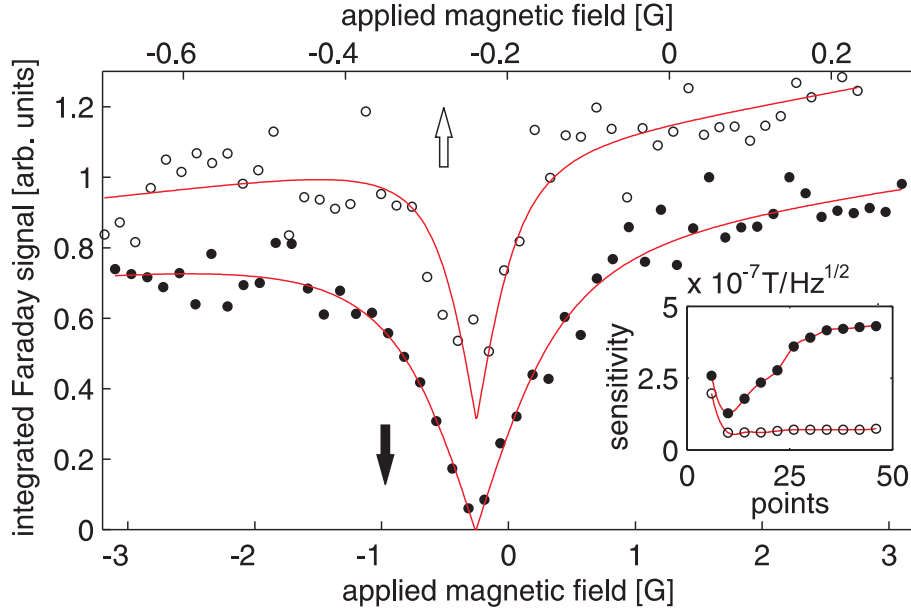


Figure 4.5: Single-run magnetometry in an optical lattice. DFFI signal as a function of the applied magnetic field along the z -axis. Open circles: Magnetic field sweep over 0.93 G at $|\mathbf{B}_r| = 0.053$ G. Full dots: Magnetic field sweep over 6.2 G at $|\mathbf{B}_r| = 1.03$ G. The inset shows the sensitivity of the offset field extraction for the two realizations as a function of number of data included points (centered around the signal minimum). The sensitivity is estimated as the error of the fit times the square root of time taken to record the included data points.

In a first approach, to quantify the sensitivity of such a time dependent vector magnetometer, the precision of extracting B_{z_0} was evaluated as a function of the number of included data points (Fig. 4.5 inset) yielding best values of $0.6 \cdot 10^{-7} \text{ T}/\sqrt{\text{Hz}}$ for the smaller sweep. The sweeps yield an offset field $B_{z_0} = -0.252(13)$ G, which is within the uncertainty in agreement with our microwave calibration technique. This demonstration shows new avenues for magnetometry with DFFI, which could be better exploited with an optimized magnetometry sequence.

Spatially resolved cloud dynamics

DFFI allows for the non-destructive investigation of spatial dynamics. We demonstrate this by monitoring the position of the atomic cloud as it oscillates in a harmonic potential. Since a single cloud can be probed repeatedly, one can map its trajectory in a single experimental run. This has previously been realized without spatial resolution to monitor breathing [70] and center-of-mass oscillations [71]; however, this approach fails for more complicated trajectories, e.g., when the position of the trapping potential is dynamically varied during the oscillation.

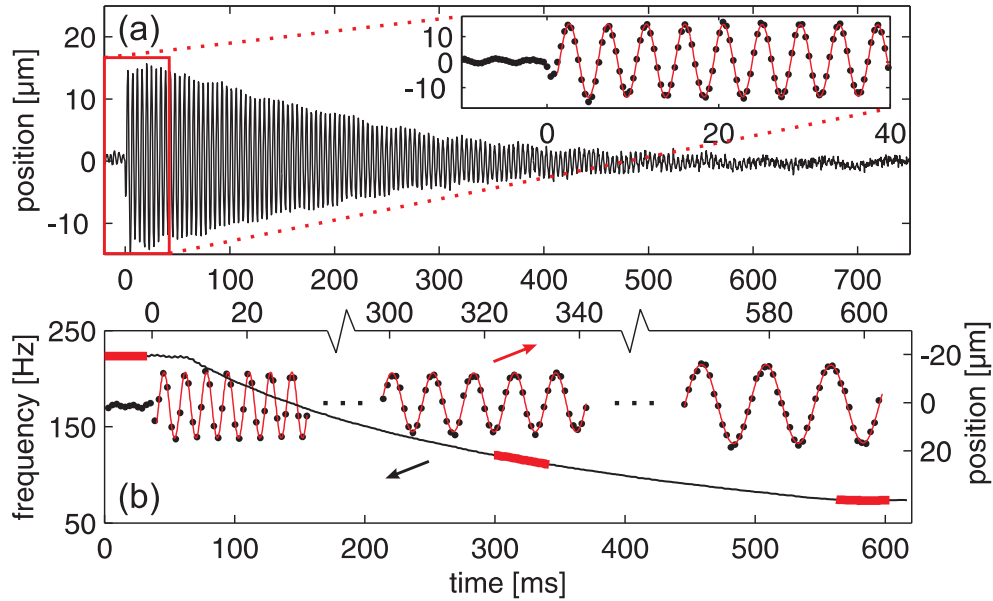


Figure 4.6: Monitoring of spatial dynamics. (a) Non-destructive measurement of the cloud position during a damped oscillation. (b) Non-destructive measurement of the cloud position during a decompression of the magnetic trap. The cloud position and oscillation frequency are shown within three time intervals during the decompression.

Fig. 4.6 (a) shows the position of the cloud recorded in a single experiment by acquiring a total of 2000 images at intervals of 0.402 ms. Initially, a cloud of about 10^6 atoms at $1 \mu\text{K}$ was created in a magnetic trap and the imaging was started. Shortly afterwards ($t = 0$), the magnetic trap was turned off for a duration of $70 \mu\text{s}$, which initiated a strong vertical oscillation.

The initial part of the oscillation was fitted to obtain the trapping frequency of $222.44(6)$ Hz as shown in the inset of Fig. 4.6 (a). The residual anharmonicity of the trap makes the system ergodic and slowly transfers the collective motion of the atoms into thermal energy. This results in a decrease of the oscillation amplitude and heating of the cloud, which can be extracted from the DFFI pictures simultaneously.

The continuous probing of the spatial dynamics enables us to monitor dynamic changes of the system in a single sequence. To demonstrate this, we have observed an oscillating cloud during a decompression of the trap. Again, we prepared a cold cloud in a magnetic trap and started the acquisition of 750 images at intervals of 0.89 ms. The oscillations were initiated at time $t = 0$ and after a hold time of 60 ms we began to decrease the current of the magnetic trap and simultaneously increase the bias field. The resulting decrease in the trapping frequency caused the cloud to sag due to gravity while it continued to oscillate.

The final displacement of the equilibrium position was $65 \mu\text{m}$: about four times the cloud size. By subtracting the shift of the equilibrium we obtained the chirped oscillations; these oscillations were fitted within short time intervals to extract the time dependent trapping frequency, as shown in Fig. 4.6 (b). This example highlights the advantages of spatially resolved non-destructive probing, since the temperature and the in-trap equilibrium position cannot be extracted from non-spatially resolved dispersive methods [70, 71].

To investigate the option of providing feedback to the in-trap cloud motion, we have attempted to extinguish the oscillation after few cycles. This was done by using the same trap turn-off pulse applied again after a half integer multiple of the oscillation period.

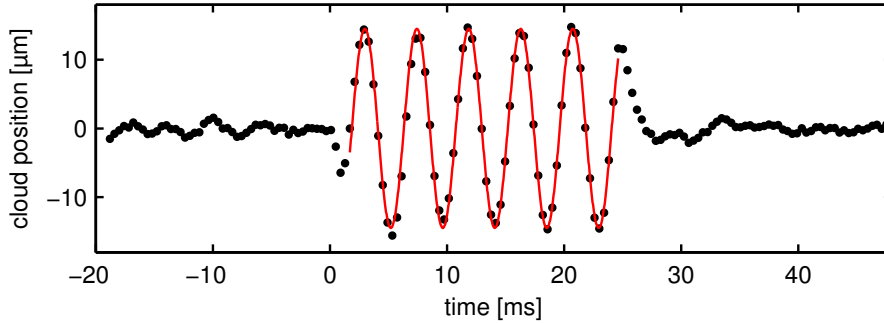


Figure 4.7: Non-destructive monitoring of controlled excitation and de-excitation of in-trap oscillations with cold thermal cloud.

Figure 4.7 shows the result of an experiment where the oscillation was stopped after 5.5 periods of oscillation. The precise delay between the two control pulses was adjusted empirically to yield the best result. Physically, the process can be visualised as follows. The first trap turn-off allows the cloud to fall briefly, which puts it out of equilibrium. Once the trap is on again, the cloud begins to oscillate. The second turn-off pulse is applied when the cloud is moving upwards. Removal of the potential, causes the cloud to slow down and captures it again once it reaches rest in the equilibrium position.

Actively stabilized preparation of atomic clouds

This chapter presents our results on high precision Faraday measurements and feedback. The method was improved to achieve a photon shot noise limited detection, which allows to resolve the stochastic character of atom number loss in an RF cut. Fast on-line evaluation of the Faraday images allows to control the applied loss with feedback and produce atomic samples with highly reduced atom number fluctuations.

Introduction

A non-destructive measurement allows to extract information about a system, without significantly disturbing its state. Such knowledge can be used to customize the ‘treatment’ of the system, making it evolve into a desired state.

Feedback can be defined as a measurement dependent action on a system. In our case, the system is an atomic cloud in a magnetic trap and the measurement is the Faraday image of the cloud. According to the thermal state of the cloud, we can divide the feedback into quasi-equilibrium and out-of-equilibrium cases: a cloud in a thermal equilibrium is fully characterized by a temperature and the number of atoms, whereas an out-of-equilibrium cloud can have a density distribution with time varying spatial moments; the mean and the variance being the first two. A quasi-equilibrium feedback acts on the temperature and/or the atom number and the feedback loop frequency has to be lower than the rethermalization rate. In contrast to that, the out-of-equilibrium feedback, such as the control of in-trap cloud oscillations, requires a fast response time, on the order of milliseconds in the magnetic trap.

As we have shown in the previous chapter, the DFFI method provides a fast and precise measurement of the atomic cloud properties. We have observed large

natural fluctuations of the atom number due to the irreproducibility of initial conditions in the evaporation sequence. We now want to measure these deviations and apply an active stabilization at a later point in the evaporative sequence. This should facilitate a stable production of ultracold thermal clouds and BECs, providing reproducible starting conditions for other experiments. Later, we want to apply feedback to the position of the cloud and eliminate the in-trap oscillations generated, e.g., by a non-adiabatic trap transformation.

5.1 Online image analysis

Real-time data processing hardware

To be able to cover both types of the feedback, we need to implement fast, real-time image evaluation. Although the traditional computer data processing does not meet these criteria, equipping the computer with a field programmable gate array (FPGA) allows one to encode an algorithm directly into an electronic hardware design featuring fast and deterministic execution. Since the information processing resources are to a large degree independent of each other, the architecture can perform several tasks in parallel, such as capture and evaluate an image, while controlling other experimental equipment in real time. To simplify the task of designing a complex hardware program, we decided to use a National Instruments FPGA (NI PCIe-7852R), which can be programmed by LabVIEW, a high level graphical programming language widely used for the control of scientific instruments.

The acquisition properties of the camera (Andor iXon DU-888) have to be set up from a computer. Nevertheless, the acquisition can be triggered by external hardware, and the captured image can be read out in parallel by the FPGA. As soon as the image exposure is complete, the individual pixels are digitized with 14 bit resolution and transferred at 10 MHz rate into the computer. A digital repeater installed on the computer line for cable extension purposes allows to split the data transfer and feed it into the FPGA via a couple of parallel TTL channels. Together with the 14 data lines, the *data clock*, *frame*, *fire* and *armed* channels are provided. The last two channels signal, respectively, that the exposure is in progress and that the camera is ready for the next exposure.

The data acquisition on the FPGA is performed in a 40 MHz loop. The pixel values are read out on a rising edge of the *data clock* provided the *frame* channel is high. Not all pixel values have to be processed: only three preselected regions of interest (ROI) are monitored. These correspond to *signal* (the area of the cloud), *reference* (an area surrounding the atoms used for light intensity scaling) and *baseline* (a masked area of the picture used for background light and electronic offset subtraction); these regions are shown in Figure 5.1. Pixel sums of the three ROIs are accumulated already during the image readout. Only the signal ROI raw image is saved into the FPGA RAM memory. The entire frame is always captured

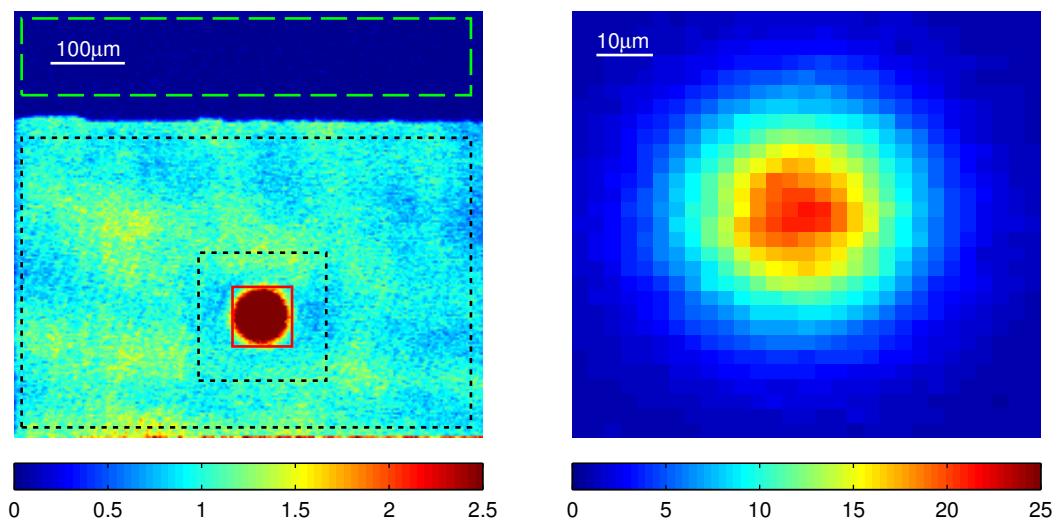


Figure 5.1: Example of rescaled Faraday image $I(\theta_F)/I(0) \propto S$. The left image shows the full 220×200 pixel frame. The right image is a zoom to the signal ROI marked with the red solid line, 29×29 pixels. The area between the two black dotted rectangles is used for estimation of the reference intensity $I(0)$ from the leaked light. The mean pixel count from the green dashed rectangle (baseline ROI) is used for electronic offset subtraction on the masked part of the CCD.

by the camera computer, allowing for post evaluation.

By default, we are using 220×200 pixel frame and we mask the upper 50 rows with a razor blade in the intermediate image plane. With this frame size, the maximal continuous imaging rate is 7ms per picture—limited by the camera readout speed.

Thermal cloud temperature and atom number

In principle, a relative measure of the atom number can be obtained very ‘easily’ by summing the Faraday angle θ_F over the signal ROI. However, this would require knowledge of the rotation angle for each pixel, which means calculating $\arcsin \sqrt{S(\theta_F) - S(0)}$. Since the dimensionless signal function $S(\theta_F)$ involves a subtraction of the baseline and scaling with the reference light intensity, the rotation angle can be evaluated only after the whole picture has been read out. The non-trivial conversion function requires a couple of clock cycles to evaluate and would have to be applied in a loop, pixel by pixel. The image evaluation would thus take an amount of time equivalent to the image readout time (typically on the order of milliseconds).

The main problem, however, lies in applying the square root to the image $S(\theta_F) - S(0)$, which contains negative values due to the noise in the light intensity. Furthermore, when an argument of a square root function approaches zero, its

derivative grows to infinity and thereby amplifies the noise significantly. The area with low mean rotation angles would thus induce most of the noise in the integrated rotation angle.

These problems can be bypassed by working directly with the signal sum

$$\Sigma_S \equiv \sum_{i,j} S_{ij}, \quad (5.1)$$

carried out over a finite area containing the cloud (the indices on S denote pixel coordinates). Here, the dominant contribution to the uncertainty comes from photon shot noise of the rotated light, which scales $\propto \sqrt{S_{ij}}$. The signal sum depends both on the atom number and temperature, and we will now investigate this dependence analytically.

Due to the equality of the two transverse trapping frequencies $\omega_\perp = \omega_x = \omega_y$, the cloud profile is expected to be radially symmetric. Assuming that the in-trap thermal cloud has a Gaussian density distribution, the atom number proportionality reads

$$N \propto \Sigma_\theta \equiv \int r d\phi dr \theta_F(r) = 2\pi\theta_{\max} \int_0^\infty r dr \exp\left(-\frac{r^2}{2\sigma^2}\right) = 2\pi\sigma^2\theta_{\max}, \quad (5.2)$$

where θ_{\max} is the peak rotation angle and the Gaussian width σ is related to the temperature of the cloud through the equipartition theorem

$$\frac{1}{2}k_B T = \frac{1}{2}m\omega_\perp^2\sigma^2. \quad (5.3)$$

The two above equations imply a useful relation for the peak rotation angle

$$\theta_{\max} \propto \frac{N}{T}. \quad (5.4)$$

Up to an offset, the raw image sum is proportional to

$$\Sigma_S = \int r d\phi dr \sin^2 \theta_F(r) = 2\pi \int_0^\infty r dr \sin^2 \left[\theta_{\max} \exp\left(-\frac{r^2}{2\sigma^2}\right) \right]. \quad (5.5)$$

Making the substitution $\theta = \theta_{\max} \exp\left(-\frac{r^2}{2\sigma^2}\right)$ and using the result (5.2), we can express the above as

$$\Sigma_S = -2\pi\sigma^2 \int_{\theta_{\max}}^0 \frac{d\theta \sin^2 \theta}{\theta} = \Sigma_\theta \beta(\theta_{\max}), \quad (5.6)$$

where we have defined

$$\beta(\theta) \equiv \frac{1}{\theta} \int_0^\theta \frac{d\theta' \sin^2 \theta'}{\theta'}. \quad (5.7)$$

This integral does not have an analytic solution, because it requires knowledge of the so called *cosine integral function*. Since the DFFI method is limited by $\theta_{\max} < \pi/2$, a Taylor expansion of the sinus function provides a high precision in a couple of terms, and the integration can be carried out explicitly, yielding

$$\beta(\theta) = \frac{\theta}{2} - \frac{\theta^3}{12} + \frac{\theta^5}{135} - \frac{\theta^7}{2520} + \dots \quad (5.8)$$

This is a simple polynomial function, which can be evaluated quickly on the FPGA. The relative atom number and temperature measures are then given by

$$N \propto \Sigma_{\theta} = \frac{\Sigma_S}{\beta(\theta_{\max})}, \quad (5.9)$$

$$T \propto 2\pi\sigma^2 = \frac{\Sigma_{\theta}}{\theta_{\max}} = \frac{\Sigma_S}{\theta_{\max}\beta(\theta_{\max})}. \quad (5.10)$$

A cloud in a thermal equilibrium is fully specified by N and T , meaning that the signal sum is also a function of these two quantities $\Sigma_S \equiv \Sigma_S(N, T)$. For small rotation angles, we can approximate $\beta(\theta) \approx \theta/2$ and from Eqs. (5.4) and (5.6) write

$$\Sigma_S \propto N\theta_{\max} \propto \frac{N^2}{T}. \quad (5.11)$$

Due to the second power dependence on N , the signal sum is about factor of two more sensitive to relative deviations in the atom number. This can be seen more explicitly by expanding the relative error in signal sum $E_S \equiv \Delta\Sigma_S/\langle\Sigma_S\rangle$ as a function of the relative deviations in atom number $E_N \equiv \Delta N/\langle N\rangle$ and temperature $E_T \equiv \Delta T/\langle T\rangle$

$$E_S = \frac{\frac{\partial\Sigma_S}{\partial N}\Delta N + \frac{\partial\Sigma_S}{\partial T}\Delta T}{\langle\Sigma_S\rangle} = \frac{\partial\Sigma_S}{\partial N} \frac{\langle N\rangle}{\langle\Sigma_S\rangle} E_N + \frac{\partial\Sigma_S}{\partial T} \frac{\langle T\rangle}{\langle\Sigma_S\rangle} E_T \equiv \gamma_N E_N + \gamma_T E_T, \quad (5.12)$$

where in the last equality we have defined error propagation coefficients γ_N and γ_T . Equation (5.11) implies $\gamma_N = 2$ and $\gamma_T = -1$. Later we will calibrate these two coefficients experimentally.

Finally, we outline the technicalities connected with evaluating Eqs. (5.9) and (5.10) efficiently on the FPGA. Since all arithmetic operations on the FPGA are carried out using a fixed point data type (constant absolute error), the relative error scales inversely-proportional to the magnitude of the represented number. Given the same resources, it turns out to be more precise to evaluate the factor $1/\beta$ from an analytical expression and multiply by it, rather than divide Σ_S directly with β . Expressing $1/\beta$ as an expansion $\sum_{k=-1}^{\infty} a_k\theta^k$, one can find the coefficients a_k by minimizing the relative error

$$\epsilon(\theta) = 1 - \beta \cdot (1/\beta) = 1 - \beta \sum_{k=-1}^{\infty} a_k\theta^k. \quad (5.13)$$

Substituting for β from (5.8), multiplying the two polynomials and nulling all the coefficients on the right hand side yields a set of linear equations for the expansion coefficients a_k . We obtain an expression for $1/\beta$ in the form

$$\frac{1}{\beta(\theta)} = \frac{2}{\theta} + \frac{\theta}{3} + \frac{7\theta^3}{270} + \frac{11\theta^5}{22680} + \dots \quad (5.14)$$

To achieve the required precision in our applications, it is sufficient to use only the first three terms of this expansion. The error of the truncated expansion can be distributed more evenly over the interval $\theta \in (0, \pi/2)$, by adjusting the last coefficient. Allowing a_3 to vary, we find that the standard deviation of the error (5.13) on the interval $(0, \pi/2)$ is minimized for $a_3 \approx 1/36$, when it acquires a value $2.7 \cdot 10^{-4}$. For the analytical result $a_3 = 7/270 \approx 1/38.57$ the standard deviation is $14.5 \cdot 10^{-4}$, about five times larger due to the growing standard deviation in the high angle regime.

To reduce the number of division operations, we first evaluate the temperature

$$T^{(\text{FPGA})} \equiv \frac{\Sigma_S}{\theta_{\max}\beta(\theta_{\max})} \approx \Sigma_S \left[\frac{2}{(\theta_{\max})^2} + \frac{1}{3} + \frac{(\theta_{\max})^2}{36} \right] \quad (5.15)$$

and then multiply by θ_{\max} to obtain the atom number

$$N^{(\text{FPGA})} \equiv \frac{\Sigma_S}{\beta(\theta_{\max})} = \theta_{\max} T^{(\text{FPGA})}. \quad (5.16)$$

Peak rotation angle and cloud position

It is now clear that the peak rotation angle θ_{\max} is an essential parameter for a quick temperature and atom number evaluation. It also determines the sensitivity of the imaging method as discussed in Chapter 1. The peak angle can be evaluated from

$$\theta_{\max} = \arcsin \sqrt{S_{\max}} = \frac{1}{2} \left[\arcsin(2S_{\max} - 1) + \frac{\pi}{2} \right], \quad (5.17)$$

$$S_{\max} \equiv S(\theta_{\max}) - S(0), \quad (5.18)$$

$$S(\theta_F) = \frac{I^{(\text{DFFI})}(\theta_F)}{I_0} = \frac{\text{CSI}^{(\text{DFFI})}(\theta_F)}{I_{\text{ref}}}, \quad (5.19)$$

where we have defined the peak signal S_{\max} such that it represents only the rotated light intensity. The reference light intensity I_{ref} is a mean over the reference ROI. The peak signal cannot simply be calculated as a mean of the few highest pixel values, because in the low angle regime it is often the image noise that determines the sorting. To average out the noise, the mean has to be taken over a uniform area that is still small in size compared to the cloud, in order to include only the peak angles.

To locate the peak area, that is to find the cloud's position, a non-weighted average over the coordinates of the maximum values is taken. The maximum values are found already during the picture readout. Since divisions of a fixed point binary numbers with powers of 2 require no processing (fixed point translation), we choose to take the mean over 8 maximum values yielding a cloud position resolution of 0.125px. The cloud position is then rounded to the nearest integer to locate the peak area.

The peak area was chosen to be a 3×3 square, however, to obtain the mean peak signal, the values are not weighted equally, in order to favor the central pixels when the cloud size is small. The central pixel has a weight of 4, its side-neighboring pixels are weighted with 2 and the corner ones with 1 implying that the weighted sum should be divided by 16. Using only the powers of 2 for the multiplication and division, the number of operations is reduced significantly, while the computation itself is precise and without cost.

The conversion function (5.17) cannot be evaluated directly, because the LabVIEW FPGA module does not provide an arcsin function. The function also cannot be well approximated by a single polynomial series because all its derivatives diverge at the end points of the definition interval $S_{\max} = \langle 0, 1 \rangle$. The simplest solution seems to be to use a linear interpolation between a couple of pre-calculated points. Realizing that the arcsin has odd parity, it is enough to implement the interpolation only for positive values and then correct it with a sign of the argument. In our implementation we use 32 points at 32 bit precision, distributed such that the standard deviation is minimized. This requires a higher density of points closer to the end points of the interval, because the first derivative grows quickly there. The final FPGA implementation of the function (5.17) yields a standard deviation of the relative precision of $2.5 \cdot 10^{-4}$.

5.2 Active experiment control

In the first set of experiments, our goal is to provide feedback to the RF evaporation sequence, that is to obtain a cloud with a predefined atom number and temperature free of run-to-run fluctuations.

In the first approximation, the cloud temperature is proportional to the trap depth. In the magnetic trap, this corresponds to the distance of the RF knife from the trap bottom. Since the RF frequency is controlled very precisely, the trap depth varies mainly due to drifts of the magnetic field. The drifts play a role only in the last stages of the evaporation, when their size becomes comparable to the trap depth. Consequently, the temperature is well defined by the RF level for most of the time, and therefore does not require active stabilization. Although we might come back to the temperature feedback later, at the moment we will neglect the trap bottom drifts and focus on atom number stabilization.

During the planning phase, we considered the option of inducing atom losses via

optical heating of the cloud using the Faraday beam. One must however consider that it is not very safe to operate the EMCCD camera in the presence of long, powerful heating pulses in between the exposures. Though it might be possible to use a different heating source, we decided to abandon this idea and to control directly the RF frequency instead. The RF can be set digitally, which offers better reproducibility and higher precision. Additionally, we can possibly devise more sophisticated feedback schemes by controlling both the power and frequency of the RF knife.

The triggering of the camera and the generation of the imaging pulses is also performed by the FPGA. Thus the imaging can be easily synchronized with the evaporative sequence. Controlling the RF with FPGA also offer the possibility of adjusting the end evaporation level in the individual runs, in case we later decide to correct the trap bottom fluctuations.

The two mechanical shutters involved in the Faraday detection (probing light and CCD) are still controlled by the Experimental Control System (ECS). Although the shutter control was implemented on the FPGA as well, operating the shutters with ECS turned out to be more convenient.

Online DDS programing via FPGA

In our experiment, the RF evaporation frequency is generated by a Direct Digital Synthesizer (DDS), which is programmed by the ECS via a serial port. For ECS, the entire experimental sequence must be compiled and loaded into a data buffer before an experimental run can begin. This prohibits adjustments of the sequence during the run, and therefore requires a full time control of the DDS chip by the FPGA.

We have settled for a 5 MHz serial programing rate, which is 1/5 of the maximum rate specified by the DDS manufacturer. The speed is limited by the rise time of the digital drivers used to amplify the current from the FPGA in order to drive the optocouplers at the DDS interface. The speed might be increased by using better drivers, however, for the present purpose this time scale is sufficient. Updating the DDS frequency takes 42 bits (8 bit instruction, 32 bit frequency and 2 bit update), which means that the frequency can be updated every $8.4 \mu\text{s}$. This provides enough resolution for all the evaporation sweeps (e.g., ramp 1 MHz/s can be swept with 8.4 Hz steps).

The control of the RF can be defined entirely in terms of linear ramps. For instance, a single ‘large’ frequency step can also be represented by a frequency sweep with the maximum ramping speed. In our system, the evaporation consists of 6 linear ramps, which approximate an exponential—the standard form of an evaporation ramp [72]. Each linear ramp is defined by a ramping speed and an end frequency. To maintain synchronous execution with the rest of the experiment, the FPGA initiates each ramp upon receiving a trigger from ECS. The ramping

speed is defined by a frequency step size per update period $8.4 \mu\text{s}$. When an end frequency is reached, it is held until the trigger is set high again. If the trigger is set high before a sweep is finished, the FPGA executes the next sweep immediately after the current sweep finishes. Once we calibrated the clock of the FPGA with the ECS computer (a constant relative correction of the order 10^{-6}), it turned out to be sufficient to set the trigger high at the first sweep, and let the FPGA evaporate at its own pace.

The sweep parameters (end frequencies and sweep durations) are read out from the current ECS file by a host LabVIEW program (running on the FPGA host computer). The host simply waits for the ECS file to be saved on the experiment computer and then formats the relevant data into a sequence of sweep rates and end frequencies and sends it to the FPGA. The sweeps are divided into sub-sweeps with the possibility of making a single Faraday image at the end of each sub-sweep. An imaging sequence with n successive images can be accomplished by programming a sweep (with possibly static RF frequency) consisting of n sub-sweeps and enabled imaging.

The FPGA RF control implementation has been tested with atoms on a BEC sequence, which yielded results equivalent to the original RF control.

Imaging power stabilization

The light from the Faraday laser is coupled into two fibres before it arrives at the experimental table. This makes it prone to power drifts and fluctuations. If we define destructivity as the lost fraction of atoms due to photon scattering, then 1% uncertainty on a 10% atom loss would induce a relative error $\sim 10^{-3}$ on the final atom number. Since the atom number can be measured with an order of magnitude higher precision, it is critical to actively stabilize the imaging power.

We have implemented the probe power stabilization on the FPGA as a small program that runs in parallel with the image evaluation and RF control. An amplified photo-detector (50 dB) is placed on the reflection of the polarization analysing PBS (see Fig. 4.1) and collects effectively all probing light after it has passed the science chamber. The detector is connected to an analog input on the FPGA.

The power is controlled by a double pass AOM driven by a homebuilt RF driver consisting of a voltage controlled oscillator, a voltage controlled attenuator, a fast RF switch and an RF amplifier. The pulses are made with the RF switch at a fixed duration, while the power is controlled by a feedback loop. On the FPGA, a free running ~ 10 MHz loop compares the photo-detector value with a set point and, adjusts the AOM power proportionally to the error via tunable gain. The power is stabilised only when the RF switch is on to ensure that the detector reading is valid. The response time of the AOM driver is on the order of $10 \mu\text{s}$, so we begin to regulate when the pulse has been engaged at least $16 \mu\text{s}$. Once an imaging pulse

has ended, the last power setting is applied in the beginning of the next pulse. The regulation reaches the set point in $\sim 25 \mu\text{s}$ and improves the immediate power stability from about 5% to 1%.

It is the integrated power (number of photons per pulse), that is important for a reproducible destructivity. The imaging pulses are usually $660 \mu\text{s}$ long and the relative integrated photon number stability is $3.9 \cdot 10^{-3}$ per pulse, as judged by the stability of the reference light recorded by the camera.

5.3 Measurement precision and destructivity

Single pixel noise

We want to achieve a measurement limited by the photon shot noise due to the rotated light. This requires that the technical noise of the camera such as the readout noise is suppressed. This type of noise always contributes with the same absolute magnitude irrespective of the amount of light detected on the camera. The technical noise can be effectively suppressed by distributing the same number of photons $N_{\text{ph},0}$ over multiple images, based on the following argument.

When the shot noise is the only source of noise, the overall precision in n images is preserved, because the relative precision of a single image is $\sigma_1 \propto 1/\sqrt{N_{\text{ph},0}/n}$, and the uncertainty of the mean is $\sigma_n = \sigma_1/\sqrt{n} \propto 1/\sqrt{N_{\text{ph},0}}$. Acquiring more images with consistently less photons per picture, requires a higher EM gain to make use of the dynamical range of the camera and keep the absolute number of pixel counts the same (close to maximum). Thus the relative size of the readout noise and the classical noise—noise proportional to the light intensity—stays the same, while the shot noise uncertainty σ_1 grows, and eventually dominates over the technical noise, for high enough n .

It is essential that the ROIs for baseline and reference are sufficiently large, such that the error on estimation of the reference light $I(0)$ is small compared to the error of the signal sum. The single pixel noise due to readout at 10MHz has standard deviation of ~ 5 digital counts, while the mean count level in the reference light area is ~ 150 . Average over baseline area 37×212 pixels therefore induces a relative error $(5/150)/\sqrt{37 \times 212} = 3.74 \cdot 10^{-4}$ in the estimation of the reference light intensity.

Single pixel noise in the reference light area is ~ 18 counts, while the area contains 25323 pixels producing a relative error $(18/150)/\sqrt{25323} = 7.5 \cdot 10^{-4}$. As we will show later (Eq. (5.21)), the signal sum Σ_S is measured with a relative error $\sigma_{\Sigma_S} = 3.57 \cdot 10^{-3}$ in a single picture, which is about an order of magnitude larger. This implies that the measurement is limited by the noise in the signal area.

Shot noise limited detection

To examine the scaling of precision with the amount of probing light, we performed a sequence of 50 Faraday images on a cloud with $\sim 5.5 \cdot 10^6$ atoms at a temperature $18 \mu\text{K}$. The run was repeated 10 times for 8 different probe pulse durations, with the EM-gain adjusted as to use the full dynamical range of the camera. To measure the imaging induced losses, we evaluate the atom number by fitting $\sin^2[\theta_g(x, y)]$ to the signal image $S(\theta_F) - S(0)$, where $\theta_g(x, y)$ is a Gaussian distribution for the rotation angles which depends on the atom number and temperature, see Eqs. (5.4), (5.3).

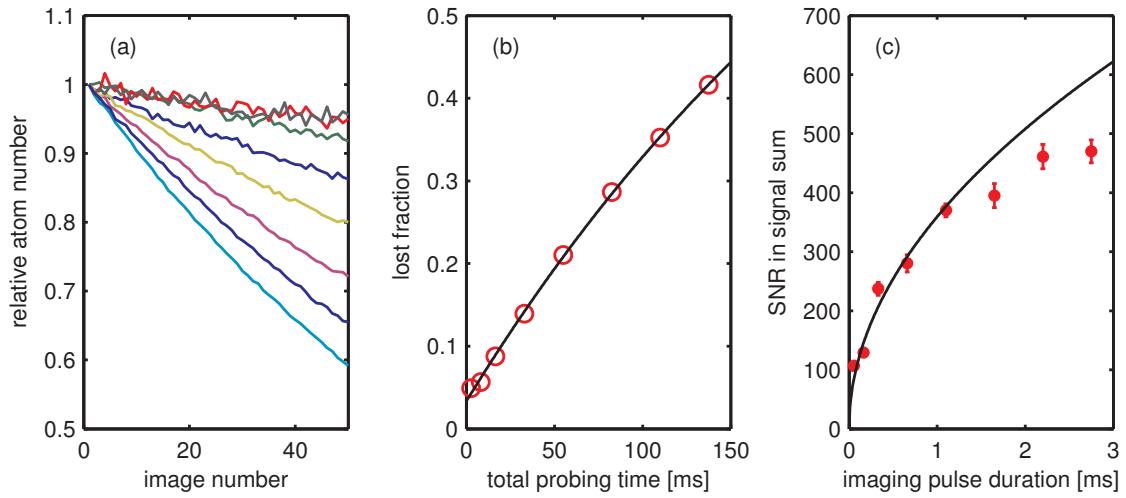


Figure 5.2: Dependence of the destructivity and measurement precision on the probe pulse duration. (a) Example traces of atom number obtained from a 2D fit to the signal images (one for each pulse duration), rescaled with the first image. (b) The lost fraction of atoms as a function of the integrated probing time. The black solid line is an exponential fit to the data. (c) The signal-to-noise ratio for signal sum evaluated on a single image as a function of the imaging pulse length. The errorbars show uncertainty of the mean based on 10 repeated experiments. The black solid line is a single parameter fit $\propto \sqrt{N_{\text{ph}}}$ to the five least destructive data points.

Example ‘traces’ of the atom number for each probe duration are shown in Figure 5.2(a). The traces were rescaled with atom number in the first picture. We see that more probing light induces higher losses, but also produces a smoother trace (higher measurement precision). The lost fraction of atoms during the 50 images is plotted as a function of the total probing time in Fig. 5.2(b). In the absence of imaging, the in-trap decay is 3.3% due to residual rethermalisation of the cloud.

To obtain the measurement precision, traces in the *signal sum* were fitted with

an exponential function individually for each run. The fits were subtracted from the data giving a deviation $\Delta\Sigma_{Sj}$ for each image j . First, we want to obtain the precision of individual images, therefore we need to evaluate correlation in pairs of successive measurements (taken on approximately the same cloud). The Allan deviation (two sample deviation) in the signal sum is

$$\sigma_{\Sigma_S} \equiv \sqrt{\frac{1}{2(M-1)} \sum_{j=1}^{M-1} (\Delta\Sigma_{Sj+1} - \Delta\Sigma_{Sj})^2}, \quad (5.20)$$

where M is the number of images.

The resulting signal-to-noise ratio in the signal sum $\text{SNR}_{\Sigma_S} = \langle \Sigma_{Sj} \rangle / \sigma_{\Sigma_S}$ is plotted in Figure 5.2(c) as a function of the probe pulse duration. We see that initially SNR_S rises with a square root dependence on the number of photons, in accordance with the scaling of the light shot noise. A single parameter square root fit to the first five data points was included as a guide for eyes. As the amount of light per picture is increased, and the consequently the EM gain is reduced, the detection becomes influenced by other sources of noise, such as the CCD readout, which hinders the growth of the SNR.

Per default, we use 0.66 ms pulse duration, which appears to be well in the shot noise limited regime, and gives relative uncertainty of the signal sum per single image

$$\sigma'_{\Sigma_S} = \frac{1}{\text{SNR}_{\Sigma_S}} = (3.57 \pm 0.18) \cdot 10^{-3}. \quad (5.21)$$

Light induced atom loss

The observed loss of atoms due to imaging is caused by spontaneous photon scattering. Two main processes might be involved: recoil heating inducing loss due to finite trap depth, and decay into untrapped states. To determine the magnitude of these contributions, we first need to estimate the number of scattered photons per atom.

Since the bias magnetic field is oriented along the probing direction, the linearly polarized light is a superposition of σ_+ and σ_- circular polarizations. Scattering photons on the σ_+ transition does not lead to a state change, since by selection rules, the atoms must decay back into $|F = 2, m_F = 2\rangle$. The scattering rate on this cycling transition may be calculated as

$$R_{\text{scat},+} = \frac{\Gamma}{2} \frac{I_+/I_{\text{sat}}}{1 + 4(\Delta_{2,3}/\Gamma)^2 + I_+/I_{\text{sat}}}, \quad (5.22)$$

where $\Gamma = 2\pi \times 6.07$ MHz is the natural line width, $I_{\text{sat}} = 1.669$ mW/cm² is the saturation intensity and $\Delta_{2,3} = 2\pi \times 1200$ MHz is the detuning of the light from the

This result is very close to the observed loss ($\sim 11\%$), which leads us to conclude that the main destructive effect of the imaging is the spontaneous scattering into untrapped states.

Uncertainty in a stochastic loss process

The atom loss due to spontaneous scattering is an example of a single body stochastic loss process, where the loss event for each atom occurs only with a certain probability and independently of other atoms. Such a random process applied to a sample with an exactly known number of particles generates uncertainty in the number of ‘survived’ particles. We will now construct a simple model for the stochastically induced uncertainty.

Let us denote the survival probability p and the initial number of particles N_0 . The probability that exactly N atoms will survive is given by the binomial distribution

$$P(N) = \binom{N_0}{N} p^N (1-p)^{N_0-N}, \quad (5.28)$$

because there is $\binom{N_0}{N}$ ways of randomly picking N atoms out of N_0 , and once those atoms survive with probability p^N , the other $N_0 - N$ atoms will be lost with probability $(1-p)^{N_0-N}$.

The mean and variance of the binomial distribution are

$$\langle N \rangle = N_0 p \quad (5.29)$$

$$\sigma_N^2 = N_0 p (1-p), \quad (5.30)$$

which implies a relative atom number uncertainty

$$\sigma'_N \equiv \frac{\sigma_N}{\langle N \rangle} = \sqrt{\frac{1-p}{\langle N \rangle}} = \sqrt{\frac{d}{\langle N \rangle}}, \quad (5.31)$$

where in the last equality we have introduced destructivity $d \equiv 1-p$. For a vanishing survival probability $p \ll 1$, the stochastic uncertainty approaches $1/\sqrt{\langle N \rangle}$, which is sometimes called the ‘atom shot noise’ limit.

Multi-image detection

For the chosen imaging conditions, the single image induced loss is $d = 2.2 \cdot 10^{-3}$, which for $\langle N \rangle \approx 5.5 \cdot 10^6$ implies a relative uncertainty $\sigma'_N = 2 \cdot 10^{-5}$. This value is about two orders of magnitude smaller than the single image precision (5.21), however, when averaging over a series of n images, the measurement uncertainty decreases proportionally to $1/\sqrt{n}$ while the stochastic noise grows as \sqrt{n} . Therefore, the two errors become comparable for $n \sim 100$.

To quantify this trade-off, we need to consider the fact that losses occur continuously throughout the imaging sequence, and therefore each image is separated by a different loss from the final atom number. We will now try to calculate more precisely the contribution of stochastic noise to the measurement precision in sequence of images. To isolate the stochastic noise contribution, assume for a moment that the individual images are infinitely precise. Provided the initial atom number is N_0 , the mean atom number measured in the k -th image is

$$\langle N_k \rangle = N_0 p^k = N_0 (1 - d)^k. \quad (5.32)$$

For a given run, we can define a relative atom number error in the k -th image

$$E_k = \frac{N_k}{\langle N_k \rangle} - 1. \quad (5.33)$$

By definition $E_0 = 0$, and in the absence of stochastic noise also $E_k = 0$ for all k . When the noise is present the error evolves as

$$E_{k+1} = E_k + \Delta E_{k+1} = \sum_{i=1}^{k+1} \Delta E_i, \quad (5.34)$$

where ΔE_k are normally distributed (for large N_0) random variables with standard deviation

$$\text{Std}(\Delta E_k) = \sqrt{\frac{d}{\langle N_k \rangle}}. \quad (5.35)$$

The simplest measure of the initial atom number N_0 (or the initial error E_0) is the mean atom number error over all images

$$\bar{E} = \frac{1}{n} \sum_{i=1}^n E_i = \frac{1}{n} \sum_{i=1}^n \sum_{j=1}^i \Delta E_j. \quad (5.36)$$

The order of the two summations can be swapped by realizing that $j \leq n$ and $i \geq j$, and the summation over i can be performed

$$\bar{E} = \sum_{j=1}^n \Delta E_j \sum_{i=j}^n \frac{1}{n} = \sum_{j=1}^n \Delta E_j (n + 1 - j)/n. \quad (5.37)$$

To obtain the measurement uncertainty of the initial atom number, we find the variance of \bar{E} with respect to the initial error E_0 .

$$\begin{aligned} \text{Var}(\bar{E} - E_0) &= \text{Var}(\bar{E}) = \sum_{j=1}^n \left(\frac{n + 1 - j}{n} \right)^2 \text{Var}(\Delta E_j) \\ &= \sum_{j=1}^n \frac{d}{\langle N_j \rangle} \left(\frac{n + 1 - j}{n} \right)^2. \end{aligned} \quad (5.38)$$

Using Eq. (5.32), we can approximate to a linear order in $d \ll 1$

$$\frac{1}{\langle N_j \rangle} = \frac{(1-d)^{-j}}{N_0} \approx \frac{1+jd}{N_0}, \quad (5.39)$$

and making the substitution $k = n + 1 - j$ we can write Eq. (5.38) as

$$\begin{aligned} \text{Var} \bar{E} &= \frac{d}{N_0 n^2} \sum_{k=1}^n [1 + d(n+1-k)] k^2 \\ &= \frac{d}{N_0 n^2} \left\{ [1 + d(n+1)] \sum_{k=1}^n k^2 - d \sum_{k=1}^n k^3 \right\}. \end{aligned} \quad (5.40)$$

The two sums are found to be

$$\sum_{k=1}^n k^2 = \frac{n(n+1)(2n+1)}{6}, \quad (5.41)$$

$$\sum_{k=1}^n k^3 = \left(\frac{n(n+1)}{2} \right)^2, \quad (5.42)$$

which gives the final result

$$\text{Var} \bar{E} = \frac{d(n+1)^2}{6N_0 n} \left(\frac{2n+1}{n+1} + \frac{d(n+2)}{2} \right). \quad (5.43)$$

For $n \gg 1$ and the combined destructivity $D \equiv dn$, this expression becomes

$$\text{Var} \bar{E} = \frac{D(1+D/4)}{3N_0}. \quad (5.44)$$

Identifying $N_0/(1+D/4) \approx \langle N_{n/4} \rangle$, we obtain the initial atom number measurement uncertainty

$$\text{Std}(\bar{E} - E_0) \approx \sqrt{\frac{D/3}{\langle N_{n/4} \rangle}}. \quad (5.45)$$

In a similar fashion we can obtain uncertainty of the final atom number measurement. We start by evaluating the variance

$$\text{Var}(\bar{E} - E_n) = \text{Var} \left[\sum_{j=1}^n \left(\frac{n+1-j}{n} - 1 \right) \Delta E_j \right] \quad (5.46)$$

$$= \sum_{j=1}^n \frac{d}{\langle N_j \rangle} \left(\frac{j-1}{n} \right)^2 \quad (5.47)$$

$$\approx \frac{d}{N_0 n^2} \sum_{k=1}^{n-1} k^2 [1 + (k+1)d], \quad (5.48)$$

where we have used Eqs. (5.34), (5.37), (5.35), (5.39) and made the substitution $k = j - 1$. Employing further Eqs. (5.41), (5.42) and neglecting d compared to one, we arrive at

$$\text{Var}(\bar{E} - E_n) = \frac{d(n-1)}{N_0} \left[\frac{2n-1}{6n} + \frac{d(n-1)}{4} \right]. \quad (5.49)$$

In the large n limit we obtain

$$\text{Var}(\bar{E} - E_n) = \frac{D(1 + 3D/4)}{3N_0}, \quad (5.50)$$

and for the final atom number measurement uncertainty we can write

$$\text{Std}(\bar{E} - E_n) \approx \sqrt{\frac{D/3}{\langle N_{3n/4} \rangle}}. \quad (5.51)$$

Equations (5.45) and (5.51) demonstrate that due to the averaging, the stochastic uncertainty in sequence of images is equivalent to a noise induced by 1/3 of the total loss.

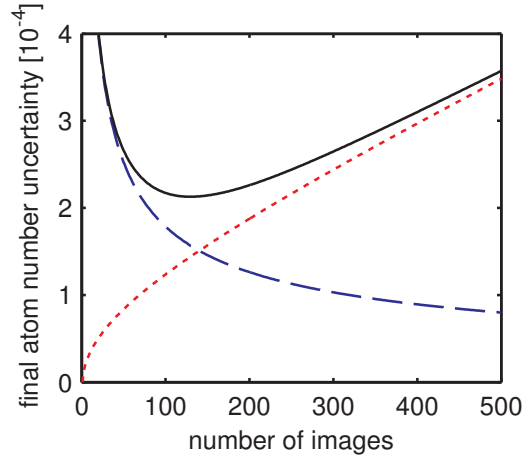


Figure 5.3: Scaling of the atom number measurement precision with the number of images. The total precision of an imaging sequence from Eq. (5.52) is shown with a black solid line. The stochastic noise contribution is shown with a red dotted line, while the photon shot noise contribution is plotted with a blue dashed line.

Finally we want to combine the photon shot noise and the stochastic noise, and search for the optimal number of images. Provided that the temperature of the cloud is well defined, we can set $E_T = 0$ in Eq. (5.12), and approximate the single image sensitivity to the atom number fluctuations by $\sigma'_{N,\text{ph}} = \sigma'_{\Sigma_S}/2 \approx 1.79 \cdot 10^{-3}$,

where we have used input from Eq. (5.21). The final atom number measurement uncertainty can then be estimated by

$$\tilde{\sigma}'_N(n) = \sqrt{\frac{(\sigma'_{N,\text{ph}})^2}{n} + \frac{d(n-1)}{N_0} \left[\frac{2n-1}{6n} + \frac{d(n-1)}{4} \right]}, \quad (5.52)$$

where we have used the full expression for the stochastic contribution from Eq. (5.49). The above expression and its constituting terms were evaluated in Fig. 5.3. There we can see that the precision is optimal for ~ 130 images, giving $\tilde{\sigma}'_N \approx 2.13 \cdot 10^{-4}$ at a cost of $\approx 28.6\%$ lost atoms, which is below the ‘atom shot noise’ limit $1/\sqrt{N_0} \approx 4.26 \cdot 10^{-4}$.

5.4 Shot noise limited sample preparation

We now want to investigate experimentally the correlation between two measurements separated by a controlled loss process. We induce the loss by ‘RF pulses’, that is brief repetitive reduction of the RF knife frequency. The pulse duration is $8.4 \mu\text{s}$ (set by the DDS programming rate), and the pulse separation was chosen to be $6 \times 8.4 \mu\text{s}$, which ensures that the cloud rethermalises with respect to the upper RF frequency.

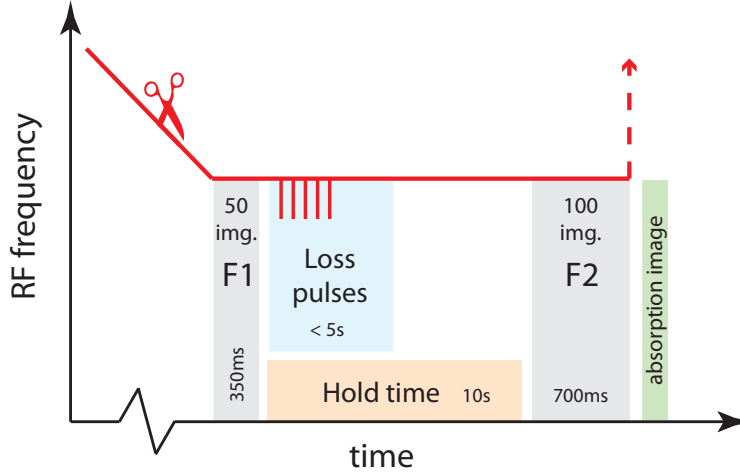


Figure 5.4: Experimental sequence schematics. The red line represents time variation of the RF cut frequency. F1 and F2 are the Faraday imaging series.

For simplicity, the RF power was hold constant for the whole experimental sequence. To achieve fine control over the applied loss, the RF frequency was reduced to 95% of the trap depth, which produces atom loss $\sim 10\%$ with 10^4 pulses and thus allows us to control the lost fraction with resolution 10^{-5} . This shallow cut method is generally addressing hot atoms, and therefore we observe

a cooling effect growing with the number of applied pulses. For a given amount of loss, this feature systematically reproduces the same effect and therefore is not detrimental to the correlation experiment.

The experimental sequence is outlined in Fig. 5.4. Forced RF evaporation is employed in the magnetic trap until the beginning of the first Faraday imaging series, ‘F1’, consisting of 50 images. At this point, the cloud contains on average 6.7×10^6 atoms at $18 \mu\text{K}$. With the exception of the applied loss pulses, the RF frequency is held at a constant value of 1900 kHz for the remainder of the experiment; this leads to an effective trap depth of $U_0 = 1340 \text{ kHz}$ ($64.3 \mu\text{K}$). The loss pulses are applied immediately after F1. To allow time for the loss pulses to be applied and for the cloud to thermalize, there is a 10 s delay between the end of F1 and the second set of Faraday images, ‘F2’, consisting of 100 images. In the absence of applied loss, the cloud contains on average 3.5×10^6 atoms at $9 \mu\text{K}$ after F2. To provide a cross-check of the prepared atom number, the magnetic trap is extinguished (after F2) and the atoms are absorption imaged after 10 ms time-of-flight.

Fixed applied loss

In the first experiment, we apply a fixed number of loss pulses. We have collected ~ 50 experimental runs for 13 different values of loss, including three data sets where the default in-trap loss was reduced by shortening the 10 s delay between F1 and F2. The final atom number and temperature obtained by the absorption imaging, as well as the mean signal in F2, are shown in Fig. 5.5. We observe $\sim 10\%$ fluctuations in the atom number, and correlated $\sim 1\%$ fluctuation in the temperature, caused mainly by fluctuations and drifts in the efficiency of laser cooling and transport in the beginning of the experiment.

To quantify the degree of correlation between the F1 and F2 measurements, we look at the correlation of mean signal sum in the two imaging series. Examples of signal sum traces for a few runs are shown in Fig 5.6 for a data set with a 10 s hold and no applied RF loss. We denote the *mean signal sum* in the k -th Faraday series ($k = 1, 2$) and j -th run by $S_{k,j}$ and define a dimensionless signal error

$$E_{k,j} = \frac{S_{k,j}}{\langle S_{k,j} \rangle_{\text{runs}}} - 1, \quad (5.53)$$

where the brackets denote the mean value over all runs in a given data set. As shown in Fig. 5.6, the two errors are nearly linearly correlated. The solid red line shows a second order polynomial fit to $E_{2,j}$ as a function of $E_{1,j}$: $E'_{2,j} \equiv E_{2,j}(E_{1,j})$. Note that the relative variation in signal sum is $\sim 20\%$, that is about factor of two larger than the variation in the atom number (see Eq. (5.12)).

To quantify the amount of correlation in a single run, we evaluate Allan deviation of $\Delta E_{2,j} \equiv E_{2,j} - E'_{2,j}$ over successive runs (see Eq. (5.20)). This reduces the

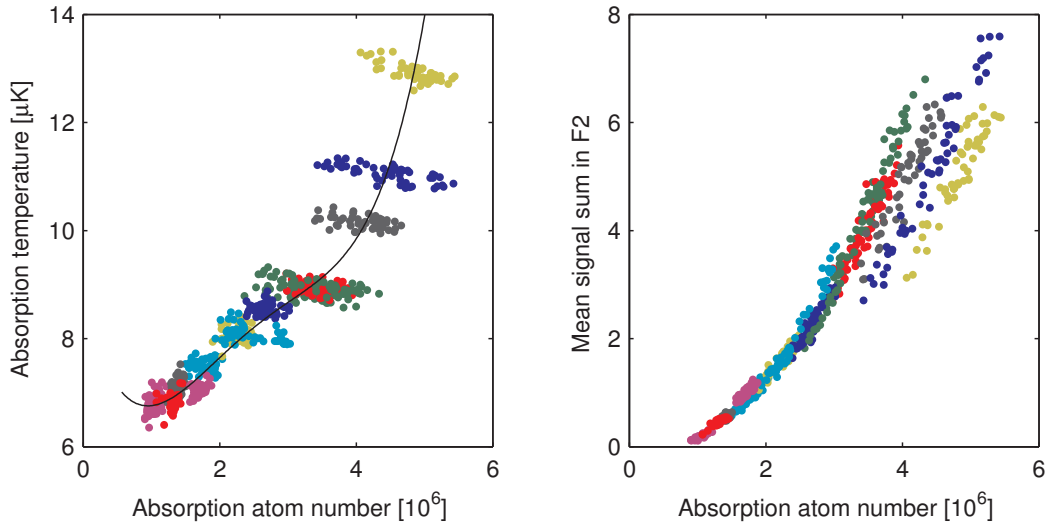


Figure 5.5: Atom number and temperature from absorption imaging and the mean signal sum in F2 for the 13 data sets with a fixed value of loss, distinguished with different colours. The black solid line in the left frame is a fourth order polynomial fit to the mean temperature and atom number in each data set.

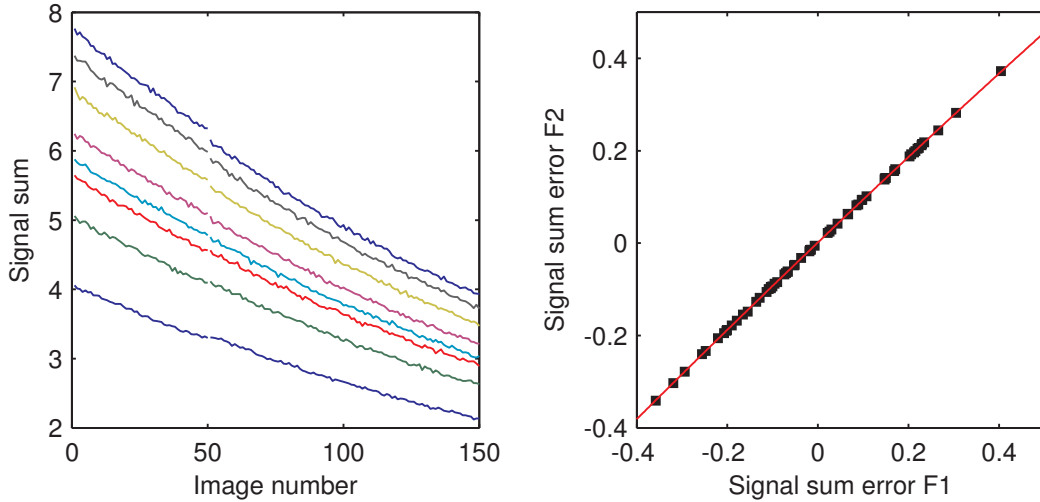


Figure 5.6: Example of the signal sum traces for few experimental runs (left) and correlation of signal sum error (right). The solid line is a quadratic fit to the correlation of $E_{1,j}$ and $E_{2,j}$. The data corresponds to the zero applied RF loss and 10s hold between F1 and F2.

contribution of slow drifts in the trap parameters, e.g. due to variation in the bias magnetic field.

The evaluated correlation of the signal for all the 13 data sets is shown in

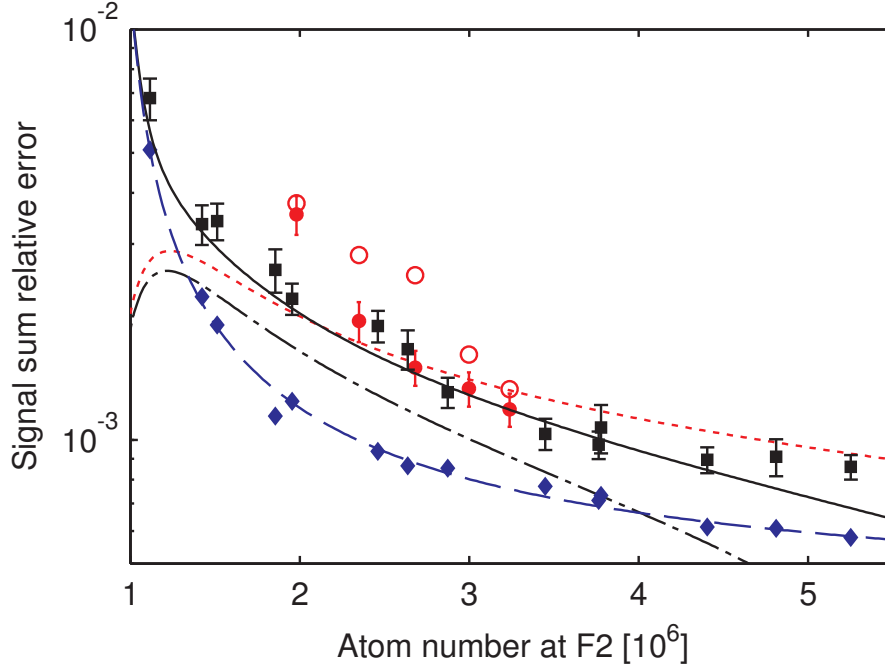


Figure 5.7: Fluctuations in the signal sum for the fixed (full black squares) and feedback controlled loss (red circles). The full red circles show the Allan deviation of the signal sum (over successive runs), while the empty circles show the standard deviation. The blue diamonds show the measurement uncertainty due to photon shot noise, and the blue dashed line is a $1/N$ type fit to the data (see text). The expected stochastic noise is plotted with black dash dotted line, while the ‘atom shot noise’ limit $1/\sqrt{\langle N \rangle}$ is plotted with red dotted line. The stochastic noise and the measurement precision are combined in quadrature and plotted with the black solid line. The errorbars were obtained by bootstrapping (see text).

Fig. 5.7 with black squares. The error bars were obtained by bootstrapping the Allan deviation, that is sampling with replacement 50 elements from the set of the observed two sample differences. The graph contains also curves for model of the expected correlation, which we discuss later.

Loss controlled with an online feedback

In a second experiment, we controlled the applied RF loss with feedback based on the F1 measurement. Specifically, the number of applied loss pulses $N_{\text{RF},j}$ in each run j was determined by a feedback function

$$N_{\text{RF},j} = gE_{1,j} \left[1 + qE_{1,j} + c(E_{1,j})^2 \right] + d_{\text{RF}}, \quad (5.54)$$

where g , q and c are the linear, quadratic and cubic gain respectively, and d_{RF} is the default loss. The feedback parameters were chosen so as to produce a stable

value of signal sum in F2, that is set $E_{2,j} = \text{const}$. For the application of loss, the value of $E_{1,j}$ is evaluated with respect to a mean signal sum from a reference data set. Alternatively, the feedback could also be defined directly as a function of $S_{1,j}$, but we find working with a normalized quantity more convenient.

The feedback parameters are optimized iteratively. First the feedback parameters are guessed, and a trial data set is acquired. The naturally fluctuating $E_{1,j}$ samples a range of applied pulse numbers. Comparing the obtained atom numbers in F2 with a reference sequence where no loss was applied, we calculate the lost fraction of atoms as a function of N_{RF} , thereby obtaining a calibration of the loss. For the trial set of $E_{1,j}$ we can then find the ideal lost fraction (if the goal was met), and by inverting the calibration find the ideal applied loss $N_{\text{RF},j}^{\text{I}}$ for each run. Finally we fit the function (5.54) to the set $E_{1,j}$, $N_{\text{RF},j}^{\text{I}}$ and obtain an improved guess of the feedback parameters. The process is repeated until the results are satisfactory, that is the residual deviation from a cubic fit to the obtained error $E_{2,j}$ is close to the standard deviation of $E_{2,j}$.

In practice, the gain optimization algorithm is not autonomous, and requires significant amount of human supervision. Due to technical problems with the stability of the ‘house’ cooling water, which cools the coils that generate the magnetic trap, and positioning of the MOT translation stage, the mean atom number can easily drift by 50% over the course of a day. We therefore have to ensure that the sampled atom numbers are within an admissible range $|E_{1,j}| < 0.5$, by occasionally adjusting the MOT loading level. We also observe slow drifts in the survived fraction of atoms, which we attribute to the changing parameters of the trap. This conclusion is based on the observed coinciding drifts in the cooling water temperature. Such technical imperfections occasionally demand a few additional iterations on the feedback optimization or slight manual adjustment of the gain parameters in order to reach the ‘physical’ limits of the system.

The feedback gain was optimized for 5 data sets with a variable amount of mean applied loss. The resulting absorption atom numbers and temperatures are shown in Fig. 5.8. Also shown are the values of the mean signal sum at F2 as a function of the atom number (compare with Fig. 5.5). The application of the feedback produces a stable signal for a wide range of initial atom numbers. The final atom number is not stable, because the same value of signal can be obtained by simultaneous adjustment of N and T , since $\Sigma_S \approx N^2/T$ (see Eq. (5.11)). In this experiment, larger initial atom numbers produce lower final atom numbers in order to counteract the increase in signal sum due to loss-induced cooling.

Figure 5.9 shows the value of $E_{2,j}$ as a function of $E_{1,j}$ for the feedback data set with a mean final atom number $2.48 \cdot 10^6$ (shown with green in Fig. 5.8). Here the errors are defined again in the sense of Eq. (5.53). For this data set, the feedback parameters were: $g = 22949$, $q = -0.224$, $c = -0.00945$ and $d_{\text{RF}} = 10071$. The values of $E_{2,j}$ were also plotted as a function of the run number to demonstrate the magnitude of the drifts in the trap parameters. Without any fitting involved, the

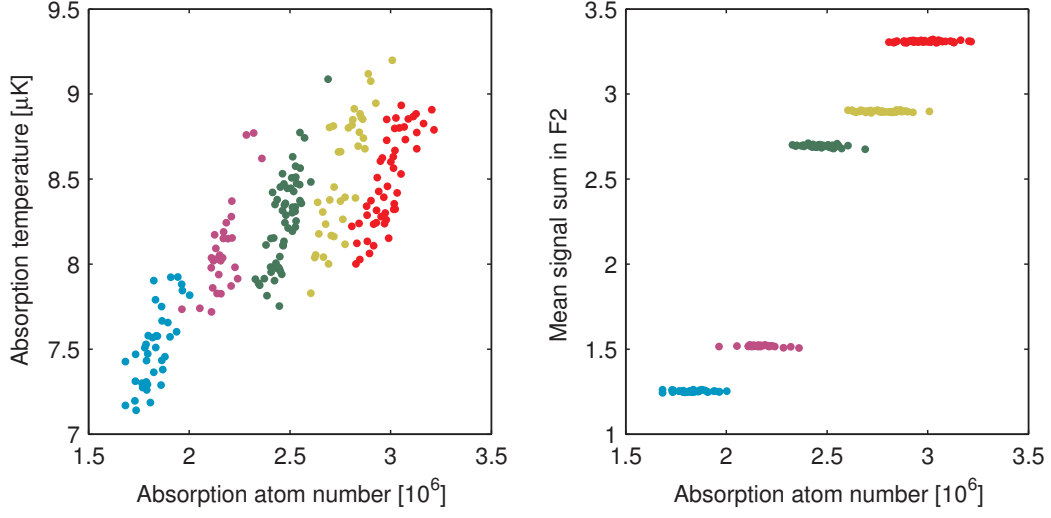


Figure 5.8: Atom number and temperature from absorption imaging and the mean signal sum in F2 for the 5 data sets with feedback stabilized signal sum, distinguished with different colours (compare with Fig. 5.5).

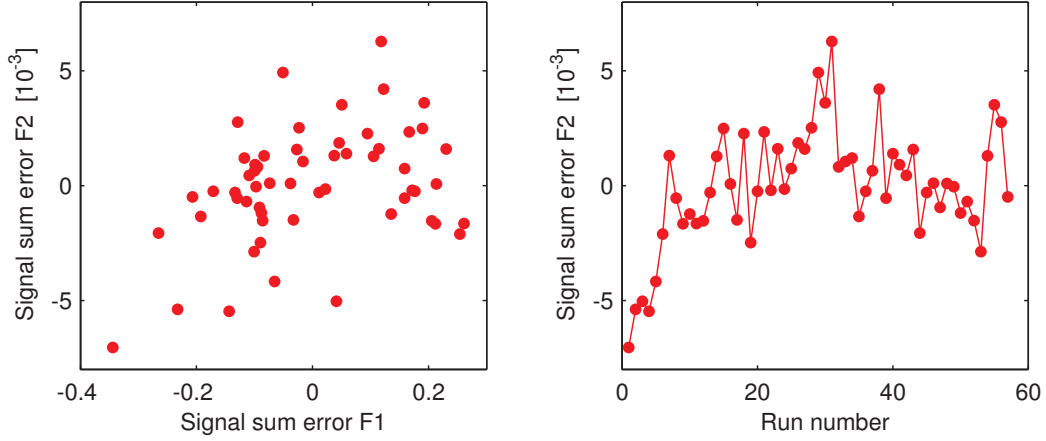


Figure 5.9: Example of a signal sum in F2 stabilized with RF loss controlled by feedback based on the signal sum at F1 (left). Demonstration of slow drift in the signal signal sum error $E_{2,j}$ as a function of the run number (right). The data corresponds to the data set with a mean final atom number $2.48 \cdot 10^6$ (shown with green in Fig. 5.8).

Allan deviation over the runs and the standard deviation of $E_{2,j}$ were evaluated and plotted in Fig. 5.7 with full and empty red circles respectively. Both quantities are comparable in size, however the additional noise due to slow drifts is detectable. Apart from the lowest atom number point, the Allan deviation for the feedback runs has the same value (within the errorbars) as the Allan deviation in the correlation

experiment, from which we conclude, that the feedback mechanism itself does not introduce any additional uncertainty.

Correlation noise model

The correlation of the F1 and F2 measurements is limited by two fundamental sources of noise: the signal sum measurement precision and stochasticity of the loss process separating the two measurements. To simplify the analysis, we assume that the atom loss present during the F1 and F2 imaging series is a part of the intermediate loss process. Based on Eq. (5.31), the expected amount of stochastic noise is approximated as

$$\sigma'_N \approx \sqrt{\frac{1 - \langle N_2 \rangle / \langle N_1 \rangle}{\langle N_2 \rangle}}, \quad (5.55)$$

where $\langle N_k \rangle$ is the mean atom number in the Fk imaging sequence.

The contribution of the measurement error is estimated from the single image precision in F1 and F2, evaluated for each run with Eq. (5.20) and rescaled with the factor $1/\sqrt{n_k}$ —accounting for the uncertainty of averaging over n_k images. The average measurement uncertainties of the F1 and F2 series were added in quadrature and plotted in Fig. 5.7 with blue diamond symbols (for the 13 fixed loss data sets). The blue dashed curve is a three parameter fit to the data: $a/(N-b)+c$, with $a = 870$, $b = 9.3 \cdot 10^5$ and $c = 3.8 \cdot 10^{-4}$. The measurement error grows with decreasing atomic density in the F2 imaging series, see Eq. (4.20).

According to Eq. (5.12), the atom number fluctuations (5.55) propagate into the signal sum as

$$\sigma'_{\Sigma_S} = \gamma_N \sigma'_N = \frac{\partial \Sigma_S}{\partial N} \frac{\langle N \rangle}{\langle \Sigma_S \rangle} \sigma'_N. \quad (5.56)$$

The temperature can also vary from run to run, but we assume that between the two measurements it follows a deterministic trend given by the initial condition at F1 (N and T) and the current trap depth, and therefore does not contribute to the noise in the correlation of the signal sum.

To complete the stochastic noise model for Fig. 5.7, we have to find the coefficient γ_N as a function of $\langle N_2 \rangle$. The required knowledge of the function $\Sigma_S(N, T)$ can be obtained from the data in Fig. 5.5 (fixed loss data sets), by fitting the signal sum at F2 as a function of N and T obtained from absorption images

$$\Sigma_S(N, T) = a_1 \frac{(N - a_5)^{a_2}}{T^{a_3}} + a_4, \quad (5.57)$$

which was inspired by Eq. (5.11). The resulting surface is shown Fig. 5.10, where $a_1 = (18.3 \pm 1.6) \cdot 10^{-18}$, $a_2 = 1.82 \pm 0.03$, $a_3 = 1.51 \pm 0.03$, $a_4 = 0.12 \pm 0.05$

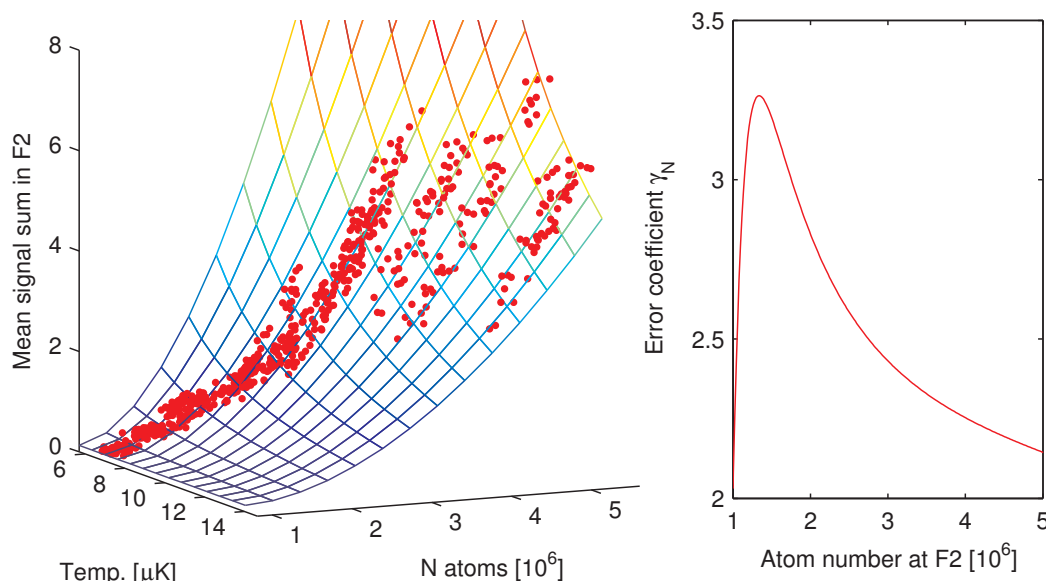


Figure 5.10: Characterisation of the signal sum function $\Sigma_S \equiv \Sigma_S(N, T)$ (left). The atom number N and the cloud temperature T were extracted from absorption images (red dots) for the 13 data sets with fixed applied loss, see Fig. 5.5. The surface mesh is a fit to the data with Eq. (5.57). The right frame shows the corresponding error propagation coefficient evaluated with Eq. (5.59) along the trajectory of mean temperature and atom number.

and $a_5 = (8.0 \pm 0.7) \cdot 10^5$. The above expression was chosen for its simplicity, because the exact functional dependence is complex (see Eq. (5.6)), and we only need to extract local properties of the function ($\partial\Sigma_S/\partial N$). The error propagation coefficient can then be obtained as

$$\gamma_N(N, T) = \frac{\partial\Sigma_S}{\partial N} \frac{N}{\Sigma_S} = a_2 a_1 \frac{(N - a_5)^{a_2 - 1} N}{T^{a_3}} \frac{N}{\Sigma_S} \quad (5.58)$$

$$= a_2 \left(1 - \frac{a_4}{\Sigma_S(N, T)} \right) / \left(1 - \frac{a_5}{N} \right). \quad (5.59)$$

In the next step, we fit the mean temperature for each fixed loss data set as a fourth order polynomial of the mean atom number to obtain the trajectory in the (N, T) space along which we evaluate Eq. (5.59). The trajectory is shown in Fig. 5.5 with a black solid line, and the resulting error propagation coefficient γ_N is shown in Fig. 5.10(right) as a function of atom number at F2. We see that for higher atom numbers (and higher temperatures), γ_N indeed approaches ~ 2 .

Finally, we plot the relative signal uncertainty from Eq. (5.56) for both the expected stochastic noise (black dash dotted line; Eq. (5.55)) and the limiting case of ‘atom shot noise’ $1/\sqrt{\langle N_2 \rangle}$ (red dotted line) in Fig. 5.7. Also shown is the combination of the stochastic noise with the detection noise (added in quadrature;

black solid line), which constitutes the total expected scatter in the correlation of the signal sum. Within the errorbars, the data is in a very good agreement with the model. At final atom numbers $\sim 4 \cdot 10^6$, the experimentally observed scatter even reaches values below the atom shot noise limit. Importantly, the signal sum can also be stabilized with a feedback to the level of the atom shot noise.

5.5 Stable sample production

In the preceding experiment, we have chosen to stabilize the signal sum, because this quantity is the most sensitive to the atom number fluctuations in a stochastic loss process. We have established that the precision of the feedback is limited only by the measurement precision and the stochasticity of the RF loss. Another important goal in our project is to enable a repeatable production of clouds with predefined properties, that is to stabilize the atom number and temperature. Simultaneous stabilization of N and T is required specifically in cases when the evaporative cooling is continued after the feedback, since the two parameters are coupled through the process of rethermalization; higher atomic density increases the rethermalization rate, and an increased temperature induces atom loss.

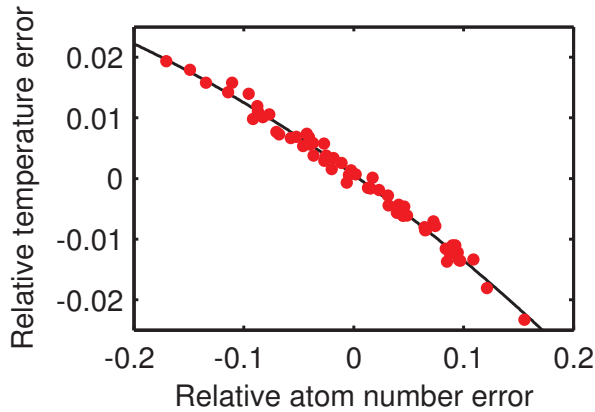


Figure 5.11: Relative deviation of temperature as a function of the relative atom number deviation evaluated from F2 for the fixed loss data set in Fig. 5.6 (no applied loss, 10 s hold between F1 and F2). The black solid line is a second order polynomial fit.

We observe that the initial evaporative process produces clouds with temperature dependent on the number of atoms. This can be seen best by extracting N and T from the Faraday images with a $\sin^2(\theta_g)$ fit to the signal image $S(x, y)$, where $\theta_g \equiv \theta_g(x, y)$ is a gaussian distribution for the Faraday rotation angles dependent on N and T . This procedure yields the two parameters with relative precision $\sigma'_N \approx 4.7 \cdot 10^{-4}$ and $\sigma'_T \approx 6.8 \cdot 10^{-4}$ for $N \sim 4 \cdot 10^6$ and $T \sim 10 \mu\text{K}$. Figure 5.11

shows the relative deviation of temperature as a function of the relative atom number deviation with respect to the mean evaluated from F2 for the fixed loss data set in Fig. 5.6 (no applied loss, 10 s hold between F1 and F2). We see that the number fluctuations are about an order of magnitude larger than the fluctuations of temperature, but the two quantities are very well correlated.

The functional relation between N and T is caused by the preceding evaporative process: a colder cloud can contain more atoms for a given depth of the trapping potential. The cloud variation is resulting from a different number of atoms initially loaded into the trap. At that point, both T and N can be independently uncertain. Once an evaporation has been performed, T becomes a function of N , and the uncertainty is essentially one-dimensional. The value of $\Sigma_S(N, T(N)) \equiv \Sigma_S(N)$ therefore unambiguously determines the cloud properties, provided that the derivative of $\Sigma_S(N)$ is non-zero. For our conditions this is indeed the case, as seen from Fig. 5.5. Importantly, if we continue to evaporate after the application of the feedback, we can choose the feedback parameters such that the signal sum is constant at a later point in the evaporation sequence, where the cloud is again rethermalized. Stable $\Sigma_S(N, T(N))$ will also imply a fixed atom number and temperature.

Atom number stabilization

In the above feedback experiment, the trap depth was kept constant. The applied RF cuts were very shallow (95 % of trap depth), which induced a cooling effect proportional to the number of loss pulses (removing hot atoms). Although the value of Σ_S was stable, N and T varied largely (in a correlated manner). In the following experiment, we have eliminated the cooling effect by setting the RF cut depth to 23 % (found experimentally). The feedback function was optimized to produce a stable atom number, while the temperature should continue to fluctuate by $\sim 1\%$. In order to roughly maintain the same loss effect (10 % with 10^4 pulses), we reduce the RF power during the application of the feedback to a fixed low value: ~ -30 dB compared to the default power during the evaporation.

Figure 5.12 shows the results of the experiment with a stabilized atom number. The feedback parameters were optimized iteratively in a fashion similar to the stabilization of the signal, that is by extracting the calibration of loss from trial runs with guessed feedback parameters. Figure 5.12(a) shows the atom number evaluated from the absorption images as a function of the signal sum error in F1. The blue squares show the data from reference runs (without applied RF loss), while the red circles are resulting from the stabilization. The solid curves show third order fits to the data. Figures 5.12 (b) and (c) show the relative stability of temperature and atom number (from absorption images) as a function of the signal sum error at F1. In accordance with our expectation, the temperature fluctuates by $\approx 1.4\%$. The atom number stability was $4.78 \cdot 10^{-3}$, implying that the natural

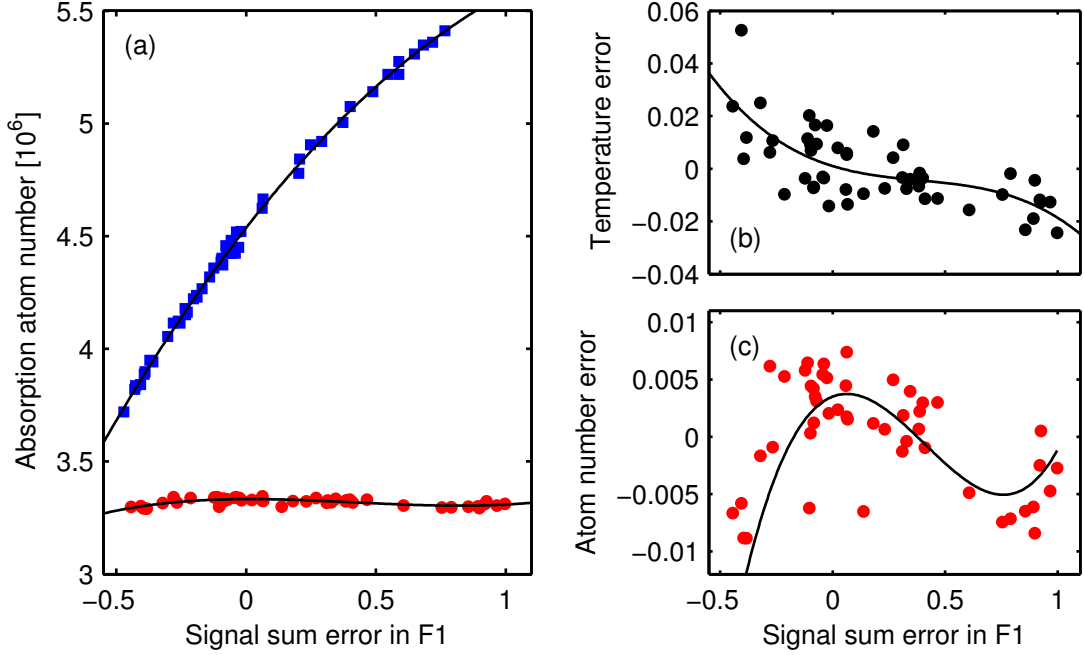


Figure 5.12: (a) Absorption atom number in a series of ~ 50 runs with (red circles) and without (blue squares) online stabilization, shown as a function of signal sum error at F1 (relative to the mean signal in the non-feedback runs). (b) shows absorption temperature error in the feedback runs relative to the mean, and (c) shows the relative atom number stability, both as a function of the signal sum error at F1. The black solid lines in all sub-figures are third order polynomial fits to the data.

atom number fluctuations ($\sim 11\%$) were reduced by a factor of 20. It appears that the feedback parameters could have been chosen still more optimally, since the residual deviation from the fit is $3.2 \cdot 10^{-3}$. It is so, because this data set samples a wider range of atom numbers than the trial data set (not shown) used to calibrate the loss response.

Finally, we comment on the precision of the absorption imaging. Before conducting this experiment, we have improved our implementation of this technique by installing a new camera (Andor iXon 897), which has a factor of two better quantum efficiency and better readout noise characteristics than the previously used model (iXon 885). We have also shortened the time between the two ‘absorption’ images (atoms and reference), which reduces noise due to low frequency vibrations of the optical elements. In a fashion similar to the Faraday detection, we have also implemented an active stabilization of the absorption imaging power on the FPGA (feedback loop with a proportional gain). Overall, we have improved the imaging precision by factor of six, and it is now $\approx 3.5 \cdot 10^{-3}$. We estimate that

the precision is further limited by the stability of the imaging laser frequency.

The goal of this experiment was to show that the Faraday signal can be used for high precision stabilization of the atomic clouds. This was verified by an independent measurement technique, the absorption imaging, where the achieved atom number stability was brought to the level of the measurement precision.

Detection of trapping potential variations

We have demonstrated that the thermal clouds can be stabilized with very high precision, even without application of subsequent evaporative cooling. The main goal, however, is to stabilize the result of the evaporation, that is produce a well defined Bose-Einstein condensate. Since the evaporation is a stochastic process similar to the examined RF pulse loss, we expect it also leads to atom number uncertainty of the order $1/\sqrt{N}$, where N is the final number of atoms. Practically, however, the most likely limit for a reliable production the ultracold clouds will now be the stability of the trapping potential.

As mentioned before, the magnetic trap is prone to trap bottom drifts inducing change of the well depth for a fixed end evaporation frequency. This can cause large fluctuations in the cloud temperature, atom number and consistently also the BEC fraction. The drifts are caused mainly by a varying bias magnetic field and/or a displacement of the coils due to thermal expansion.

The following experiment was carried out to investigate how well we can detect the trap variations. We apply the RF loss with a feedback based on F1 at RF = 1900 kHz and continue to evaporate towards the BEC in a usual manner until we reach a trap depth ~ 20 kHz (RF = 550 kHz). This produces a cloud with $N \approx 3.73 \cdot 10^5$ and $T \approx 297$ nK, which has $\sim 12\%$ of atoms in the BEC. The final clouds were detected in time-of-flight with the absorption imaging. At first, the F2 imaging was applied at RF = 1100 kHz in order to optimize the feedback parameters such that a stable signal sum is produced (also stable N and T). The RF cut was performed at 95 % of the trap depth. In a subsequent experiment, F2 was moved to RF = 650 kHz, that is, 120 kHz above the trap bottom (~ 1 s before the BEC formation), in order to enhance the sensitivity to the trap bottom drifts. Here the previously optimized feedback parameters were utilized.

The results of 21 experimental repetitions are shown in Fig. 5.13. The sub-figure (a) shows that the error of the signal sum at F2 ($E_{2,j}$) was decoupled from the influence of the initial atom number fluctuation detectable at F1. Any residual deviations of $E_{2,j}$ therefore must have been caused by effects not detectable/present in the F1 measurement, such as the exact position of the trap bottom. The sub-figures (b), (c) and (d) show the final temperature, the BEC fraction and the atom number extracted from the absorption images plotted as a function of $E_{2,j}$.

The behaviour is generally consistent with the effects of trap bottom drift. As opposed to Fig. 5.11, T and N are now positively correlated (simultaneous growth

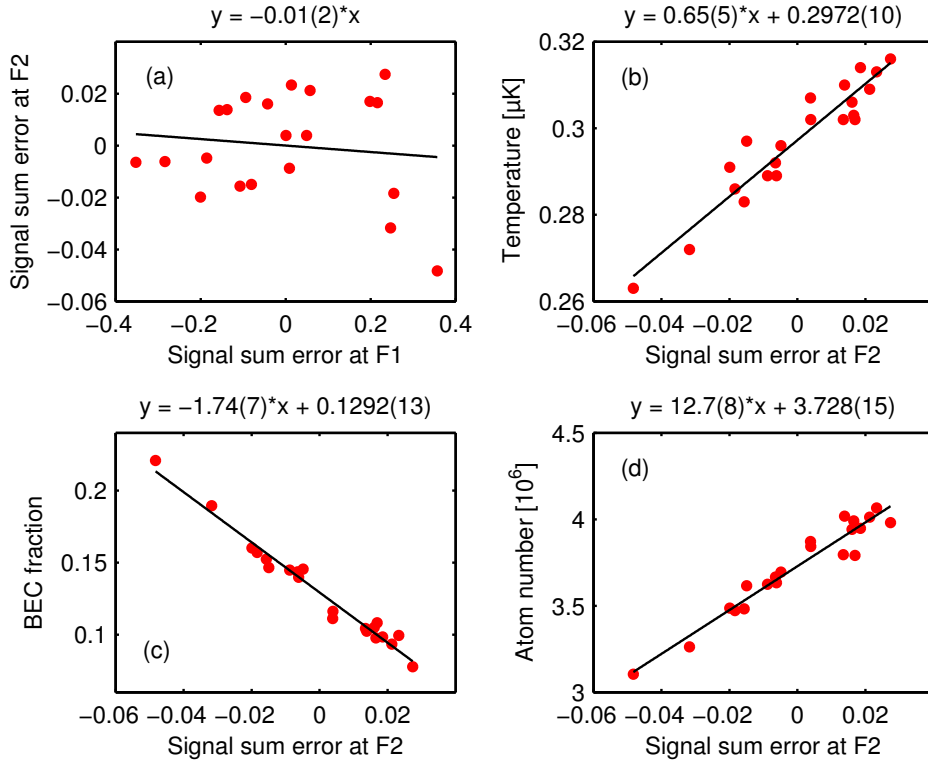


Figure 5.13: Detection of trap bottom drift. (a) shows the signal sum error at F2 ($E_{2,j}$) relative to the mean as a function of the signal sum error at F1. (b),(c) and (d) show the temperature, the BEC fraction and the atom number, respectively, evaluated from the absorption images and plotted as a function of $E_{2,j}$. The black solid curves are linear fits to the data. The fit parameters are shown above each plot.

with $E_{2,j}$): a deeper trap can hold bigger and hotter clouds. The atom number fluctuated by 7.0% while the temperature changed only by 4.6%, which explains why the correlation of T with $E_{2,j}$ has a positive slope ($\Sigma_S \approx N^2/T$). Remarkably, $E_{2,j}$ has the most precise correlation with the fraction of atoms condensed, see Fig. 5.11(c). The equations above each sub-figure show the fit parameters of the respective linear correlation functions (plotted with solid black lines). The residual relative deviation from the fit was 1.5% for the temperature and 1.8% for the atom number. The BEC fraction was ‘predicted’ with precision $5.8 \cdot 10^{-3}$. The sign of the BEC fraction correlation is consistent with the trap bottom drift effects: shallower trap implies higher condensed fraction.

To find the sensitivity to the trap bottom position, we have raised the end evaporation frequency by 30 kHz (in a different experiment), which led to a temperature increase ≈ 310 nK. Assuming that the temperature is proportional to the trap depth, this implies calibration 92 Hz/nK. In the above experiment, the tem-

perature varied by 53 nK (peak to peak), which implies change of the trap bottom by 5.1 kHz. Also, the temperature was resolved with 4.4 nK precision, implying 0.43 kHz resolution in the trap bottom detection. We conclude that the Faraday detection scheme resolves the variations of the trapping potential with very high precision.

To stabilize the trap bottom with a feedback, we can either actively alter the external bias field or change the end evaporation frequency as a function of $E_{2,j}$. The second option seems to be simpler to implement, since we already control the RF with the FPGA.

Conclusion and Outlook

The first part of this thesis, analysed the use of the Faraday effect as a non-destructive spatially resolved method for the interrogation of ultracold atomic clouds. In particular, dark field Faraday imaging (DFFI) was described and characterized, and compared with other non-destructive imaging methods. The work shows experimental applications of the method and presents its use in feedback experiments.

In an analytic approach, a framework for the signal-to-noise ratio of a general imaging technique was derived and related to the level of destructiveness. The analysis was applied to four common dispersive imaging methods including DFFI, which revealed, surprisingly, that in a low angle regime, the four methods provide effectively the same signal-to-noise ratio.

The precision of DFFI was evaluated in a broad range of atom numbers and temperatures, and it was shown that DFFI can facilitate a fast and precise non-destructive measurement of atomic cloud properties. Among the many practical applications, magnetometry and monitoring of in-trap oscillations were presented.

Fast online image evaluation on an FPGA was implemented, which provides a tunable feedback to the RF evaporation sequence and facilitates a reliable production of ultracold atomic clouds. The stochasticity of the controlled loss process was investigated in detail and was resolved with precision below the atom shot noise level. We have also developed a method to observe the effects of the trap bottom drift in a magnetic potential, which in further experiments can be stabilised. Importantly, the improved control, active stabilization and precise measurement techniques constitute a versatile toolbox for other experiments.

Non-destructive imaging perspectives

One of the future experiments will be a study of the spontaneous onset of the BEC formation, when the ground state population grows exponentially due to bosonic

stimulation once it has been seeded by vacuum fluctuations. An interesting pathway for extending the feedback applications would be high resolution monitoring and control of the in-trap cloud oscillations. The position of the cloud could be detected very precisely by ‘dividing’ the CCD into quadrants centred on the cloud. The measurement could be carried out on a small chip area, thus enhancing the sampling rate. As the cloud moves, the amount of light rotated by the cloud in the up-down and left-right frames will become uneven, which can be translated into displacement through a calibration function. Parametric feedback to the external bias field in the xy -plane could then be used to stabilize or amplify the oscillation, or drive a non-harmonic motion.

Spinor dynamics perspectives

In the project of spinor dynamics we have demonstrated creation of correlated wave packets due to spin changing collisions in a two-dimensional trapping geometry. In this thesis, I have presented an analytical study of the system supporting the wave packet like mechanism of the spinor excitations. It now remains to be verified experimentally that each lattice site of the 1D vertical lattice generates exactly one pair of wave packets due to bosonic stimulation and spontaneous symmetry breaking. Further progress could be achieved by isolating a single lattice site, which could be done with microwave addressing in the presence of a magnetic field gradient. It may also be interesting to investigate the influence of the condensate phase coherence, searching for a difference in the spinor dynamics in a superfluid and a Mott insulator state.

Part II

Quantum gates and Optimal Control

Introduction

The history of computing machines dates back to 2400 BC when Babylonians invented the abacus. Since then, many different mechanical and electronic computing devices have aided humans in keeping track of their complex models of reality. The search for the most powerful and efficient computing architecture has so far converged on silicon based semiconductors. The transistor was invented by John Bardeen, Walter H. Brattain and William B. Shockley at Bell Labs in 1947 [73]. Within ten years, the device effectively replaced all other computational hardware, and since then has transformed our lives like no other human invention.

A new shift of paradigm may be on the horizon: Quantum Information Processing. As the theoretical and practical knowledge of quantum mechanics improves, quantum systems start to be used as computation devices. Essentially, the initial state of the system encodes the input information and the interaction of the different degrees of freedom in time evolves or processes the information. The result of the computation is then read out by a final measurement of the state. For certain problems, quantum computers have the potential to outperform the conventional computers.

In computer science, problems are classified according to their complexity, that is scaling of the computational time (or number of operations) with the number of input bits n . The complexity of problems that are considered to be 'simple' scales polynomially with n . These problems belong to a class called **P**. On the other hand, hard problems require an exponentially growing computation time [74].

Finding a solution to a given problem is generally harder than verifying that a given solution solves the problem. Problems whose solution can be verified in a polynomial time are called **NP**. For example, it is believed that factorising a big integer number k into prime numbers is not a **P** problem, however checking whether a given number divides k can be found easily, and therefore number factorisation is an **NP** problem.

Factorising large numbers is one of the tasks which can be solved with a quantum computer in a polynomial time. Number factorization or similarly complex problems form the base of commonly used public key encryption systems, such as the Rivest-Shamir-Adleman (RSA) algorithm. In these protocols, the receiver of the message publishes a key, which can be freely used to encrypt messages. The messages can be decrypted only with a secret key (known solely to the receiver) analogous to a large prime factor of the public key. If a quantum computer could find the private key in a polynomial time, it would pose a serious threat to the security.

Apart from number factorization, there are only few other known problems that can in principle be solved faster with a quantum computer. An unstructured database with n entries can be searched for an element matching a certain condition with \sqrt{n} queries by means of the Grover search algorithm [75]. Compared to conventional computers, which use on the order of n queries, the speed up is only quadratic. Nevertheless, for a large database this could make a practical difference.

Due to the non-intuitive character of quantum mechanics, it is generally hard to find quantum algorithms that outperform the classical computers. All classically solvable problems can also be solved on a quantum computer, but gaining an advantage requires the use of some purely quantum effects, which are poorly captured by our intuition.

A more direct application of quantum computers is the simulation of other quantum systems. This task becomes quickly intractable with classical computers, since the number of memory registers required just to hold the state of a quantum system grows exponentially with the number of degrees of freedom, that is the number of particles. The rapid progress experienced currently in the information technologies originates mainly from the miniaturisation of elementary electronic components. As these active parts become smaller, eventually quantum mechanical phenomena begin to play a role and quantum mechanics has to be taken into account in their design. Being able to simulate complex quantum system is thus of paramount importance.

Quantum gates

In analogy to classical bits, quantum computers operate on quantum bits or qubits, which are carried by two level quantum systems prepared generally in a superposition

$$|\phi\rangle = c_1|0\rangle + c_2|1\rangle. \quad (7.1)$$

Single qubit quantum gates are essentially unitary operations, which can be represented by two-dimensional matrices operating on the vector $\begin{pmatrix} c_1 \\ c_2 \end{pmatrix}$. For example,

a quantum NOT gate is represented by

$$X \equiv \begin{pmatrix} 0 & 1 \\ 1 & 0 \end{pmatrix}, \quad (7.2)$$

and swaps the coefficients c_1 and c_2 . Another important gate is the Hadamard gate

$$H \equiv \frac{1}{\sqrt{2}} \begin{pmatrix} 1 & 1 \\ 1 & -1 \end{pmatrix}, \quad (7.3)$$

which transforms the states $|0\rangle$ and $|1\rangle$ into the basis

$$\begin{aligned} |+\rangle &\equiv \frac{1}{\sqrt{2}}(|0\rangle + |1\rangle), \\ |-\rangle &\equiv \frac{1}{\sqrt{2}}(|0\rangle - |1\rangle). \end{aligned} \quad (7.4)$$

An essential requirement for computation is conditional execution or the interaction of qubits. Most simply, this can be achieved with two-qubit gates which operate on the four dimensional vector space

$$|\phi\rangle = c_1|00\rangle + c_2|01\rangle + c_3|10\rangle + c_4|11\rangle. \quad (7.5)$$

A prototypical two-qubit gate is the *controlled*-NOT or CNOT gate, which in the matrix formalism can be represented by the unitary matrix

$$U_{\text{CX}} \equiv \begin{pmatrix} 1 & 0 & 0 & 0 \\ 0 & 1 & 0 & 0 \\ 0 & 0 & 0 & 1 \\ 0 & 0 & 1 & 0 \end{pmatrix}. \quad (7.6)$$

The state of the second qubit (called *target*) is negated

$$|0\rangle \leftrightarrow |1\rangle \quad (7.7)$$

when the input state of the first qubit (called *control*) is $|1\rangle$ and remains unchanged for control $|0\rangle$. The CNOT gate is an equivalent of the universal logic NAND gate in that: *Any multiple qubit logic gate may be composed from CNOT and single qubit gates* [74].

Quantum computation has not yet found the winning physical architecture. Research is carried out in many areas, with the most prominent candidates based on trapped ions [76], quantum dots [77], superconductors [78], neutral atoms in optical lattices [79] and nuclear magnetic resonance [80], to name a few. In all cases, the research is still at the level of development of elementary quantum gates that could form the basis for a scalable quantum computer.

In the first part of my thesis, I described experiments aimed at the robust production of cold atomic gas samples. When further cooled those produce an ultracold gas, where the motional degrees of freedom have to be described by quantum mechanics. Many experiments have been carried out to demonstrate the matter wave properties of both condensates [81] and atoms trapped in an external potential [45]. In the following we consider a proposal for a quantum CNOT gate operating on qubits encoded in the motional degrees of freedom of individual trapped atoms.

Spatial mode encoding has primarily been used in optical qubits, in the context of continuous variable quantum computation [82], or in dual-rail schemes [83]. Certain clever proposals for realizing phase gates in double-well potentials [84, 85, 86] have also employed vibrational modes of trapped atoms. However, the gate outcome is contained in the phase of the states and readout was shown to require intermediate encoding on internal atomic states [87]. In contrast, we encode qubits in the population distribution of atoms in a triple-well potential, and readout simply involves determining the presence or absence of atoms in specific wells, possible even for single atoms by direct imaging methods [88].

The CNOT gate design is further generalised to perform an atomtronics transistor function [89, 90, 91], where the flow of one BEC can be directly controlled by a presence of another species BEC. Existing designs are based on manipulating resonant coupling of lattice sites by adjusting the chemical potential or external bias fields [89, 90, 92]; or on manipulating atomic internal states to transport holes [93], or spin [94].

Optimal control and the quantum speed limit

The main task in implementing efficient quantum gates is to drive a given system by a time varying control from a certain initial state to a given target state. Often the time dependence of the control is chosen heuristically, which does not yield a sufficiently high fidelity required for scalable quantum computing. However the performance of the gate can be further improved by optimizing the control numerically.

Generally, many quantum processes intended for practical applications involve elaborate models, where the final fidelity can only be determined in a simulation, and manually choosing an efficient control is very difficult. The theory of optimum control [95] provides means for improving the fidelity for a given process duration or even shortening the process at the expense of some loss of fidelity, which may ultimately become advantageous due to the increased repetition rate and reduced decoherence.

As realized by Mandelstam and Tamm [96], the time-energy analogue of the quantum mechanical uncertainty principle provides a general limit for the time evolution of observables. This principle led Bhattacharyya [97] to the formulation

of the ‘Quantum Speed Limit’ (QSL), which asserts that a system evolving from $|\psi_i\rangle$ to $|\psi_f\rangle$ in time T must fulfil $\Delta E \times T \geq \arccos(|\langle\psi_i|\psi_f\rangle|)$, where ΔE is the energy uncertainty of the system. Aharonov and Anandan [98] later identified $\int_0^T \Delta E dt$ with the path length of the trajectory in Hilbert space, and showed that its value is limited by $\arccos(|\langle\psi_i|\psi_f\rangle|)$. This geometrical interpretation of the QSL motivated Carlini *et al.* [99] to search for the optimal path in Hilbert space. Recently, Caneva *et al.* [100] demonstrated the existence of the QSL based on the convergence of an Optimum Control (OC) algorithm.

The quantum speed limit is often stated in terms of the minimum time $T = T_{QSL}$ required to obtain complete transfer into a given target state. At durations shorter than T_{QSL} , the target state cannot be fully reached and the high operation speed comes at the expense of a fidelity lower than one. The standard QSL provides only a lower bound for T_{QSL} , which can be reached by an ideal Hamiltonian driving the system along a geodesic in Hilbert space. In most systems, however, such a Hamiltonian is not available and the actual T_{QSL} is substantially larger than that lower bound. The time-fidelity trade-off—a particular case of Pareto optimization [101]—has previously been evaluated for specific quantum systems using mainly numerical means [102, 103, 104]. The derivative of fidelity with respect to process duration was also obtained analytically for a uniform extension of the process [105, 106]. However, an intuitive interpretation of the trade-off as well as a treatment of non-uniform time variations has been missing.

In the following we address the problem of quantum speed limit in the framework of Hilbert space geometry offering an intuitive interpretation of optimal control algorithms. This approach is applied to non-uniform time variations, which yields the time fidelity trade-off expressed in terms of the direct Hilbert velocity and provides a robust prediction of the quantum speed limit.

Structure of part II

The second part of the thesis is organized as follows:

- Chapter 8 presents a theoretical proposal for the implementation of a quantum CNOT gate operating on the spatial degrees of freedom of atoms trapped in a triple well potential. The design is further generalized to provide a transistor-like action with two interacting Bose-Einstein condensates.
- Chapter 9 analyses the problem of quantum speed limit and optimum control in the framework of Hilbert space geometry. The trade-off is quantified in terms of a direct Hilbert velocity, which closely ties to the notion of geodesics. We also provide a numerical example applying the formalism to a multi-particle system generating entanglement through a Rydberg blockade.
- Chapter 10 summarizes our theoretical results and outlines interesting pathways for extending this work.

An atomtronics transistor for quantum gates

8.1 Static operation scheme

Quantum Gate

We consider two independently controlled orthogonal triple wells that can be switched between two ‘T-shaped’ configurations, shown in Fig. 8.1(a,b), containing two mutually-interacting species, each free to move only along one direction. Single qubits are encoded in the spatial degrees of freedom of the two species, with $|0\rangle$ and $|1\rangle$ corresponding to localizations in the respective extreme wells. In any given operation cycle, the motion of one species is kept frozen by deep potentials, so *only one spatial dimension (1D) needs to be considered at a time*. Without loss of generality *we refer to the active species as A and the passive as B*.

Along the active direction, we label the wells *left, central, right*, with effective qubit definitions [Fig. 8.1(d,e)]: Qubit A is in state $|0\rangle$ or $|1\rangle$ if species A is localized in the left or right well respectively; Qubit B is in state $|0\rangle$ or $|1\rangle$ when species B is absent or present in the central well, with ‘absent’ corresponding to localization in the extreme transverse well. A two-qubit CNOT gate can be then designed [Fig. 8.1 (f)] such that after a set time T , qubit A is negated if qubit B is in $|1\rangle$, but is unchanged if qubit B is in $|0\rangle$. Notably, such a configuration allows for simple scalability since the roles (‘control’ or ‘controlled’) of the two species can be switched in different cycles.

We first consider a *static* triple-well potential to describe the gate operation principle, which involves the three lowest eigenstates ϕ_0, ϕ_1 and ϕ_2 for species A in the triple-well, with eigenenergies $E_0 < E_1 < E_2$. The potential is symmetric about the central well minimum [Fig. 8.2], so ϕ_1 has its *node* there while ϕ_0 and

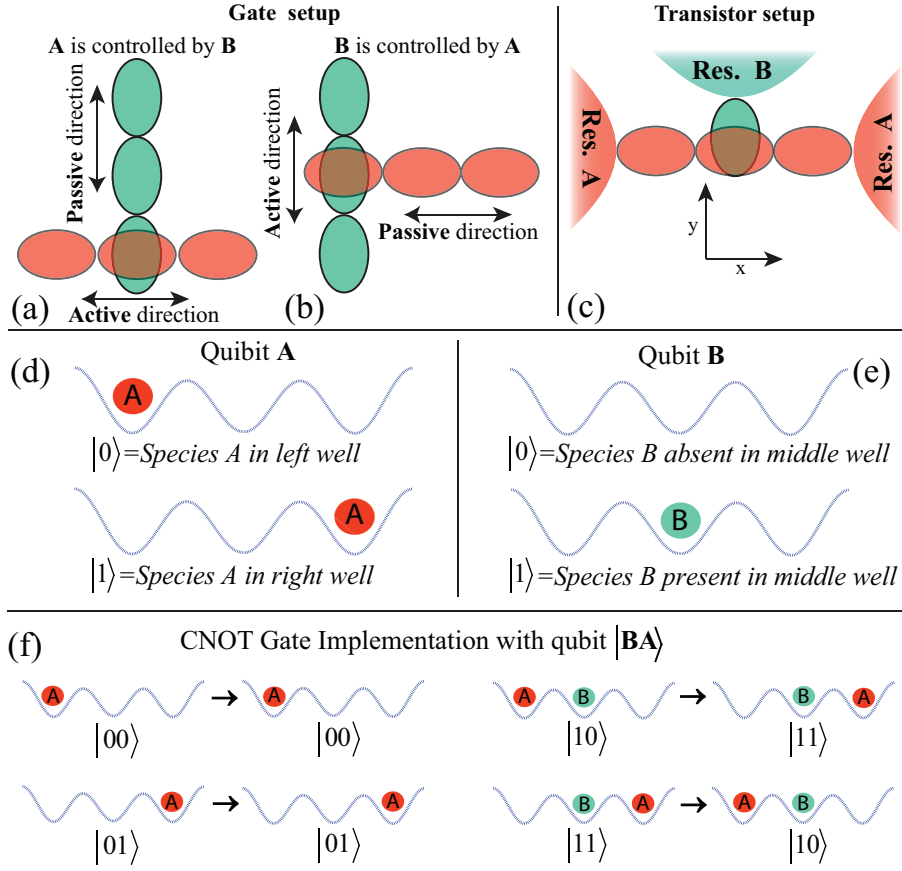


Figure 8.1: (a)-(b) Interchangeable gate configurations where role of A and B can be swapped; (c) Transistor configuration connected to reservoirs. (d)-(e) Effective qubit definitions in a specific cycle; (f) CNOT quantum gate operation.

ϕ_2 have anti-nodes. Therefore, when species B is present in the central well, the repulsive A-B interaction V_{AB} will shift up the energies E_0 and E_2 , but hardly affect E_1 . A class of potentials exists where the presence of atom B will raise E_0 and E_2 by the same amount, thus leaving $\Delta E_2 = E_2 - E_0$ unchanged while decreasing $\Delta E_1 = E_1 - E_0$.

Species A is prepared in a state $|\psi_A(t=0)\rangle$ localized in one of the two extreme wells. Even though we choose this state to simply be a Gaussian with minimized energy, it is almost completely superposition of only the three lowest eigenstates. The initial phase relations among the eigenstates, shown in Fig. 8.2(a,b), are such that $\phi_0(0)$ and $\phi_2(0)$ add up constructively with $\phi_1(0)$ in one extreme well and destructively in the other. If present, $|\psi_B(0)\rangle$ is a minimum energy Gaussian localized in the central well. The process can work starting from either extreme well due to the bilateral symmetry of the potential.

We adjust *four* degrees of freedom of the system: position, width and height of the two barriers, and V_{AB} . By simple reparametrization [107], two are degrees of

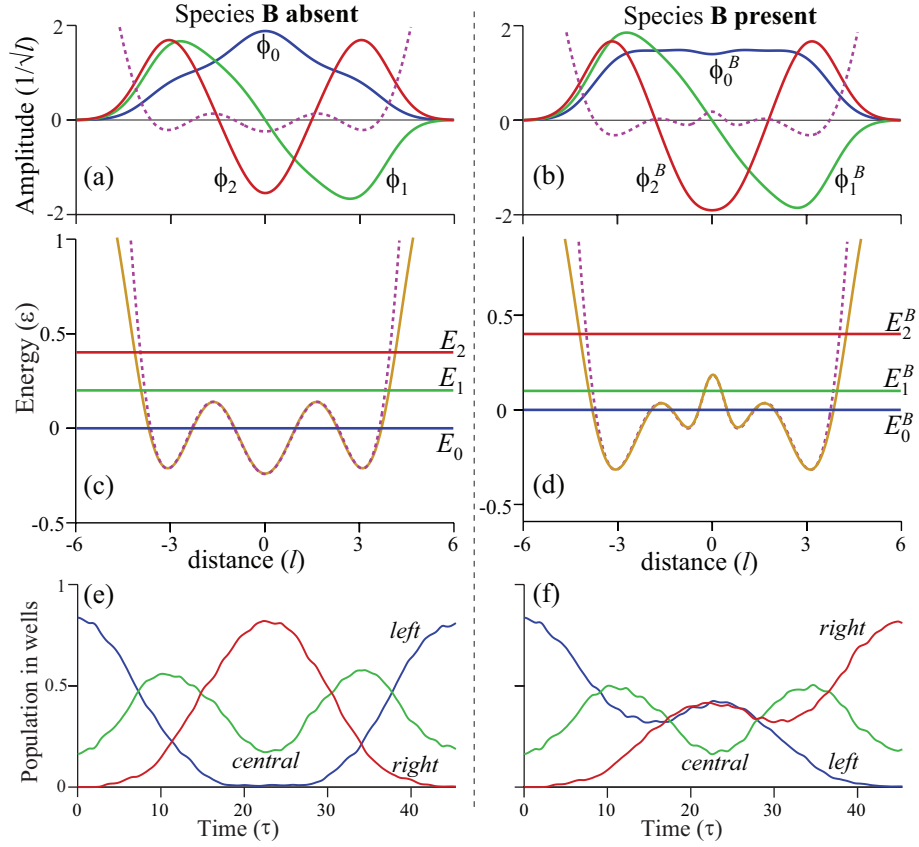


Figure 8.2: Static potential: Species B absent (left), present (right): (a, b) The three lowest eigenstates and (c,d) corresponding eigenenergies of species A in the triple-well. The dotted lines show the potential from Eq. (8.4), which generally matches a lattice potential (solid line in (c,d)) created with three harmonics. With B absent, $\Delta E_2 = 2 \times \Delta E_1$ but with B present, $\Delta E_2^B = 4 \times \Delta E_1^B$. (e,f) The single-well occupation versus time for species A, with species B absent/present. The units are defined in table 8.2.

freedom used to fix the time scale of operation, and to set the condition that with species B *absent*, the energy separations satisfy $\Delta E_2 = 2 \times \Delta E_1$ so that after time $T = h/\Delta E_1$, the dynamical phases acquired by the three eigenstates are offset by multiples of 2π leading to the revival of the initial state in the *initially occupied* extreme well. The remaining two parameters are set to ensure that with species B *present* $\Delta E_2^B = \Delta E_2$ remains unaltered while $\Delta E_1^B = \Delta E_1/2$ is halved, as seen in Fig. 8.2, so that now $\Delta E_2^B = 4 \times \Delta E_1^B$.

The antisymmetric state ϕ_1 evolves at half the rate than without B, hence after the same time of evolution T it has an opposite phase, or π offset, relative to the symmetric states. This results in localization of the species A in the *initially empty* extreme well. Thus, the presence or absence of the species B leads to the revival

of species A in the original well or transfer to the other extreme well after a set time T , implementing the CNOT gate.

Cold atom transistor

The gate operation described above is the specific case, of fixed V_{AB} , of a general transistor mechanism in which species B is used to precisely control the flow of species A between the extreme wells. A schematic of operation as an atomtronics transistor is shown in Fig. 8.1 (c), where the left and right wells of the triple-well system are coupled to two reservoirs of species A, while the central well is coupled transversely to a reservoir for species B. Since V_{AB} directly affects the dynamic evolution of species A it controls the transfer rate from the left well to the right well.

A range of interaction strengths can be found for feasible parameters where we can smoothly adjust ΔE_1 which fixes the period for a gate cycle $T = h/\Delta E_1$. Therefore, if we instead fix the period of each cycle at T and vary V_{AB} , the transfer per cycle can be controlled; the fraction of species A transferred varies smoothly from zero to complete transfer (inset of Fig. 8.3(a)). Since V_{AB} depends on the interaction strength g_{AB} and the density $|\psi_B|^2$ of species B, for large g_{AB} small variations in $|\psi_B|^2$ can be used to control a large flux of species A, creating an amplification effect. As V_{AB} is further increased, transfer of species A is eventually blocked.

8.2 Physical models: Single atoms and Dual species condensates

During operation the dynamics is kept 1D along the active direction, with transverse motion suppressed by tight harmonic potentials, taken to be cylindrical with angular frequency ω_\perp . We propose implementation in two distinct systems of ultracold atoms:

(i) *Single atom per species in triple-well optical superlattices*, described by an effective Hamiltonian, with 1D hard-core bosonic *inter*-species interaction strength g_{AB} ,

$$\hat{H} = \sum_{j=A,B} \left[\frac{-\hbar^2}{2m_j} \frac{\partial^2}{\partial x_j^2} + V_j(x_j, t) \right] + g_{AB} \delta(x_A - x_B). \quad (8.1)$$

This is obtained from the 3D Hamiltonian by integrating out the transverse degrees of freedom [108]. The potential for each species $V_j(x_j, t)$ is formed with three harmonics, with the third harmonic generated by counter-propagating beams with

wavelength λ and the two lower harmonics obtained using the same light intersecting at angles to increase the spatial periodicity of their interference pattern along the triple-well direction.

(ii) *Coupled BEC's in optical dipole traps* described by

$$i\hbar\partial_t\psi_A = \left(-\frac{\hbar}{2m_A}\partial_{xx} + V_A + g_{AB}|\psi_B|^2\right)\psi_A \quad (8.2)$$

$$i\hbar\partial_t\psi_B = \left(-\frac{\hbar^2}{2m_B}\partial_{xx} + V_B + g_{BA}|\psi_A|^2 + g_{BB}|\psi_B|^2\right)\psi_B. \quad (8.3)$$

To ensure linear dynamics, species A has no self-interaction (possible with Feshbach resonance [109]). The triple wells are created with blue-detuned laser barriers in a harmonic well of angular frequency ω :

$$V_A(x, t) = \frac{1}{2}m_A\omega_A x^2 + U\left[e^{-\frac{(x-d)^2}{2\sigma^2}} + e^{-\frac{(x+d)^2}{2\sigma^2}}\right]. \quad (8.4)$$

In simulations we assume the same potential (8.4) for species B but magnified $V_B = 20 \times V_A$ to keep it localized even when the potential varies (as in the dynamical case described next). In practice, V_B can be smaller since localization along the active direction can be done by a *separate* potential that provides the lateral confinement for the passive direction (Fig. 8.1(a,b)).

Both systems have similar outcomes, because the lattice potential in Eq. (8.1) can be made almost identical to Eq. (8.4) by suitable choice of parameters as shown in Fig. 8.2(c,d). The time-evolution is then similar for both models, because due to strong confinement the self-interaction of species B has little effect on the dynamics – which justifies the factorization of the two-component wavefunction $|\psi_{AB}\rangle = |\psi_A\rangle|\psi_B\rangle$ so that Eqs. (8.2) (apart from the self-interaction term for B) can be derived as the equations of motion for the Hamiltonian (8.1) by taking the projections $\langle\psi_B|\hat{H}|\psi_{AB}\rangle$ and $\langle\psi_A|\hat{H}|\psi_{AB}\rangle$.

Thus here we display simulations that combine features from these almost equivalent scenarios, using potential (8.4) in the Hamiltonian (8.1). We time-evolve by a split-operator method applied to a 2D wavefunction of the two species. The evolution of the population of species A (initially in the left well), in the *static* triple-well during a gate cycle, is shown in Fig. 8.2 (e,f). The populations in the wells are computed by integrating $|\psi_A(x, t)|^2$ over the intervals $(\infty, -D)$, $(-D, D)$ and (D, ∞) , where $\pm D$ are the coordinates of the barrier maxima—different than the barrier positions d .

8.3 Dynamic gate and Transistor

The static Hamiltonian demonstrates that both gate and transistor mechanism operate by evolution of dynamical phases. But, to put this in practice, two issues need to be addressed: (i) preparation and readout of the quantum bits and (ii) initiation and termination of each operation cycle. Both goals can be achieved if

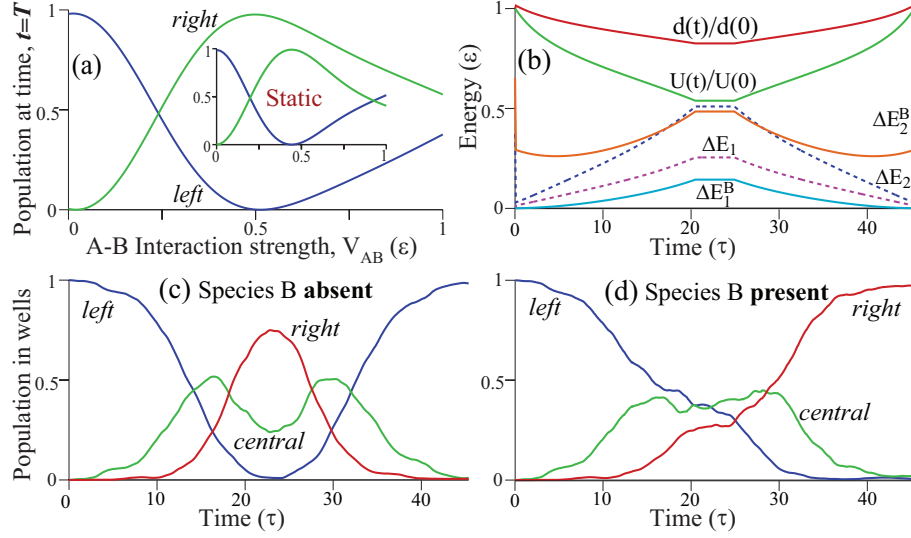


Figure 8.3: Dynamic potential: (a) Populations in left and right wells after one period $t = T$, as functions of V_{AB} ; (inset) similar behavior is seen in the static potential. (b) Smooth time evolution of the dynamical parameters: barrier position d and barrier amplitude U ; also shown are the energy separations with species B absent ($\Delta E_1^B, \Delta E_2^B$, dotted lines) and present ($\Delta E_1^B, \Delta E_2^B$). The single-well occupation versus time for species A, when species B is (c) absent and (d) present.

the initial and final states of species A are the ground state of a single, isolated well.

The initial state is kept localized by suppressing the tunneling, that is making the barriers high and the central well shallower than the extreme wells. This ensures $\Delta E_2 \gg \Delta E_1$ so that ϕ_2 is unoccupied and the state is a superposition of the almost degenerate ϕ_0 and ϕ_1 . The gate operation is initiated by an abrupt decrease of the central well, to set $\Delta E_2 = 2 \times \Delta E_1$. The state is now a superposition of the three lowest eigenstates, and population begins to flow due to the evolution of their phases. To speed up the tunneling rate, ΔE_1 and ΔE_2 are increased, while maintaining $\Delta E_2 = 2 \times \Delta E_1$. This is done via a smooth decrease of $U(t)$ and $d(t)$, as shown in Fig. 8.3(b).

The potential energy variation induces a non-adiabatic coupling

$$\mathcal{A}_{kn} = \frac{i\hbar \langle \phi_k | \partial_t \hat{H} | \phi_n \rangle}{(E_k - E_n)^2}, \quad (8.5)$$

which may drive some population exchange between the immediate eigenstates of the Hamiltonian. Since the Hamiltonian is kept bilaterally symmetric, such coupling occurs only between states of the same parity. In our simulations, the net population in the three lowest eigenstates is conserved by setting the strongest out-coupling A_{13} to a low value 0.07, which determines the speed of variation of the

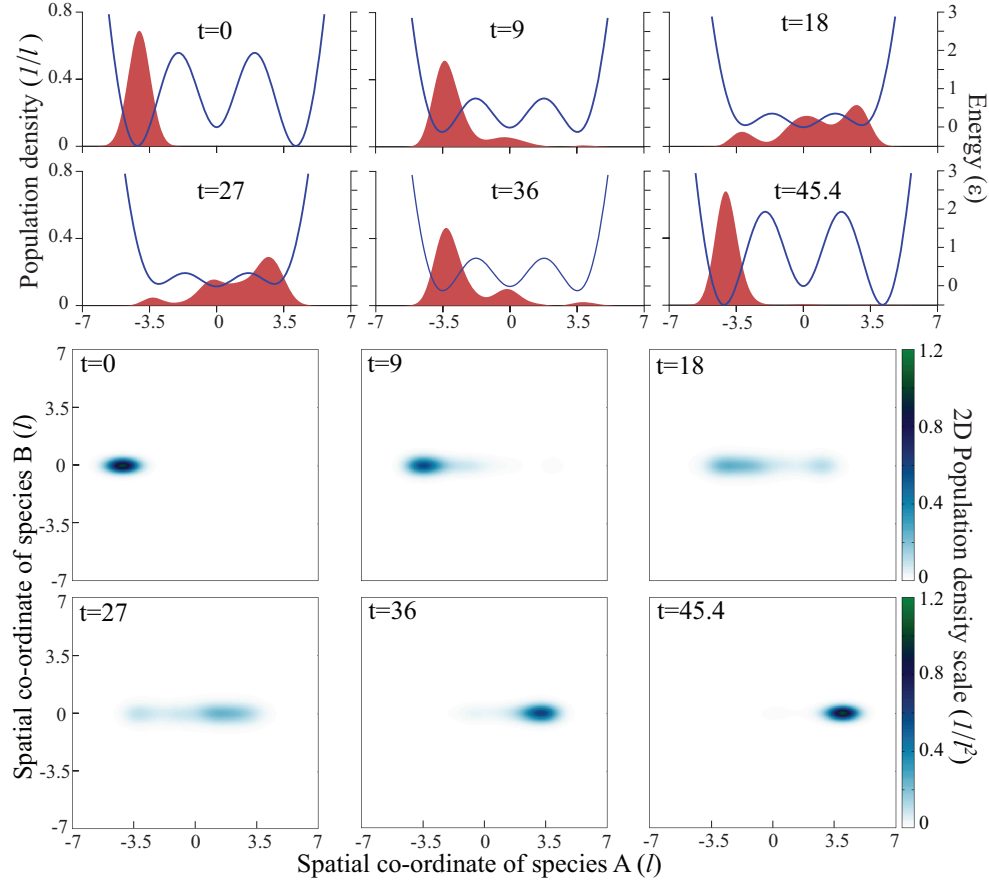


Figure 8.4: Snapshots of population density in a gate cycle of period T (time units of τ) corresponding to Fig. 8.3 (c) and (d): *upper panels*: Density (left axis) of species A when species B is absent; the potential is shown as blue lines (right axis); *lower panels*: Joint density of species A (horizontal axis) and species B (vertical axis) when species B is present. The units are defined in table 8.2.

potential through Eq. (8.5). The path selecting algorithm stops when the phase difference of the states ϕ_0 and ϕ_1 is π , that is half of the revival; the second half is just a mirror image in time.

The parametric paths, shown in Fig. 8.3(b), are determined from the properties of the potential with species B absent. We ensure that with species B present, exactly the same path leads to species A localizing in the opposite well, by tuning V_{AB} to maximize gate fidelity, measured by the probability of the projection of the final state at $t = T$ on the desired gate outcome.

8.4 Feasibility analysis

In this section, we demonstrate the feasibility for both individual atoms and BEC by showing that our assumptions can be met by currently available physical systems. We indicate the active direction by coordinate x and assume cylindrical symmetry in transverse directions, denoted by ‘ \perp ’.

Individual atoms in a Lattice

For lattice implementation we consider ^{23}Na and ^{87}Rb as the two species, in orthogonal triple-wells created by $\lambda = 600\text{ nm}$ and 800 nm along their active directions. With $D1, D2$ lines for ^{23}Na , $\simeq 589\text{ nm}$ and $D1 = 795\text{ nm}$, $D2 = 780\text{ nm}$ for ^{87}Rb , this ensures that each species is red-detuned by about 10 nm from its trapping frequency, but far off-resonant from that of the other. Since the species are held by separate lasers, the passive species will be naturally unaffected by the transfer cycle.

Transverse trapping for both species can be achieved with a laser at 1064 nm . We use the wavelength for the active species to set our length unit, and the recoil energy E_R as the energy unit ε . The effective transverse trap frequency is $\omega_{\perp} = (2\pi/\lambda)\sqrt{2V_{\perp}/m}$; and in these units the oscillator length $l_{\perp} = \sqrt{\hbar/(m\omega_{\perp})}$ and the confinement energy $2\hbar\omega_{\perp}$ are fixed by depth of the potential, which we take to be $V_{\perp} = 80\varepsilon$. The effective 1D interspecies interaction strength takes the form $g_{AB} = a/(\pi^2 l_{\perp A}^2)$, where scattering length $a = 103a_B$ for the ^{23}Na - ^{87}Rb [110]. Along the direction of the triple-wells, the well depths never exceed $V_z = 20\varepsilon$. The resulting estimates for our units and parameters are summarized in table 8.1.

Table 8.1: Units and parameters for lattice implementation with ^{87}Rb or ^{23}Na atoms.

Units and Parameters	^{87}Rb active	^{23}Na active
Length unit $l = \lambda$	800 nm	600 nm
Energy unit $\varepsilon = E_R = \hbar^2/(2m_A\lambda^2)$	$2.36 \times 10^{-30}\text{ J}$	$1.6 \times 10^{-30}\text{ J}$
Time unit $\tau = \hbar/\varepsilon$	$4.47 \times 10^{-5}\text{ s}$	$6.7 \times 10^{-6}\text{ s}$
Transverse trap freq. ω_{\perp}	$4.0 \times 10^5\text{ Hz}$	$2.7 \times 10^5\text{ Hz}$
Int. strength g_{AB}	$0.244\ \varepsilon \cdot l$	$0.325\ \varepsilon \cdot l$
Transverse Osc. Length l_{\perp}	$0.053\ l$	$0.053\ l$
Transverse energy $2\hbar\omega_{\perp}$	$36\ \varepsilon$	$36\ \varepsilon$
Int. energy g_{1D}/l_z	$3.24\ \varepsilon$	$4.3\ \varepsilon$

These estimates meet the main assumptions of our model and simulations:

1. The values of the interspecies interaction in our estimates are close to that used in our simulation $g_{1D} = 0.26 \varepsilon \cdot l$ with the units defined here.

2. The time scale for operation is about 11.9τ which corresponds to 0.53×10^{-3} s for active ^{23}Rb and 0.079×10^{-3} s for active ^{23}Na , implying sub-millisecond operation time scales, competitive with most proposals for quantum gates.

3. Effective 1D dynamics of the active species is justified: the transverse confinement energy $2\hbar\omega_{\perp} = 36 \varepsilon$ is much higher than the sum of the longitudinal kinetic energy $\sim \varepsilon$ and interaction energy $g_{AB}/l_z \simeq 4\varepsilon$. The latter is estimated by the product of the interaction strength and 1D particle density $\sim N/L \simeq 1/l_z$ with $N \sim 1$ since we consider single particle of each species; the extent of the density overlap of the particles during evolution is estimated by the effective *longitudinal* oscillator length $l_z = \sqrt{\hbar/(m_A\omega_z)}$ where $\omega_z = (2\pi/\lambda)\sqrt{2V_z/m_A}$ and we take $V_z = 20 \varepsilon$ as the upper limit of the longitudinal depth of the wells.

BECs in a Triple-well potential

In order to implement the proposed quantum gate with BECs, the triple well structure can be designed such that the two Gaussian barriers are felt only by the active species (A), possible by keeping their laser frequencies far off-resonant with respect to the passive species (B) which is therefore not affected by the variation of the barriers. In optical dipole traps, the self-interaction in the species A can be suppressed by Feshbach resonance.

To demonstrate feasibility, we choose ^7Li and ^{87}Rb as species A and B. Experiments [111] show ^7Li in $|F = 1, m_F = 1\rangle$ state has a very weak scattering length $a = -1 a_B$ at 560 G, changes sign and goes up to $a = 10 a_B$ at 630 G, implying zero scattering length at 566 G (by linear interpolation). The inter-species s-wave scattering length between ^7Li in $|F = 1, m_F = 1\rangle$ and ^{87}Rb in $|F = 1, m_F = 1\rangle$ has been computed [109] to be zero at 438 G and positive above that hitting resonance at 566 G (coincidentally). That coincidence means that the field cannot be at 566 G necessary for $a = 0$ for Lithium, but we can tune the interspecies scattering to about $a = +100 a_B$ at 560 G by being close but not quite at the resonance while having the species A scattering length of the order of $a = -1 a_B$, low enough to have negligible effect on the dynamics or eigenstates of species A.

We consider $N_A = N_B = 1000$ atoms, large enough to justify using mean field theory [112]. Both species are confined in a cigar-shaped optical dipole trap by the *same* laser of 1064 nm wavelength in the axial (direction of transport), but they experience different axial trap frequencies due to different detuning and masses. For species B, the axial (z) and transverse (\perp) trap frequencies are chosen to be $\omega_z^B = 2\pi \times 10$ Hz and $\omega_{\perp}^B = 2\pi \times 100$ Hz; and for species A $\omega_{\perp}^A = 2\pi \times 1000$ Hz, and its axial frequency is fixed by $\omega_z^A = \omega_z^B/\eta_z$ where $\eta_z = \sqrt{\frac{\delta_z^A}{\delta_z^B} \frac{m_z^A}{m_z^B}} = 0.36$, on using $\frac{\delta_z^A}{\delta_z^B} = 1.6$ for the ratio of detuning for the two species in the common axial field.

The tight transverse confinement implies a Gaussian shape transverse profile for both species : $\Phi_i(r_i, z_i) = \sqrt{2\beta_i}e^{-\beta_i r^2/2}\psi_i(z_i)$ with ($i = A, B$). Integrating out the transverse direction we get the coupled 1D Gross-Pitaevskii equations in Eq. (8.2). We define units based on the axial trap frequency ω_z^A for species A, shown in table 8.2, along with the resulting expressions for some of the relevant parameters like mean field interaction strengths g_{ij} . The mass ratios are denoted by $\mu_{AB} = m_{AB}/m_A$, $\mu_B = m_B/m_A$ with m_{AB} being the reduced mass of species A and B; and a_{ij} are the s-wave scattering lengths.

Following Ref. [112], we assume a Thomas-Fermi profile in the axial direction justified because of weak trapping: $\psi(z_B) = \sqrt{3/(4d_B^3)}\sqrt{d_B^2 - z_B^2}$, where $z_B \in [-d_B, d_B]$. We determine the values of the physical parameters, summarized in table 8.2, by minimizing with respect to parameters β_B and d_B the resulting energy functional corresponding to GP equation for species B.

$$\frac{E[\Phi_B]}{\eta_z N_B} = \left[\frac{1}{2\mu_B \eta_z} \left(\beta_B + \frac{(\mu_B \eta_z \gamma_B)^2}{\beta_B} \right) + \mu_B \eta_z \frac{d_B^2}{10} + \frac{1}{\mu_B \eta_z} \frac{3N_B a_{BB} \beta_B}{5d_B} \right] \quad (8.6)$$

where $\eta_z = \omega_z^B/\omega_z^A$ and $\gamma_B = \omega_\perp^B/\omega_z^B$.

Table 8.2: Units and parameters for two-species BEC in triple-well.

Units and Parameters	Numerical Values
Energy unit $\varepsilon = \hbar\omega_z^A$	1.8×10^{-32} J
Length unit $l = \sqrt{\frac{\hbar}{m_A \omega_z^A}}$	7.2×10^{-6} m
Time unit $\tau = (\omega_z^A)^{-1}$	5.7×10^{-3} s
Transverse size of B is $l_\perp^B = \sqrt{1/\beta_B}$	$\beta_B = 35.85 \simeq 36 \Rightarrow l_\perp^B = 0.17 l$
Transverse size of A is $l_\perp^A = \sqrt{1/\beta_A}$	$\beta_A = 35.97 \simeq 36 \Rightarrow l_\perp^A = 0.17 l$
Longitudinal size of B	$d_B = 1.58 l$
Longitudinal size of A	$l_z^A = 1 l$ (by choice of units)
Chemical-potential of B	5.7ε (less than $2\hbar\omega_\perp^B = 7.2 \varepsilon$)
Self-interaction strength of B	$g_{BB} = \frac{2a_{BB}N_B\beta_B}{\mu_B} = 4.2 \varepsilon \cdot l$
Cross-interaction strength for A	$g_{AB} = \frac{a_{AB}N_B\beta_B}{\mu_{AB}} = 28.6 \simeq 29\varepsilon \cdot l$
Cross-interaction strength for B	$g_{BA} = \frac{a_{AB}N_A\beta_A}{\mu_{AB}} = 28.7 \simeq 29\varepsilon \cdot l$

Notably, we decoupled the energy functional by neglecting the inter-species interaction assuming it to be small relative to its self-interaction for species B. But as we see from table 8.2, it is quite the opposite. Likewise the cross-interaction for species A is two orders of magnitude higher than is assumed in our simulations. This can be rectified by adding a novel design feature that creates a slight transverse offset of the longitudinal axes to reduce the overlap of the two species. Since

the radial profiles are seen to be identical for the two species $\beta_A \simeq \beta_B \simeq 36 = \beta$, the geometric factor due to the reduced overlap is given by the integral:

$$\mathcal{I} = \int_{-\infty}^{\infty} dy e^{-\beta y^2} \times \left[\int_{-\infty}^{b/2} dx e^{-\beta(x-b)^2} + \int_{b/2}^{\infty} dx e^{-\beta x^2} \right] = \frac{\pi}{\beta} \text{Erfc}[b\sqrt{\beta}/2] \quad (8.7)$$

which is an Error-Function and where the line of intersection of the surfaces is found by setting $x^2 = (x - b)^2 \Rightarrow 2x = b$ for positive offset b . Using the inter-species interaction strength of $29\varepsilon \cdot l$ for full overlap we solve $29 \times \mathcal{I}(b) = 0.5$ to find that a small offset of $b = 0.30l$ reduces that interaction strength to $0.5\varepsilon \cdot l$ as used in our simulations.

We summarize how these estimates satisfy the assumptions of our model:

1. Our use of $g_{1D} = 0.5\varepsilon \cdot l$ for the inter-species interaction can be realized by a small transverse offset of the two species.

2. Even though the species B does not ‘see’ the Gaussian barriers creating the triple well, its extent in the dynamical direction is $2d_B \simeq 3l$, localized within the size $2d \simeq 4l$ of the central well measured as the separation between the peaks of the barriers.

3. The dynamics in the active direction is effectively 1D since the chemical potential of even species B (which has self-interaction) is 5.69ε which is less than the energy required for exciting the first transverse excited state 7.2ε .

4. During evolution of species A, species B remains well-localized since it does not feel the time-varying potential and its overlap and interaction with species A remains relatively small.

8.5 Fidelity and noise

We obtained gate fidelities of 98% for both static and dynamic potentials, computed as the probability of finding atom A in a localised Gaussian state. The main source of infidelity was projection on $\phi_{i>3}$ of the initial Gaussian for the static case and residual non-adiabatic coupling to $\phi_{i>3}$ for the dynamic case.

The primary noise sources are fluctuations of the potentials, and of T and V_{AB} . High frequency fluctuations $>\text{kHz}$ cause heating with negligible impact ($\sim 10^{-4}$ change in fidelity) in the lattice where the cycle time $\sim 10^{-4}\text{ s} \ll 10\text{ s}$ durations of stable trapping of single atoms [113]. Heating effects are more significant for BECs with cycle time $\sim 0.25\text{ s}$, but long lifetimes $\geq 10\text{ s}$ can compensate for that [114]. In the lattice, due to fast cycle time, low frequency noise $\leq 100\text{ Hz}$ can be treated as static deviations of the physical parameters. Given that our mechanism is an interference effect of the lowest three eigenstates, its fidelity goes as $\sin^2 \Delta\theta$, where $\Delta\theta$ is the eigenstate phase difference, which depends linearly on potential variations. Thus, for small fluctuations, the infidelity $\simeq \Delta\theta^2$ implying a *quadratic* dependence on fluctuations of the physical parameters. The combined impact of 0.1% variations in potential parameters leads to a fidelity loss of about 3×10^{-4} .

Snapshots of gate operation shown in Fig. 8.4 confirm that: (i) species B remains localized unaffected by the evolution of species A, (ii) species A is delocalized during transit (iii) dynamics with Eq. (8.1) and Eq. (8.2) is indistinguishable on plot-scale.

After a gate cycle, the reduced density matrix $\rho_A(t) = \text{Tr}_B |\psi_{AB}(t)\rangle\langle\psi_{AB}(t)|$, gives $1 - \text{Tr}\rho_A^2(T) = 4.4 \times 10^{-4}$, indicating a pure state. The von Neumann entropy $S(T) = -\text{Tr}[\rho_A(T) \ln(\rho_A(T))] = 2.3 \times 10^{-3}$, with $S(t) < 4.0 \times 10^{-3}$ during the cycle for the dynamic potential and $S(t) < 12 \times 10^{-3}$ for the static. These justify the factorization of $|\psi_{AB}\rangle$ and show the absence of significant entanglement between the species. The gate fidelity can be arbitrarily improved to limits $\sim 99.97\%$ set by noise, by using optimal control methods [115], since the mechanism has well-defined initial and target states and a highly optimal initial path. This design can implement a universal set of gates, since single qubit gates, like a Hadamard gate, can be implemented by adjusting ΔE_1 , with species B absent, for desired partial transfer in a cycle.

Hilbert space geometry and the quantum speed limit

In this chapter, we investigate the optimality of time limited dynamics within the framework of Hilbert space geometry, where the time evolution is represented as a trajectory and the optimized quantity is the final distance from some target state. After introducing the basic geometrical concepts in Hilbert space, we derive a simple optimization procedure equivalent to the standard optimum control (OC) algorithms. We then examine the effect of independent local time variations, yielding a quantitative measure of process optimality, which allows to assess the convergence of OC algorithms.

We express the exact time fidelity trade-off in an integral form and argue for its broad applicability in the estimation of T_{QSL} . This result can also be employed in reaching a desired fidelity in a minimal time below T_{QSL} . Finally, we show the existence of multiple locally optimal solutions in a system with a constrained Hamiltonian, and verify the validity of the analytical results numerically.

9.1 Hilbert space geometry

Consider a system characterized by a state vector $|\psi\rangle \equiv |\psi(t)\rangle$ evolving in time via the Schrödinger equation $|\dot{\psi}\rangle = -i\hat{H}|\psi\rangle$, where \hat{H} is the time dependent Hamiltonian of the system and $\hbar = 1$.

The time derivative of the state can be interpreted as the *velocity in the Hilbert space*. Generally, the *parallel Hilbert velocity* defined by

$$|\dot{\psi}_{\parallel}\rangle \equiv |\psi\rangle\langle\psi|\dot{\psi}\rangle = -i|\psi\rangle\langle\psi|\hat{H}|\psi\rangle \equiv -iE|\psi\rangle, \quad (9.1)$$

merely evolves the phase of the current state, while the *perpendicular Hilbert velocity*

$$|\dot{\psi}_\perp\rangle \equiv |\dot{\psi}\rangle - |\dot{\psi}_\parallel\rangle, \quad (9.2)$$

$$|\dot{\psi}_\perp| \equiv \sqrt{\langle\dot{\psi}_\perp|\dot{\psi}_\perp\rangle} = \sqrt{|\dot{\psi}|^2 - |\dot{\psi}_\parallel|^2} = \sqrt{\langle\hat{H}^2\rangle - \langle\hat{H}\rangle^2} \equiv \Delta E, \quad (9.3)$$

induces motion in the Hilbert space.

This can be seen explicitly by decomposing the state in a fixed orthonormal basis $|\phi_j\rangle$,

$$|\psi\rangle = \sum_j a_j e^{-ib_j} |\phi_j\rangle, \quad (9.4)$$

where $\mathbf{a} \equiv (a_1, a_2, \dots)$ and $\mathbf{b} \equiv (b_1, b_2, \dots)$ are real vectors, and $|\mathbf{a}|^2 = \sum_j a_j^2 = 1$. The Hilbert velocity is

$$|\dot{\psi}\rangle = \sum_j (\dot{a}_j - ia_j \dot{b}_j) e^{-ib_j} |\phi_j\rangle. \quad (9.5)$$

At a given instant, the particular choice of basis $|\phi_1\rangle = |\psi\rangle$ ensures $a_k = 0$ for $k > 1$ and $\dot{a}_1 = 0$ (since $\frac{d}{dt}|\mathbf{a}| = 0$). Thus, a non-zero perpendicular Hilbert velocity component

$$\langle\phi_k|\dot{\psi}\rangle = \sum_j (\dot{a}_j - ia_j \dot{b}_j) e^{-ib_j} \langle\phi_k|\phi_j\rangle = \dot{a}_k e^{-ib_k} \quad (9.6)$$

implies a time variation of the coefficient a_k leading to motion in Hilbert space.

In a general basis, one finds that $|\dot{\psi}|^2 = |\dot{\mathbf{a}}|^2 + \langle\dot{b}^2\rangle$ and $|\dot{\psi}_\parallel| = \langle\dot{b}\rangle$, where the notation $\langle c \rangle \equiv \sum_j a_j^2 c_j$ was used. The speed of motion can then be expressed as $|\dot{\psi}_\perp| = \sqrt{|\dot{\mathbf{a}}|^2 + (\Delta\dot{b})^2}$, where $\Delta\dot{b} \equiv \sqrt{\langle\dot{b}^2\rangle - \langle\dot{b}\rangle^2}$. The *trajectory length* can be defined for any $|\psi(t)\rangle$, $t \in \langle 0, T \rangle$ as

$$\mathcal{C} \equiv \int_0^T |\dot{\psi}_\perp| dt = \int_0^T \Delta E(t) dt, \quad (9.7)$$

which is the Aharonov-Anandan geometrical distance [98].

The distance in Hilbert space $\mathcal{D}(\alpha, \beta)$ between states $|\alpha\rangle$ and $|\beta\rangle$ is the length of the shortest trajectory connecting them. The functional (9.7) attains an extremal value when its integrand fulfills the Euler-Lagrange equations. Since $|\dot{\psi}_\perp|(\dot{\mathbf{a}}, \mathbf{a}, \dot{\mathbf{b}})$ does not depend on \mathbf{b} , the generalized momenta

$$\Pi_j \equiv \frac{\partial |\dot{\psi}_\perp|}{\partial \dot{b}_j} = \frac{(\dot{b}_j - \langle\dot{b}\rangle) a_j^2}{|\dot{\psi}_\perp|} = \text{const.} \quad (9.8)$$

are conserved. Without loss of generality, we can choose $|\phi_1\rangle = |\alpha\rangle$ in the state expansion implying $a_1(t=0) = 1$ and $\Pi_j = 0$ for all j . At any later time, non-zero a_j requires $\dot{b}_j = \langle\dot{b}\rangle$ and consequently $\Delta\dot{b} = 0$. In this case, $|\dot{\psi}_\perp| = |\dot{\mathbf{a}}|$ for all

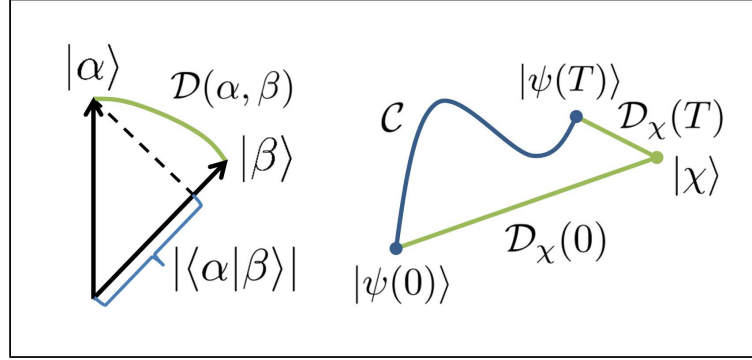


Figure 9.1: Schematic illustration of the distance of states from equation (9.9) and the distance inequality (9.20).

times, and the shortest trajectory is a geodesic on a hypersphere in the space of parameter \mathbf{a} defined by $|\mathbf{a}| = 1$. Identifying $|\beta\rangle$ with $|\psi(T)\rangle$, in the chosen basis $a_1(T) = |\langle\phi_1|\psi(T)\rangle| = |\langle\alpha|\beta\rangle|$. Thus the distance of states is

$$\mathcal{D}(\alpha, \beta) = \arccos(|\langle\alpha|\beta\rangle|), \quad (9.9)$$

which is equivalent to the Wootters distance [116, 117, 118], and attains a maximum value $\pi/2$ for a pair of orthogonal states, see Fig. 9.1. Since $\mathcal{C} \geq \mathcal{D}$, we arrive at the integral form of the QSL inequality

$$\int_0^T \Delta E dt \geq \arccos(|\langle\psi(T)|\psi(0)\rangle|). \quad (9.10)$$

For a constant ΔE we recover the Bhattacharyya bound

$$\Delta E \times T \geq \arccos(|\langle\psi(T)|\psi(0)\rangle|). \quad (9.11)$$

9.2 Relative motion

In general, optimum control algorithms aim to drive the system into a certain predefined state by dynamically varying its Hamiltonian. It is thus of special interest to evaluate the relative motion in the subspace spanned by the current state $|\psi\rangle$ and some fixed target state $|\chi\rangle$. Let $|\nu\rangle$ be another fixed state forming an orthonormal basis with $|\chi\rangle$ in this subspace at a given instant. The current state can then be expressed as

$$|\psi\rangle = a_1 e^{-ib_1} |\chi\rangle + a_2 e^{-ib_2} |\nu\rangle, \quad (9.12)$$

and the motion in the subspace is induced by a component of the perpendicular Hilbert velocity along a state

$$|\xi\rangle = a_2 e^{-ib_1} |\chi\rangle - a_1 e^{-ib_2} |\nu\rangle \quad (9.13)$$

(orthogonal to $|\psi\rangle$, determined up to a phase). Defining the fidelity $F \equiv |\langle\chi|\psi\rangle|^2 = \cos^2[\mathcal{D}(\chi, \psi)]$, we can obtain this state from

$$|\xi\rangle = \frac{|\chi\rangle\langle\chi| - F}{\sqrt{F(1-F)}}|\psi\rangle. \quad (9.14)$$

The states $|\psi\rangle$ and $|\xi\rangle$ also form an orthonormal basis in the subspace, hence

$$|\chi\rangle = e^{ib_1}(a_1|\psi\rangle + a_2|\xi\rangle), \quad (9.15)$$

implying that $|\xi\rangle$ represents the part of $|\chi\rangle$ which is not present in $|\psi\rangle$.

Using the expansion for Hilbert velocity from Eq. (9.5) with $|\phi_1\rangle = |\chi\rangle$ and $|\phi_2\rangle = |\nu\rangle$, we can express the perpendicular Hilbert velocity in the subspace as

$$|\dot{\psi}_{\perp,\chi}\rangle \equiv |\xi\rangle\langle\xi|\dot{\psi}\rangle = |\xi\rangle\left[\frac{\dot{a}_1}{a_2} + i(\dot{b}_2 - \dot{b}_1)a_1a_2\right], \quad (9.16)$$

where we have also used Eq. (9.13) and the normalization condition $a_1^2 + a_2^2 = 1$. Denoting the immediate distance from $|\chi\rangle$ as $\mathcal{D}_\chi(t) \equiv \mathcal{D}(\chi, \psi(t)) = \arccos(a_1)$, we see that the real part of $\langle\xi|\dot{\psi}\rangle$ corresponds to the direct motion towards the state $|\chi\rangle$

$$\dot{\mathcal{D}}_\chi(t) = \frac{d}{dt} \arccos(a_1) = -\frac{\dot{a}_1}{a_2} = -\text{Re}\langle\xi|\dot{\psi}\rangle. \quad (9.17)$$

On a Bloch sphere with $|\chi\rangle$ and $|\nu\rangle$ on the poles this corresponds to a motion along a meridian. Similarly, the imaginary part

$$|\text{Im}\langle\xi|\dot{\psi}\rangle| = |(\dot{b}_2 - \dot{b}_1)a_1a_2| = \sqrt{\langle\dot{b}^2\rangle - \langle\dot{b}\rangle^2} \equiv \Delta\dot{b} \quad (9.18)$$

represents a motion along the parallels on the sphere preserving the distance from the poles.

When $|\chi\rangle$ is orthogonal to $|\psi\rangle$, we have $a_1 = 0$ and $|\xi\rangle = e^{-ib_1}|\chi\rangle$, with an arbitrary phase b_1 . The imaginary part of $\langle\xi|\dot{\psi}\rangle$ becomes zero due to vanishing frequency uncertainty $\Delta\dot{b} = 0$ and the direct velocity towards $|\chi\rangle$ becomes $\dot{\mathcal{D}}_\chi(t) = -|\langle\chi|\dot{\psi}\rangle|$.

For a general trajectory $|\psi(t)\rangle$, where $t \in \langle 0, T \rangle$, we can obtain the distance of its end point from the target by integrating Eq. (9.17)

$$\mathcal{D}_\chi(T) = \mathcal{D}_\chi(0) - \int_0^T \text{Re}\langle\xi(t)|\dot{\psi}\rangle dt, \quad (9.19)$$

where the time dependence of $|\xi\rangle$ was shown explicitly. Since $\langle\xi|\dot{\psi}\rangle$ is only one component of the transverse Hilbert velocity, it directly follows

$$\mathcal{D}_\chi(T) \geq \mathcal{D}_\chi(0) - \int_0^T \Delta E dt, \quad (9.20)$$

which can also be seen by realizing that the hypothetical trajectory $\mathcal{C} + \mathcal{D}_\chi(T)$ connecting $|\psi(0)\rangle$ and $|\chi\rangle$ is necessarily longer or equal to the distance of the two states $\mathcal{D}_\chi(0)$, see Fig. 9.1. The above expression sets a limit on how quickly a target state can be approached as opposed to Eq. (9.10), which sets a limit on how quickly a system can leave an initial state.

9.3 Optimal navigation

Just like it often pays off to take a slightly longer path to avoid an obstacle on the way to our goal, it may not be optimal to maximize the direct Hilbert velocity towards the target at all times. Taking a longer path at higher speed may produce a better result. What is important is the final proximity to the target achieved in the specified time, rather than the actual traveled distance.

In the following we will consider a case when the Hamiltonian of the system depends on time via a vector of control parameters $\mathbf{u}(t)$, that is $\hat{H} \equiv \hat{H}(\mathbf{u}(t))$. Suppose the initial state $|\psi(0)\rangle$ is fixed and we have some guess for the control $\mathbf{u}(t)$, $t \in (0, T)$. To obtain the final distance from the target $\mathcal{D}_\chi(T)$, we first need to calculate the full time evolution of the initial state. How will $\mathcal{D}_\chi(T)$ change when we arbitrarily alter the control on some short time interval within the process?

Thanks to unitarity of the quantum time evolution we do not have to calculate the whole trajectory again: For any two trajectories $|\psi_1(t)\rangle$ and $|\psi_2(t)\rangle$ governed by the same Hamiltonian and having generally different starting points $|\psi_1(0)\rangle$ and $|\psi_2(0)\rangle$, the immediate distance $\mathcal{D}(\psi_1(t), \psi_2(t))$ is preserved for all times t . This follows from the time invariance of the scalar product

$$\begin{aligned} \frac{d}{dt} \langle \psi_1 | \psi_2 \rangle &= \langle \dot{\psi}_1 | \psi_2 \rangle + \langle \psi_1 | \dot{\psi}_2 \rangle \\ &= i \langle \psi_1 | \hat{H} | \psi_2 \rangle - i \langle \psi_1 | \hat{H} | \psi_2 \rangle = 0. \end{aligned} \quad (9.21)$$

For convenience of notation we will rename the target state $\chi \rightarrow \chi(T)$ and denote its backwards evolved trajectory as $|\chi(t)\rangle$. The final distance from the target is then equal to the immediate distance of the trajectories $|\psi(t)\rangle$ and $|\chi(t)\rangle$

$$\mathcal{D}_\chi(T) \equiv \mathcal{D}(\chi(T), \psi(T)) = \mathcal{D}(\chi(t), \psi(t)) \quad (9.22)$$

for any point in time. Utilizing the result (9.19) for infinitesimal integration boundaries $\langle t - dt, t \rangle$, we can write

$$\mathcal{D}_\chi(T) = \mathcal{D}(\chi(t), \psi(t - dt)) - Q(t)dt, \quad (9.23)$$

where we have introduced a new notation for the *direct Hilbert velocity*

$$Q(t) \equiv \text{Re} \langle \xi(t) | \dot{\psi} \rangle = \text{Im} \langle \xi(t) | \hat{H}(t) | \psi(t) \rangle. \quad (9.24)$$

Note that the state $|\xi(t)\rangle$ is now computed with respect to the backwards evolved target state $|\chi(t)\rangle$. As before, the direct Hilbert velocity is bounded from above by

$$Q \equiv \text{Re}\langle\xi|\dot{\psi}\rangle = \text{Re}\langle\xi|\dot{\psi}_\perp\rangle \leq |\dot{\psi}_\perp| = \Delta E. \quad (9.25)$$

The equality occurs when the motion in the Hilbert space is along a geodesic towards $|\chi(t)\rangle$.

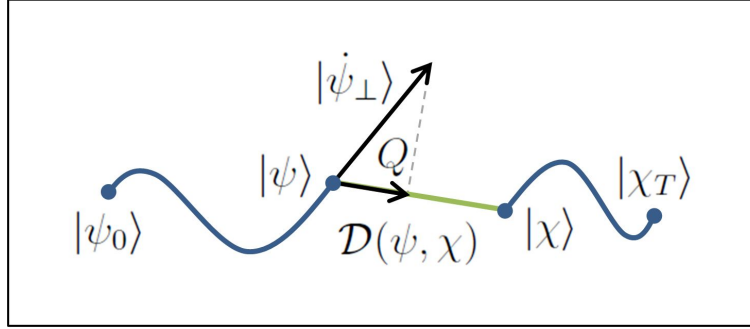


Figure 9.2: Schematic interpretation of the direct Hilbert velocity Q as a component of the perpendicular Hilbert velocity $|\dot{\psi}_\perp\rangle$ which corresponds to the shortening rate of the distance $\mathcal{D}(\psi, \chi)$, see Eq. (9.23). We have omitted the explicit time dependence of the forward evolved initial state $|\psi\rangle \equiv |\psi(t)\rangle$, as well as the backwards evolved target state $|\chi\rangle \equiv |\chi(t)\rangle$. Subscripts on ψ and χ denote points in time.

Equation (9.23) shows that in order to minimize the final distance from the target, we have to maximize the direct Hilbert velocity $Q(t)$ at each point in time. The simplest local optimization algorithm can vary the control proportionally to the gradient of $Q(t)$

$$\delta \mathbf{u}(t) = \alpha \cdot \frac{\partial Q(t)}{\partial \mathbf{u}} = \alpha \cdot \text{Im} \left\langle \xi(t) \left| \frac{\partial \hat{H}}{\partial \mathbf{u}} \right| \psi(t) \right\rangle, \quad (9.26)$$

with some step size α . An improved convergence can be achieved by employing higher derivatives with respect to the control [119]. Once the control has been altered on some finite time interval, one can update the time evolution of $|\psi(t)\rangle$ and $|\chi(t)\rangle$ on that interval and proceed by optimizing a neighboring interval (preceding or following in time) [120]. One iteration of the algorithm would then be understood as a sweep over the whole process duration.

Such an optimization is in fact equivalent to the Krotov algorithm [115, 121] which follows from the Pontryagin maximum principle [122, 95] as well as alternative approaches [123, 124]. In the Krotov algorithm the optimized quantity is fidelity and the improvement of the control is found by maximization of the Pontryagin Hamiltonian $\mathcal{H}(t, \psi, \mathbf{u}, \chi) \equiv 2\text{Im} [\langle \chi | \hat{H} | \psi \rangle \langle \psi | \chi \rangle]$. Inserting for $|\chi\rangle$ from

Eq. (9.15), we see that this function is in fact proportional to the direct Hilbert velocity

$$\mathcal{H}(t, \psi, \mathbf{u}, \chi) = 2\sqrt{F(1-F)} \times Q(t). \quad (9.27)$$

Thus our result provides an interpretation of optimum control theory in terms of Hilbert space geometry. As shown below it also offers an intuitive framework for the understanding of time optimization.

9.4 Time fidelity trade-off

We now turn to the question of trade-off between the duration of the process and the achievable proximity of the target state. To our knowledge, this problem has only been studied for uniform extensions of the process [101, 105, 102, 103, 106, 104]. In the following we consider a more general case of non-uniform time variations.

Assume the process can be divided into N small but finite time intervals Δt_j , connected at points in time $t_j = \sum_{k=1}^j \Delta t_k$. At each interval the Hamiltonian is constant and determined uniquely by the value of the control parameter \mathbf{u}_j , thus the set $\{\mathbf{u}_j, \Delta t_j; j = 1, 2, \dots, N\}$, together with the initial condition for $|\psi(0)\rangle$, completely defines the process.

When treating Δt_j as independent parameters, the process duration T is also allowed to vary, however both $|\psi(0)\rangle$ and $|\chi(T)\rangle$ remain fixed. A general variation of the time intervals can be written in the form $\delta\Delta t_j = \mu_j\Delta t_j$, where all $|\mu_j| \ll 1$. To the first order in Δt_j we can approximate Eq. (9.23) as

$$\mathcal{D}_\chi(T) \approx \mathcal{D}(\chi(t_j), \psi(t_{j-1})) - Q_j\Delta t_j, \quad (9.28)$$

with $Q_j \equiv Q(t_j)$. The induced variations of T and $\mathcal{D}_\chi(T)$ then are

$$\delta T = \sum_{j=1}^N \delta\Delta t_j = \sum_{j=1}^N \mu_j\Delta t_j = T \langle \mu \rangle_T, \quad (9.29)$$

$$\delta\mathcal{D}_\chi(T) = \sum_{j=1}^N \frac{\partial\mathcal{D}_\chi(T)}{\partial\Delta t_j} \delta\Delta t_j = -T \langle Q\mu \rangle_T, \quad (9.30)$$

where we have defined the time average

$$\langle f \rangle_T \equiv \frac{1}{T} \sum_{j=1}^N f_j\Delta t_j \rightarrow \frac{1}{T} \int_0^T f(t)dt. \quad (9.31)$$

For the case of an *uncorrelated adjustment* μ_j , fulfilling

$$\text{Cov}(Q, \mu) \equiv \langle Q\mu \rangle_T - \langle Q \rangle_T \langle \mu \rangle_T = 0, \quad (9.32)$$

the variation of the distance is simply

$$\delta\mathcal{D}_\chi(T) = -\langle Q \rangle_T \delta T. \quad (9.33)$$

A trivial example fulfilling condition (9.32) is a uniform extension of the process $\delta\Delta t_j = \kappa\Delta t_j$, with a small constant $\kappa = \delta T/T$. This case was considered among others by Mishima *et al.* [105] arriving at an equivalent time fidelity trade-off, which in our notation can be expressed as

$$\frac{dF}{dT} = \frac{1}{T} \int_0^T 2\text{Im} [\langle \chi | \hat{H} | \psi \rangle \langle \psi | \chi \rangle] dt \quad (9.34)$$

$$= 2\sqrt{F(1-F)} \times \langle Q \rangle_T, \quad (9.35)$$

where the $|\chi\rangle$ decomposition (9.15) was utilized.

Let us now consider a generally non-uniform adjustment of the time intervals which preserves the total duration T . Such a redistribution must be of the form $\mu_j = \epsilon[\nu_j - \langle \nu \rangle_T]$, where $\nu_j \equiv \nu(t_j)$ is an arbitrary function of time, and ϵ is a small scaling factor. Using Eq. (9.30), the corresponding change in the distance is

$$\delta\mathcal{D}_\chi^\epsilon(T) = -\epsilon T \text{Cov}(Q, \nu), \quad (9.36)$$

which is extremal for $\nu_j = Q_j$. Comparing this with the distance variation $\delta\mathcal{D}_\chi^\kappa(T)$ induced by a uniform extension of the process with an equivalent mean adjustment

$$\kappa = \sqrt{\langle \mu^2 \rangle_T} = \epsilon \sqrt{\langle (Q - \langle Q \rangle_T)^2 \rangle_T} \equiv \epsilon \text{Std}(Q), \quad (9.37)$$

we obtain a measure of the process optimality

$$\sigma_Q \equiv \frac{\delta\mathcal{D}_\chi^\epsilon(T)}{\delta\mathcal{D}_\chi^\kappa(T)} = \frac{\text{Cov}(Q, Q)}{\text{Std}(Q) \langle Q \rangle_T} = \frac{\text{Std}(Q)}{\langle Q \rangle_T}. \quad (9.38)$$

For a sufficiently fine discretization of time, any process optimal with respect to \mathbf{u}_j is necessarily extremal with respect to any variation of Δt_j which preserves T , implying $\delta\mathcal{D}_\chi^\epsilon(T) \rightarrow 0$. Thus $\sigma_Q \rightarrow 0$ is a necessary criterion for process optimality, and can be used for quantifying the convergence of OC algorithms. Additionally $\sigma_Q = 0$ implies $Q(t) = \langle Q \rangle_T$ for all points in time, which via $\text{Cov}(Q, \mu) = 0$ guarantees validity of Eq. (9.33) for any time adjustment μ_j of an optimal process.

For further discussion it is useful to introduce a classification scheme of the control sequences based on their optimality. Since the optimizing algorithm searches for local optima, the optimization result can depend on the initial choice of the control $\mathbf{u}(t)$. We define an *optimum class* as a continuous T transformation of *optimal* control parameters $\mathbf{u}_{\text{opt}}(T, t) \equiv \mathbf{u}_{\text{opt}, T}(t)$. A set of initial control parameters yielding upon optimization a solution in a certain optimum class will be called a *control family*.

If we denote the direct Hilbert velocity within an optimum class by $Q_{\text{opt}}(T)$, we can write the time distance trade-off (9.33) in an integral form

$$\mathcal{D}_x(T_2) = \mathcal{D}_x(T_1) - \int_{T_1}^{T_2} Q_{\text{opt}}(T) dT. \quad (9.39)$$

For an optimum class extending from zero to some finite duration T , the above equation quantifies the speed limit exactly as opposed to Eq. (9.20), which merely provides a lower bound. In terms of fidelity the above can be written as

$$\left[\arcsin(\sqrt{F}) \right]_{F_1}^{F_2} = \int_{T_1}^{T_2} Q_{\text{opt}}(T) dT. \quad (9.40)$$

Usually the convergence of OC algorithms becomes slower as T approaches the quantum speed limit T_{QSL} from below. Interestingly for many systems $Q_{\text{opt}}(T)$ is constant or a slowly varying function of T in that regime. The value of T_{QSL} can thus be predicted well even for moderate values of fidelity ($F \approx 0.9$, $T < T_{\text{QSL}}$) by approximating the integrand in Eq. (9.40) with a constant. Note that Eq. (9.34) is not very suitable for linear extrapolation of the fidelity, since the right hand side varies quickly when $F \rightarrow 1$ and thus cannot be approximated with a constant.

Caneva *et al.* [103] observed the relation $F = \sin^2\left(\frac{\pi}{2}T/T_{\text{QSL}}\right)$ arising from a numerical optimization of multiple physical systems, and attributed this behavior to the motion along geodesics in Hilbert space. In general, Eq. (9.40) implies $F = \sin^2\left(\int_0^T Q_{\text{opt}}(T') dT'\right)$ for an optimum class with $F(T=0) = 0$. The \sin^2 dependence thus occurs whenever $Q_{\text{opt}}(T)$ is independent of T , even if the motion is not along a geodesic. Unit fidelity is then reached in time $T_{\text{QSL}} = \pi/(2Q_{\text{opt}})$.

Equation (9.40) also allows an OC algorithm to search for a process yielding a certain predefined fidelity while having the shortest possible duration within a given control family. After the default OC algorithm has converged to some fidelity F_1 for a given initial duration T_1 , we can estimate the time T_2 required to obtain fidelity F_2 by setting $Q_{\text{opt}}(T)$ constant in Eq. (9.40), that is

$$T_2 = T_1 + \left[\arcsin(\sqrt{F}) \right]_{F_1}^{F_2} / Q_{\text{opt}}(T_1). \quad (9.41)$$

Re-optimizing the process with uniformly extended control to $T = T_2$ and repeating the estimate of T_2 converges upon the process with the desired fidelity F_2 in few iterations. When $Q_{\text{opt}}(T)$ is a varying function, we can improve the convergence by employing its derivatives in the expansion of the integrand in Eq. (9.40).

9.5 Entanglement generation in a multilevel system

To provide a non-trivial example of our time optimal control, we optimize entanglement generation in an atomic system with Rydberg excitation blockade [125].

The system consists of N indistinguishable atoms, each having two ground states $|1\rangle$ and $|2\rangle$, and a highly excited Rydberg state $|r\rangle$. The ground states are coupled by a resonant external field with a Rabi frequency $\Omega_1(t) = \Omega_{\max}u_1(t)$, and similarly the states $|2\rangle$ and $|r\rangle$ are coupled by $\Omega_r(t) = \Omega_{\max}u_r(t)$, with the control parameters limited by $0 \leq u_i \leq 1$ and $\Omega_{\max} = 2\pi \times 10\text{MHz}$. Due to a large electric dipole moment, a single Rydberg excitation will render Ω_r off-resonant for the remaining atoms, thus permitting only one Rydberg excitation at a time. Consequently, the system is closed in the $2N + 1$ dimensional Hilbert space with a symmetric basis $|n_1, n_2, n_r\rangle$, where n_i is the number of atoms in the state $|i\rangle$, and $n_1 + n_2 + n_r = N$, $n_r \leq 1$. The Hamiltonian is $H = H_{J_x} + H_{\text{JC}}$ with

$$H_{J_x}(t) \equiv \Omega_1(t)J_x = \Omega_1(t)\frac{1}{2}(a_1^\dagger a_2 + a_1 a_2^\dagger), \quad (9.42)$$

$$H_{\text{JC}}(t) \equiv \Omega_r(t)\frac{1}{2}(a_2^\dagger \sigma^- + a_2 \sigma^+), \quad (9.43)$$

where a_i (a_i^\dagger) are the conventional annihilation (creation) operators, J_x is the pseudo-spin operator and σ^\pm are the Pauli matrices denoting the transfer between the states with 0 and 1 Rydberg excitation.

Initially the system is prepared in $|\psi(0)\rangle = |N, 0, 0\rangle$. Motivated by Ref. [125], we aim to prepare the maximally entangled state

$$|\chi(T)\rangle = \begin{cases} |J_x = 0\rangle & \text{if } N \text{ is even} \\ (|J_x = 0\rangle \otimes |r\rangle)_{\text{sym}} & \text{if } N \text{ is odd} \end{cases}, \quad (9.44)$$

where $(\cdot)_{\text{sym}}$ denotes symmetrization with respect to all atoms. To have a simple but non-trivial system with $\langle\psi(0)|\chi(T)\rangle = 0$, we have chosen $N = 3$.

To classify the control sequences as outlined above, we initially choose constant control parameters $u_1(t) = u_r(t) = 1$ and evolve the states ψ and χ in time (forward and backward respectively) for a variable total duration T . The resulting fidelities $F(T)$ and the values of $\langle Q \rangle_T$ are shown in Fig.9.3(a,b). Note that Q does not depend on t since H is constant and thus commutes with the evolution operator. The examined range of T is divided into several sections by discontinuities in $Q(T)$ where $F \rightarrow 0$ and $Q(T)$ changes sign.

To identify the associated control families we perform control optimization for initial parameters u_i chosen from each of these sections. Once the control has been optimized, an element in the optimum class is found and the whole class can be mapped out by allowing the process duration to vary through Eq. (9.41), where the target fidelity is adjusted in small steps. Different initial conditions converging into the same optimum class then belong to the same control family. The division of our initial controls into control families is denoted by roman numbering $i - vi$. Note that initial control parameters from different sections can belong to the same control family as illustrated by family *iii*. Moreover the transition to a different control family can occur at non-zero fidelity, illustrated by family *v*.

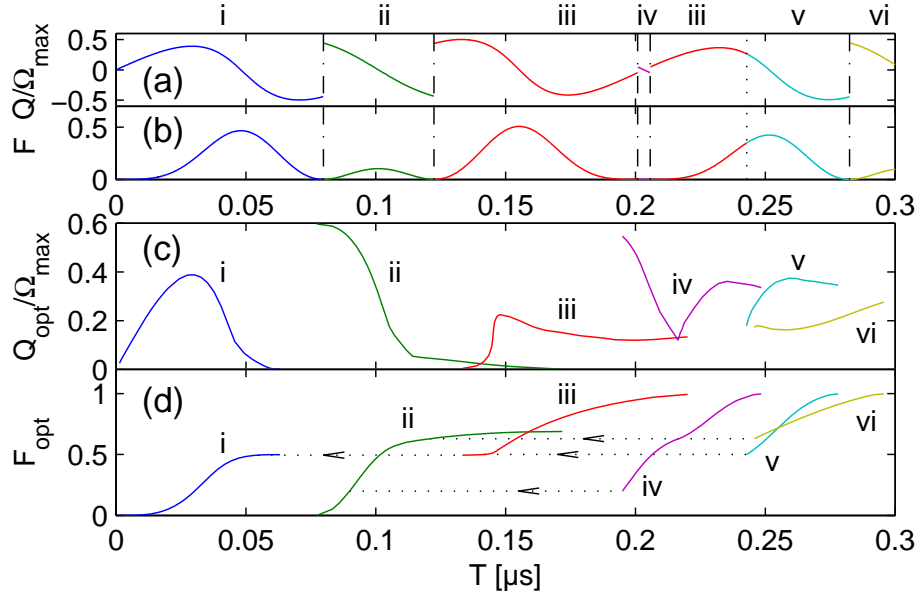


Figure 9.3: (a,b) The evolution of the direct Hilbert speed Q and fidelity F are shown for constant control $u_1(t) = u_r(t) = 1$ as a function of the process duration T . Note the discontinuities in $Q(T)$ separating the control families $i - vi$. (c,d) The values of Q and F for the optimum solutions (classes) are shown as a function of the process duration T . The horizontal dotted lines in (d) represent the slip transitions (see text).

Figure 9.3(c,d) shows the fidelity $F_{\text{opt}}(T)$ and $Q_{\text{opt}}(T)$ for the six optimum classes. Each class is shown within the relevant region in T where $0 < F < 1$ and $Q_{\text{opt}}(T) > 0$. The first two classes do not reach $F = 1$, because the OC algorithm fails to improve when $Q_{\text{opt}}(T) \rightarrow 0$. Interestingly, the remaining optimal classes slip into a lower class before reaching $F = 0$ (denoted by vertical dotted lines in Fig.9.3(d)).

These slip transitions are very sudden due to the use of the modified OC algorithm aiming for some predefined fidelity. A slight decrease of the target F at the slip point allows to shorten T substantially by falling into a different control family and converging towards an optimal solution there. We never observe such transitions while increasing the target F , just as it is not possible to find the upper optimum class when extending the duration in fixed steps and optimizing the control.

Within the numerical precision of our model, all curves in Fig. 9.3 are consistent with Eq. (9.40). A very important feature is the slow variation of Q_{opt} as $F \rightarrow 1$. This property allows us to extrapolate the fidelity in a wide range of durations and to predict the value of T_{QSL} using equation (9.40). Thus the time fidelity trade-off can be quantified even for moderately optimized processes.

Figure 9.4 presents the optimal control sequences for the relevant range of

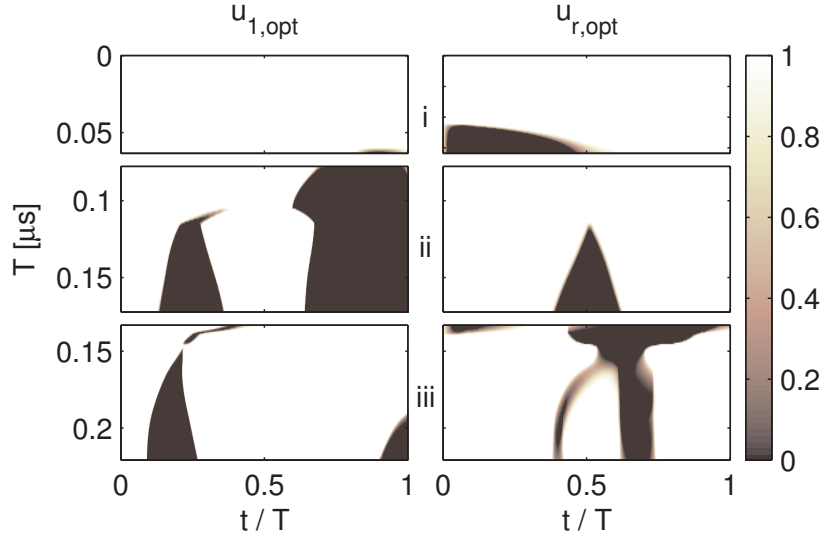


Figure 9.4: Time dependence of the control parameters within the optimal classes *i*, *ii* and *iii* referenced in Fig. 9.3. The images show values of the control parameters u_1 and u_r at each instant along the process t/T (horizontal axis) for each process duration T (vertical axis). Shading encodes the value. A horizontal cross section corresponds to a single optimum control sequence.

process durations in the optimum classes *i*, *ii* and *iii* referenced in Fig. 9.3. Note that the function $\mathbf{u}_{\text{opt}}(T, t)$ is pulse-like but continuous in both dimensions. This demonstrates that for small time variations the process remains close to optimal. Although some optimum classes overlap in time, they are clearly using different strategies to approach the target.

The presented optimum classes are not the only possible solutions to the problem, but they provide very efficient processes reaching perfect fidelity in $T_{\text{QSL}} = 0.2204\mu\text{s}$ for the *iii* class (on the order of the coupling period $2\pi/\Omega_{\text{max}} = 0.1\mu\text{s}$). Nevertheless, the motion in the Hilbert space is most certainly not along a geodesic, since the corresponding path length $\mathcal{C} = \int_0^T \Delta E dt = 10.16$ is much longer than the distance of states $\mathcal{D}(\psi(0), \chi(T)) = \pi/2$. This is due to the character of the Hamiltonians (9.42) and (9.43), which do not provide the ideal driving of the system.

Although this numerical example considers a finite dimensional system, the formalism is universal and applicable to any quantum system for which the state evolution can be computed.

Conclusion and Outlook

We have presented a proposal for a two qubit quantum gate, which can be implemented with ultracold atoms trapped in a species selective potentials. In the simplest case, the gate operation does not require manipulation of the potentials, since it is based on the interference of freely evolving energy eigenstates, which makes it robust against technical noise. The design was generalized for operation with coherent atomic ensembles, where the action can be compared to a transistor like effect. The gate was not subjected to numerical optimization, mainly because we focused on characterising the natural robustness of the physical process. Certainly, the performance could be improved by usage of Optimum Control (OC) algorithms.

We have derived a simple algorithm for optimization of quantum system evolution based on Hilbert space velocity analysis. We have demonstrated its equivalence with standard OC algorithms and quantified the trade-off between the fidelity and the duration. It was shown that the time variation of the direct Hilbert velocity has to be diminished in order to obtain an optimum trajectory, which provides a necessary convergence criterion applicable to local OC algorithms. Not least, the presented formulation of the quantum speed limit (QSL) allows to calculate the value of the shortest time T_{QSL} required to reach a given target state by extrapolation from an optimal processes at $T < T_{\text{QSL}}$. The developed formalism has broad applicability to quantum optimization problems; we illustrate this by applying it to a multilevel system with a constrained Hamiltonian, for which we present and classify a number of different optimal solutions.

Quantum gate perspectives

The project of quantum information processing with motional degrees of freedom can be further developed by designing more single qubit and two qubit gates, and

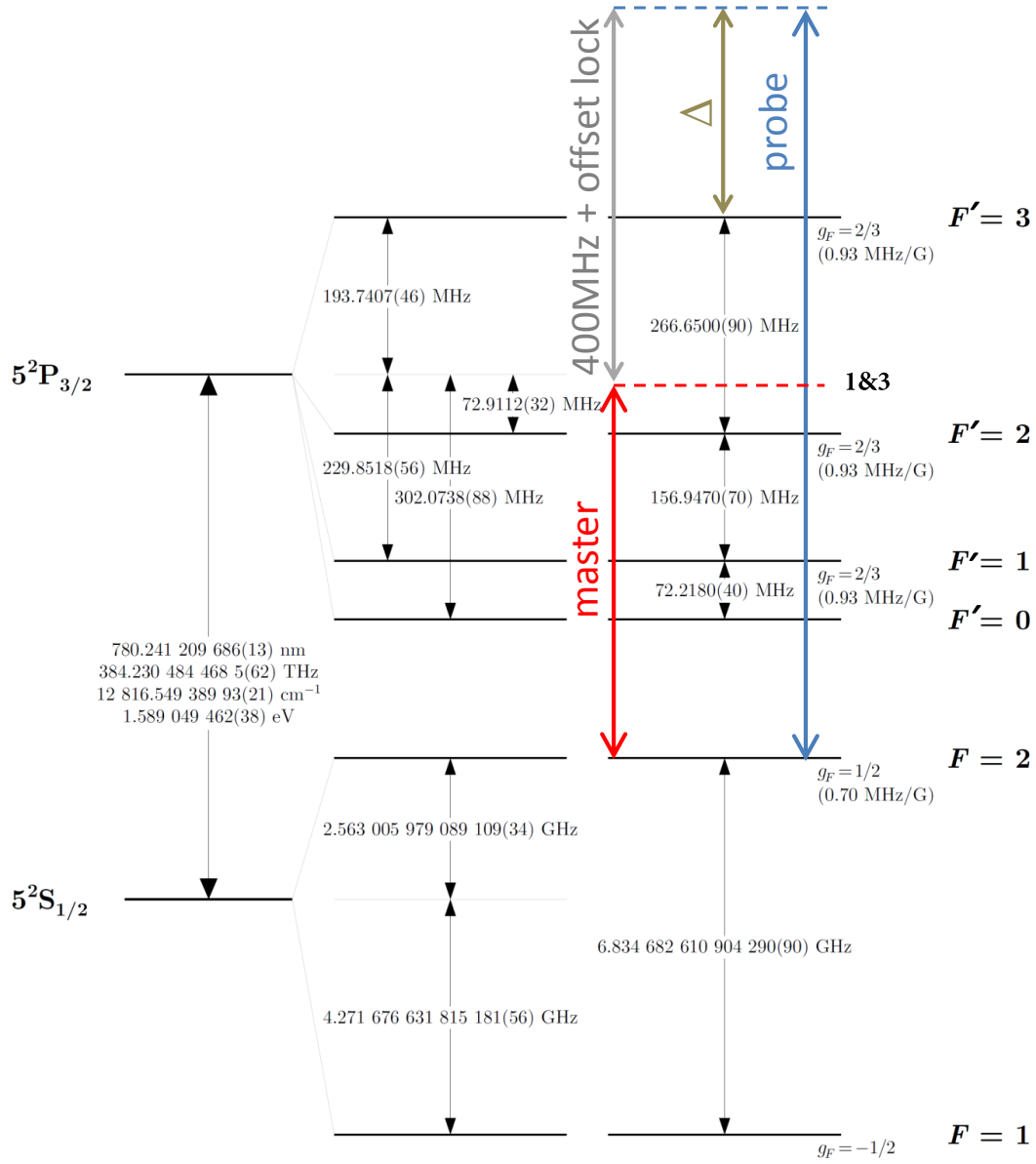
searching for the most suitable architecture for an experimental implementation. For the latter, we might find inspiration in the currently developed techniques for manipulation of atoms, such as the use of spatial light modulators or micro-lens arrays for construction of tunable multi-well trapping potentials. A worthwhile avenue to explore might be the utilization of microwave-dressed state-selective potentials [126], which might allow to use a single atomic species and to swap the role of control and target qubits via state preparation.

Optimum control perspectives

In the optimum control project, the next step will be to apply the Hilbert velocity formalism in well-known quantum processes, such as parametric amplification [127], transport of spin [100] or stimulated emission rapid adiabatic passage (STIRAP) [128], to deepen their understanding and examine the limits. Application to ‘new’ systems is, however, equally interesting.

APPENDIX A

^{87}Rb D2 line and the Faraday laser



State diagram of the hyperfine structure. A master laser is locked to the $F' = 1\&3$ crossover (-212MHz from $F' = 3$). The Faraday laser is locked with an offset lock to the master laser and is shifted $+2 \times 200\text{MHz}$ with a double pass AOM. Data taken from: Daniel A. Steck, "Rubidium 87 D Line Data," available online at <http://steck.us/alkalidata> (revision 2.0.1,2 May 2008).

BIBLIOGRAPHY

- [1] Thomsom, Joseph John: *Conduction of electricity through gases*. Cambridge University Press, (1906).
- [2] Rutheford, E.: *LXXIX. The scattering of α and β particles by matter and the structure of the atom*. Philosophical Magasine Series 6, 21:669–688, (1911).
- [3] Andrews, M. R., C. G. Townsend H.-J. Miesner D. S. Durfee D. M. Kurn and W. Ketterle: *Observation of Interference Between Two Bose Condensates*. Science, 275:637, (1997).
- [4] Jochim, S., M. Bartenstein A. Altmeyer G. Hendl S. Riedl C. Chin J. Hecker Denschlag and R. Grimm: *Bose-Einstein Condensation of Molecules*. Science, 302:5653, (2003).
- [5] Vengalattore, M., J. M. Higbie S. R. Leslie J. Guzman L. E. Sadler and D. M. Stamper-Kurn: *High-resolution magnetometry with a spinor Bose-Einstein condensate*. Phys. Rev. Lett., 97:200801, (2007).
- [6] Müntinga, H., H. Ahlers, M. Krutzik, A. Wenzlawski, S. Arnold, D. Becker, K. Bongs, H. Dittus, H. Duncker, N. Gaaloul, C. Gherasim, E. Giese, C. Grzeschik, T. W. Hänsch, O. Hellmig, W. Herr, S. Herrmann, E. Kajari, S. Kleinert, C. Lämmerzahl, W. Lewoczko-Adamczyk, J. Malcolm, N. Meyer, R. Nolte, A. Peters, M. Popp, J. Reichel, A. Roura, J. Rudolph, M. Schiemangk, M. Schneider, S. T. Seidel, K. Sengstock, V. Tamma, T. Valenzuela, A. Vogel, R. Walser, T. Wendrich, P. Windpassinger, W. Zeller, T. van Zoest, W. Ertmer, W. P. Schleich and E. M. Rasel: *Interferometry with Bose-Einstein Condensates in Microgravity*. Phys. Rev. Lett., 110:093602, (2013).
- [7] Ketterle, W., D. S. Durfee and D. M. Stamper-Kurn: *Proceedings of the*

- International School of Physics of Enrico Fermi, Course CXL: Bose-Einstein condensation in gases.*
Italian Physical Society, pages 67–164, (1998).
- [8] Budker, D., W. Gawlik D. F. Kimball S. M. Rochester V. V. Yashchuk and A. Weis: *Resonant nonlinear magneto-optical effects in atoms.*
Rev. Mod. Phys., 74:1153–1201, (2002).
- [9] Hammerer, K.: *Quantum interface between light and atomic ensembles.*
Rev. Mod. Phys., 82:1041–1093, (2010).
- [10] Turner, L., K. Domen and R. Scholten: *Diffraction-contrast imaging of cold atoms.*
Phys. Rev. A, 72:031403, (2005).
- [11] Ramanathan, A., S. R. Muniz K. C. Wright R. P. Anderson W. D. Phillips K. Helmerson and G. K. Campbell: *Partial-Transfer Absorption Imaging: A versatile technique for optimal imaging of ultracold gases.*
Rev. Sci. Instrum., 83:083119, (2012).
- [12] Gajdacz, M., P. L. Pedersen, T. Mørch, A. Hilliard, J. Sherson and J. Aert: *Non-destructive Faraday imaging of dynamically controlled ultracold atoms.*
Rev. Sci. Instr., 84:083105, (2013).
- [13] Julsgaard, B., A. Kozhekin and E. S. Polzik: *Experimental long-lived entanglement of two macroscopic objects.*
Nature, 413:400–403, (2001).
- [14] Julsgaard, B., J. Sherson J. I. Cirac J. Fiurásek and E. S. Polzik: *Experimental demonstration of quantum memory for light.*
Nature, 432:482–6, (2004).
- [15] Sherson, J. F., H. Krauter R. K. Olsson B. Julsgaard K. Hammerer I. Cirac and E. S. Polzik: *Quantum teleportation between light and matter.*
Nature, 443:557–560, (2006).
- [16] Kubasik, M., M. Koschorreck M. Napolitano S. de Echaniz H. Crepaz J. Eschner E. S. Polzik and M. W. Mitchell: *Polarization-based light-atom quantum interface with an all-optical trap.*
Phys. Rev. A, 79:043815, (2009).
- [17] Kaminski, F., N. Kampel M. Steenstrup A. Griesmaier E. Polzik and J. Müller: *In-situ dual-port polarization contrast imaging of Faraday rotation in a high optical depth ultracold ^{87}Rb atomic ensemble.*
Eur. Phys. J. D, 66:227, (2012).
- [18] Takano, T., M. Fuyama R. Namiki and Y. Takahashi: *Spin Squeezing of a Cold Atomic Ensemble with the Nuclear Spin of One-Half.*
Phys. Rev. Lett., 102:033601, (2009).

- [19] Liu, Y., S. Jung, S. Maxwell, L. Turner, E. Tiesinga and P. Lett: *Quantum Phase Transitions and Continuous Observation of Spinor Dynamics in an Antiferromagnetic Condensate*.
Phys. Rev. Lett., 102:125301, (2009).
- [20] Hall, D. S., M. R. Matthews, J. R. Ensher, C. E. Wieman and E. A. Cornell: *Dynamics of Component Separation in a Binary Mixture of Bose-Einstein Condensates*.
Phys. Rev. Lett., 81:4531–4531, (1998).
- [21] Matthews, M. R., D. S. Hall, D. S. Jin, J. R. Ensher, C. E. Wieman, E. A. Cornell, F. Dalfovo, C. Minniti and S. Stringari: *Dynamical Response of a Bose-Einstein Condensate to a Discontinuous Change in Internal State*.
Phys. Rev. Lett., 81:243–247, (1998).
- [22] Stenger, J. and, Inouye S., D. Stamper-Kurn, H.J. Miesner, A. Chikkatur and W. Ketterle: *Spin domains in ground-state Bose-Einstein condensates*.
Nature 396, 345., 396:345, (1998).
- [23] Sadler, L. E., J. M. Higbie, S. R. Leslie, M. Vengalattore and D. M. Stamper-Kurn: *Spontaneous symmetry breaking in a quenched ferromagnetic spinor Bose-Einstein condensate*.
Nature, 443(7109):312–315, (2006).
- [24] Klempt, C., O. Topic, G. Gebreyesus, M. Scherer, T. Henninger, P. Hyllus, W. Ertmer, L. Santos and J. J. Arlt: *Parametric Amplification of Vacuum Fluctuations in a Spinor Condensate*.
Phys. Rev. Lett., 104:195303, (2010).
- [25] Einstein, A., N. Rosen and B. Podolsky: *Can Quantum-Mechanical Description of Physical Reality Be Considered Complete?*
Phys. Rev., 47:777, (1935).
- [26] Bell, J.S.: *On the Einstein Podolsky Rosen paradox*.
Physics, 1, No.3:195–200, (1964).
- [27] Bell, John S.: *Speakable and Unsayable in Quantum Mechanics*.
Cambridge University Press, (1987).
- [28] Holland, Peter R.: *The Quantum Theory of Motion: An Account of the de Broglie-Bohm Causal Interpretation of Quantum Mechanics*.
Cambridge University Press, (1995).
- [29] Kwiat, Paul G., Klaus Mattle Harald Weinfurter and Anton Zeilinger: *New High-Intensity Source of Polarization-Entangled Photon Pairs*.
Phys. Rev. Lett., 75:4337, (1995).

-
- [30] Lücke, B. M., Scherer J. Kruse L. Pezzé F. Deuretzbacher P. Hyllus O. Topic J. Peise W. Ertmer J. Arlt L. Santos A. Smerzi and C. Klempt: *Twin Matter Waves for Interferometry Beyond the Classical Limit*. Science, 334:773, (2011).
- [31] Muessel, W., H. Strobel, D. Linnemann, D. B. Hume and M. K. Oberthaler: *Scalable Spin Squeezing for Quantum-Enhanced Magnetometry with Bose-Einstein Condensates*. Phys. Rev. Lett., 113:103004, (2014).
- [32] Chang, Ming-Shien, Qishu Qin Wenxian Zhang Li You and Michael S. Chapman: *Coherent spinor dynamics in a spin-1 Bose condensate*. Nature Physics, 1:111–116, (2005).
- [33] Liu, Y., S. Jung, S. E. Maxwell, L. D. Turner, E. Tiesinga and P. D. Lett: *Quantum Phase Transitions and Continuous Observation of Spinor Dynamics in an Antiferromagnetic Condensate*. Phys. Rev. Lett., 102:125301, (2009).
- [34] Krauser, J. S., J. Heinze N. Fläschner S. Götze O. Jürgensen D. Lühmann C. Becker and K. Sengstock: *Coherent multi-flavour spin dynamics in a fermionic quantum gas*. Nature Physics, 8:813–818, (2012).
- [35] Klempt, C., O. Topic, G. Gebreyesus, M. Scherer, T. Henninger, P. Hyllus, W. Ertmer, L. Santos and J. J. Arlt: *Multiresonant Spinor Dynamics in a Bose-Einstein Condensate*. Phys. Rev. Lett., 103:195302, (2009).
- [36] Scherer, M., B. Lücke, G. Gebreyesus, O. Topic, F. Deuretzbacher, W. Ertmer, L. Santos, J. J. Arlt and C. Klempt: *Spontaneous Breaking of Spatial and Spin Symmetry in Spinor Condensates*. Phys. Rev. Lett., 105:135302, 2010.
- [37] Scherer, M., B. Lücke, J. Peise, O. Topic, G. Gebreyesus, F. Deuretzbacher, W. Ertmer, L. Santos, C. Klempt and J. J. Arlt: *Spontaneous symmetry breaking in spinor Bose-Einstein condensates*. Phys. Rev. A, 88:053624, (2013).
- [38] Chu, Steven, Claude Cohen-Tannoudji and William D. Phillips: *The Nobel Prize in Physics 1997*.
- [39] Metcalf, Harold J. and Peter van der Straten: *Laser Cooling and Trapping*. Springer-Verlag New York, (1999).
- [40] Ketterle, W., D.S. Durfee and D.M. Stamper-Kurn: *Making, probing and understanding Bose-Einstein condensates*.

- In Bose-Einstein condensation in atomic gases, Proceedings of the International School of Physics "Enrico Fermi", Course CXL, edited by M. Inguscio, S. Stringari and C.E. Wieman, pages 67–176, (1999).
- [41] Steck, Daniel A.: *Rubidium 87 D Line Data*, available online at <http://steck.us/alkalidata/rubidium87numbers.1.6.pdf>, (2001).
- [42] Raab, E. L., M. Prentiss, Alex Cable, Steven Chu and D. E. Pritchard: *Trapping of Neutral Sodium Atoms with Radiation Pressure*. Phys. Rev. Lett., 59:2631–2634, (1987).
- [43] Böhi, Pascal, Max F. Riedel, Johannes Hoffrogge, Jakob Reichel, Theodor W. Hänsch and Philipp Treutlein: *Coherent manipulation of Bose-Einstein condensates with state-dependent microwave potentials on an atom chip*. Nature Physics, 5:592–597, (2009).
- [44] Timoney, N., I. Baumgart, M. Johanning, A. F. Varón, M. B. Plenio, A. Retzker and Ch. Wunderlich: *Quantum gates and memory using microwave-dressed states*. Nature, 476:185–188, (2011).
- [45] Bloch, Immanuel: *Ultracold quantum gases in optical lattices*. Nature Physics, 1:23 – 30, (2005).
- [46] Pethick, C.J. and H. Smith: *Bose-Einstein Condensation in Dilute Gases*. Cambridge University Press, (2008).
- [47] Hilliard, A.: *Collective Rayleigh scattering in a Bose Einstein condensate*. PhD thesis, University of Copenhagen, Denmark, (2008).
- [48] Pedersen, Poul Lindholm: *Multi-mode spin dynamics of a Bose-Einstein condensate in an optical lattice*. PhD thesis, Aarhus University, Denmark, (2014).
- [49] Andersen, Henrik Kjær: *Bose-Einstein condensates in optical lattices*. PhD thesis, Aarhus University, Denmark, (2008).
- [50] Pedersen, Poul L., Mirosław Gajdacz, Frank Deuretzbacher, Luis Santos, Carsten Klempt, Jacob F. Sherson, Andrew J. Hilliard and Jan J. Arlt: *Spin dynamics in a two-dimensional quantum gas*. Phys. Rev. A, 89:051603, (2014).
- [51] Chin, Cheng, Rudolf Grimm, Paul Julienne and Eite Tiesinga: *Feshbach resonances in ultracold gases*. Rev. Mod. Phys., 82:1225–1286, (2010).
- [52] Stamper-Kurn, Dan M. and Masahito Ueda: *Spinor Bose gases: Symmetries, magnetism, and quantum dynamics*. Rev. Mod. Phys., 85:1191–1244, (2013).

-
- [53] Zhao, L., J. Jiang, T. Tang, M. Webb and Y. Liu: *Dynamics in spinor condensates tuned by a microwave dressing field*.
Phys. Rev. A, 89:023608, (2014).
- [54] Gerbier, Fabrice, Artur Widera, Simon Fölling, Olaf Mandel and Immanuel Bloch: *Resonant control of spin dynamics in ultracold quantum gases by microwave dressing*.
Phys. Rev. A, 73:041602, (2006).
- [55] Klausen, Nille N., John L. Bohn and Chris H. Greene: *Nature of spinor Bose-Einstein condensates in rubidium*.
Phys. Rev. A, 64:053602, (2001).
- [56] Ketterle, Wolfgang and Shin Inouye: *Collective enhancement and suppression in Bose-Einstein condensates*.
Comptes Rendus de l'Académie des Sciences - Series {IV} - Physics, 2(3):339 – 380, (2001).
- [57] Kubasik, Marcin: *Towards Spin Squeezing in Cold Atomic Ensembles*.
PhD thesis, Universitat Politècnica de Catalunya, Spain, (2009).
- [58] Hynccek, J. and T. Nishiwaki: *Excess noise and other important characteristics of low light level imaging using charge multiplying CCDs*.
IEEE Transactions on Electron Devices, Vol. 50, Nr. 1:239–245, (2003).
- [59] Robbins, M. S. and B. J. Hadwen: *The noise performance of electron multiplying charge-coupled devices*.
IEEE Transactions on Electron Devices, Vol. 50, Nr. 5:1227, (2003).
- [60] Schünemann, U., H. Engler, R. Grimm, M. Weidemüller and M. Zielonkowski: *Simple scheme for tunable frequency offset locking of two lasers*.
Rev. Sci. Instrum., 70:242–243, (1999).
- [61] Yefsah, T., R. Desbuquois, L. Chomaz, K. Günter and J. Dalibard: *Exploring the Thermodynamics of a Two-Dimensional Bose Gas*.
Phys. Rev. Lett., 107:130401, (2011).
- [62] Reinaudi, G., T. Lahaye Z. Wang and D. Guéry-Odelin: *Strong saturation absorption imaging of dense clouds of ultracold atoms*.
Opt. Lett., 32:3143–3145, (2007).
- [63] Budker, D. and M. Romalis: *Optical magnetometry*.
Nature Physics, 3:227–234, (2007).
- [64] Kominis, I. K., T. W. Kornack J. C. Allred and M. V. Romalis: *A subfemtotesla multichannel atomic magnetometer*.
Nature, 422:596–599, (2003).

- [65] Seltzer, S. J. and M. V. Romalis: *Unshielded three-axis vector operation of a spin-exchange-relaxation-free atomic magnetometer*. Appl. Phys. Lett., 85:4804, (2004).
- [66] Fatemi, F. K. and M. Bashkansky: *Spatially resolved magnetometry using cold atoms in dark optical tweezers*. Optics express, 18:2190–2196, (2010).
- [67] Wildermuth, S., S. Hofferberth I. Lesanovsky S. Groth P. Krüger J. Schmiedmayer and I. Bar-Joseph: *Sensing electric and magnetic fields with Bose-Einstein condensates*. Appl. Phys. Lett., 88:264103, (2006).
- [68] Smith, A., B. E. Anderson S. Chaudhury and P. S. Jessen: *Three-axis measurement and cancellation of background magnetic fields to less than 50 μ G in a cold atom experiment*. J. Phys. B: At. Mol. Opt. Phys., 44:205002, (2011).
- [69] Koschorreck, M., M. Napolitano B. Dubost and M. W. Mitchell: *High resolution magnetic vector-field imaging with cold atomic ensembles*. Appl. Phys. Lett., 98:074101, (2011).
- [70] Petrov, P. G., D. Oblak C. L. G. Alzar N. Kjærgaard and E. S. Polzik: *Nondestructive interferometric characterization of an optical dipole trap*. Phys. Rev. A, 75:033803, (2007).
- [71] Kohonen, M., P. G. Petrov, R. A. Nyman and E. A. Hinds: *Minimally destructive detection of magnetically trapped atoms using frequency-synthesized light*. New J. Phys., 13:085006, (2011).
- [72] Ketterle, W. and N. J. Van Druten: *Evaporative cooling of trapped atoms*. Advances in Atomic, Molecular and Optical Physics, 37:181–231, (1996).
- [73] Shockley, William Bradford, John Bardeen and Walter Houser Brattainer: *The Nobel Prize in Physics 1956*.
- [74] Nielsen, Michael A. and Isaac L. Chuang: *Quantum Computation and Quantum Information*. Cambridge University Press, (2010).
- [75] Grover, Lov K.: *A Fast Quantum Mechanical Algorithm for Database Search*. In *Proceedings of the Twenty-eighth Annual ACM Symposium on Theory of Computing*, STOC '96, pages 212–219, New York, NY, USA, (1996). ACM.
- [76] Harty, T. P., D. T. C. Allcock, C. J. Ballance, L. Guidoni, H. A. Janacek, N. M. Linke, D. N. Stacey and D. M. Lucas: *High-Fidelity Preparation, Gates, Memory, and Readout of a Trapped-Ion Quantum Bit*. Phys. Rev. Lett., 113:220501, (2014).

- [77] Pribiag, V. S., S. Nadj-Perge S. M. Frolov J. W. G. van den Berg I. van Weperen S. R. Plissard E. P. A. M. Bakkers and L. P. Kouwenhoven: *Electrical control of single hole spins in nanowire quantum dots*. Nature Nanotechnology, 8:170–174, (2013).
- [78] Clarke, John and Frank K. Wilhelm: *Superconducting quantum bits*. Nature, 453:1031–1042, (2008).
- [79] Brennen, Gavin K., Carlton M. Caves, Poul S. Jessen and Ivan H. Deutsch: *Quantum Logic Gates in Optical Lattices*. Phys. Rev. Lett., 82:1060–1063, (1999).
- [80] Kane, B. E.: *A silicon-based nuclear spin quantum computer*. Nature, 393:133–137, (1998).
- [81] Andrews, M. R., C. G. Townsend, H.-J. Miesner, D. S. Durfee, D. M. Kurn and W. Ketterle: *Observation of Interference Between Two Bose Condensates*. Science, 275(5300):637–641, (1997).
- [82] Tasca, D. S., R. M. Gomes, F. Toscano, P. H. Souto Ribeiro and S. P. Walborn: *Continuous-variable quantum computation with spatial degrees of freedom of photons*. Phys. Rev. A, 83:052325, (2011).
- [83] Miková, Martina, Helena Fikerová, Ivo Straka, Michal Mičuda, Jaromír Fiurášek, Miroslav Ježek and Miloslav Dušek: *Increasing efficiency of a linear-optical quantum gate using electronic feed-forward*. Phys. Rev. A, 85:012305, (2012).
- [84] Charron, Eric, Eite Tiesinga, Frederick Mies and Carl Williams: *Optimizing a Phase Gate Using Quantum Interference*. Phys. Rev. Lett., 88:077901, (2002).
- [85] Mompert, J., K. Eckert, W. Ertmer, G. Birkl and M. Lewenstein: *Quantum Computing with Spatially Delocalized Qubits*. Phys. Rev. Lett., 90:147901, (2003).
- [86] Strauch, Frederick W., Mark Edwards, Eite Tiesinga, Carl Williams and Charles W. Clark: *Tunneling phase gate for neutral atoms in a double-well lattice*. Phys. Rev. A, 77:050304, (2008).
- [87] Charron, E., M. A. Cirone, A. Negretti, J. Schmiedmayer and T. Calarco: *Theoretical analysis of a realistic atom-chip quantum gate*. Phys. Rev. A, 74:012308, (2006).
- [88] Sherson, Jacob F., Christof Weitenberg, Manuel Endres, Marc Cheneau, Immanuel Bloch and Stefan Kuhr: *Single-atom-resolved fluorescence imaging of an atomic Mott insulator*.

- Nature, 467:68, (2010).
- [89] Pepino, R. A., J. Cooper, D. Z. Anderson and M. J. Holland: *Atomtronic Circuits of Diodes and Transistors*.
Phys. Rev. Lett., 103(14):140405, (2009).
- [90] Seaman, B. T., M. Krämer, D. Z. Anderson and M. J. Holland: *Atomtronics: Ultracold-atom analogs of electronic devices*.
Phys. Rev. A, 75(2):023615, (2007).
- [91] Das, Kunal K. and Seth Aubin: *Quantum Pumping with Ultracold Atoms on Microchips: Fermions versus Bosons*.
Phys. Rev. Lett., 103(12):123007, (2009).
- [92] Stickney, James A., Dana Z. Anderson and Alex A. Zozulya: *Transistorlike behavior of a Bose-Einstein condensate in a triple-well potential*.
Phys. Rev. A, 75(1):013608, (2007).
- [93] Benseny, A., S. Fernández-Vidal, J. Bagudà, R. Corbalán, A. Picón, L. Roso, G. Birkel and J. Mompart: *Atomtronics with holes: Coherent transport of an empty site in a triple-well potential*.
Phys. Rev. A, 82(1):013604, (2010).
- [94] Vaishnav, J. Y., Julius Ruseckas, Charles W. Clark and Gediminas Juzeliūnas: *Spin Field Effect Transistors with Ultracold Atoms*.
Phys. Rev. Lett., 101(26):265302, (2008).
- [95] Pontryagin, L. S., V. G. Boltyanskii, R. V. Gamkrelidze and E. F. Mishchenko: *The Mathematical Theory of Optimal Processes*.
John Wiley and Sons, New York, (1962).
- [96] Mandelstam, L. and Ig. Tamm: *The uncertainty relation between energy and time in non-relativistic quantum mechanics*.
Journal of Physics (Moscow), 9:249, (1945).
- [97] Bhattacharyya, K.: *Quantum decay and the Mandelstam-Tamm-energy inequality*.
Journal of Physics A: Mathematical and General, 16(13):2993, (1983).
- [98] Anandan, J. and Y. Aharonov: *Geometry of quantum evolution*.
Phys. Rev. Lett., 65:1697–1700, (1990).
- [99] Carlini, Alberto, Akio Hosoya, Tatsuhiko Koike and Yosuke Okudaira: *Time-Optimal Quantum Evolution*.
Phys. Rev. Lett., 96:060503, (2006).
- [100] Caneva, T., M. Murphy, T. Calarco, R. Fazio, S. Montangero, V. Giovannetti and G. E. Santoro: *Optimal Control at the Quantum Speed Limit*.
Phys. Rev. Lett., 103:240501, (2009).

-
- [101] Chakrabarti, Raj, Rebing Wu and Herschel Rabitz: *Quantum Pareto optimal control*.
Phys. Rev. A, 78:033414, (2008).
- [102] Koike, Tatsuhiko and Yosuke Okudaira: *Time complexity and gate complexity*.
Phys. Rev. A, 82:042305, (2010).
- [103] Caneva, Tommaso, Tommaso Calarco, Rosario Fazio, Giuseppe E. Santoro and Simone Montangero: *Speeding up critical system dynamics through optimized evolution*.
Phys. Rev. A, 84:012312, (2011).
- [104] Tibbetts, Moore, Katharine W., Constantin Brif, Matthew D. Grace, Ashley Donovan, David L. Hocker, Tak-San Ho, Re-Bing Wu and Herschel Rabitz: *Exploring the tradeoff between fidelity and time optimal control of quantum unitary transformations*.
Phys. Rev. A, 86:062309, (2012).
- [105] Mishima, K. and K. Yamashita: *Free-time and fixed end-point optimal control theory in quantum mechanics: Application to entanglement generation*.
The Journal of Chemical Physics, 130(3):034108, (2009).
- [106] Lapert, M., J. Salomon and D. Sugny: *Time-optimal monotonically convergent algorithm with an application to the control of spin systems*.
Phys. Rev. A, 85:033406, (2012).
- [107] Gajdacz, Miroslav, Tomáš Opatrný and Kunal K. Das: *Transparent non-local species-selective transport in an optical superlattice containing two interacting atom species*.
Phys. Rev. A, 83:033623, (2011).
- [108] Das, K. K., M. D. Girardeau and E. M. Wright: *Crossover from one to three dimensions for a gas of hard-core bosons*.
Phys. Rev. Lett., 89:110402, (2002).
- [109] Marzok, C., B. Deh, C. Zimmermann, Ph. W. Courteille, E. Tiemann, Y. V. Vanne and A. Saenz: *Feshbach resonances in an ultracold ${}^7\text{Li}$ and ${}^{87}\text{Rb}$ mixture*.
Phys. Rev. A, 79:012717, (2009).
- [110] Bhattacharya, M., L.O. Baksmaty, S.B. Weiss and N.P. Bigelow: *Feshbach resonances in ${}^{23}\text{Na}$ - ${}^{87}\text{Rb}$* .
Eur. Phys. J. D, 31:301, (2004).
- [111] Strecker, K. E., G.e B. Partridge and R. G. Truscott, A. G. and Hulet: *Formation and propagation of matter-wave soliton trains*.
Nature, 417:150, (2002).

-
- [112] Das, K. K.: *Highly anisotropic Bose-Einstein condensates: crossover to lower dimensions*.
Phys. Rev. A, 66:053612, (2002).
- [113] Gibbons, Michael J., Soo Y. Kim, Kevin M. Fortier, Peyman Ahmadi and Michael S. Chapman: *Achieving very long lifetimes in optical lattices with pulsed cooling*.
Phys. Rev. A, 78:043418, (2008).
- [114] Chikkatur, A. P., Y. Shin, A. E. Leanhardt, D. Kielpinski, E. Tsikata, T. L. Gustavson, D. E. Pritchard and W. Ketterle: *Continuous Source of Bose-Einstein Condensed Atoms*.
Science, 296:2192, (2002).
- [115] Sklarz, Shlomo E. and David J. Tannor: *Loading a Bose-Einstein condensate onto an optical lattice: An application of optimal control theory to the nonlinear Schrödinger equation*.
Phys. Rev. A, 66:053619, (2002).
- [116] Wootters, W. K.: *Statistical distance and Hilbert space*.
Phys. Rev. D, 23:357–362, (1981).
- [117] Jones, Philip J. and Pieter Kok: *Geometric derivation of the quantum speed limit*.
Phys. Rev. A, 82:022107, (2010).
- [118] Braunstein, Samuel L. and Carlton M. Caves: *Statistical distance and the geometry of quantum states*.
Phys. Rev. Lett., 72:3439–3443, (1994).
- [119] Eitan, Reuven, Michael Mundt and David J. Tannor: *Optimal control with accelerated convergence: Combining the Krotov and quasi-Newton methods*.
Phys. Rev. A, 83:053426, (2011).
- [120] Schirmer, S. G. and Pierre de Fouquieres: *Efficient algorithms for optimal control of quantum dynamics: the Krotov method unencumbered*.
New Journal of Physics, 13(7):073029, (2011).
- [121] Krotov, Vadim F.: *Advances in Nonlinear Dynamics and Control: A Report from Russia*.
Birkhäuser Boston, (1993).
- [122] Khaneja, Navin, Steffen J. Glaser and Roger Brockett: *Sub-Riemannian geometry and time optimal control of three spin systems: Quantum gates and coherence transfer*.
Phys. Rev. A, 65:032301, (2002).

-
- [123] Khaneja, Navin, Timo Reiss, Cindie Kehlet, Thomas Schulte-Herbrüggen and Steffen J. Glaser: *Optimal control of coupled spin dynamics: design of NMR pulse sequences by gradient ascent algorithms*.
Journal of Magnetic Resonance, 172(2):296 – 305, (2005).
- [124] Rothman, Adam, Tak-San Ho and Herschel Rabitz: *Observable-preserving control of quantum dynamics over a family of related systems*.
Phys. Rev. A, 72:023416, (2005).
- [125] Møller, Ditte, Lars Bojer Madsen and Klaus Mølmer: *Quantum Gates and Multiparticle Entanglement by Rydberg Excitation Blockade and Adiabatic Passage*.
Phys. Rev. Lett., 100:170504, (2008).
- [126] Guarrera, V., R. Szmuk, J. Reichel and P. Rosenbusch: *Microwave-dressed state-selective potentials for atom interferometry*.
arXiv:1503.02657, (2015).
- [127] Mollow, B. R. and R. J. Glauber: *Quantum Theory of Parametric Amplification. I*.
Phys. Rev., 160:1076–1096, (1967).
- [128] Gaubatz, U., P. Rudecki, S. Schiemann and K. Bergmann: *Population transfer between molecular vibrational levels by stimulated Raman scattering with partially overlapping laser fields. A new concept and experimental results*.
The Journal of Chemical Physics, 92(9):5363–5376, (1990).